A Practical Guide to Corrosion of Atmospheric Corrosion Resistant Steel Bridges Exposed to De-icing Salt: Understanding Micro-Climate Effects

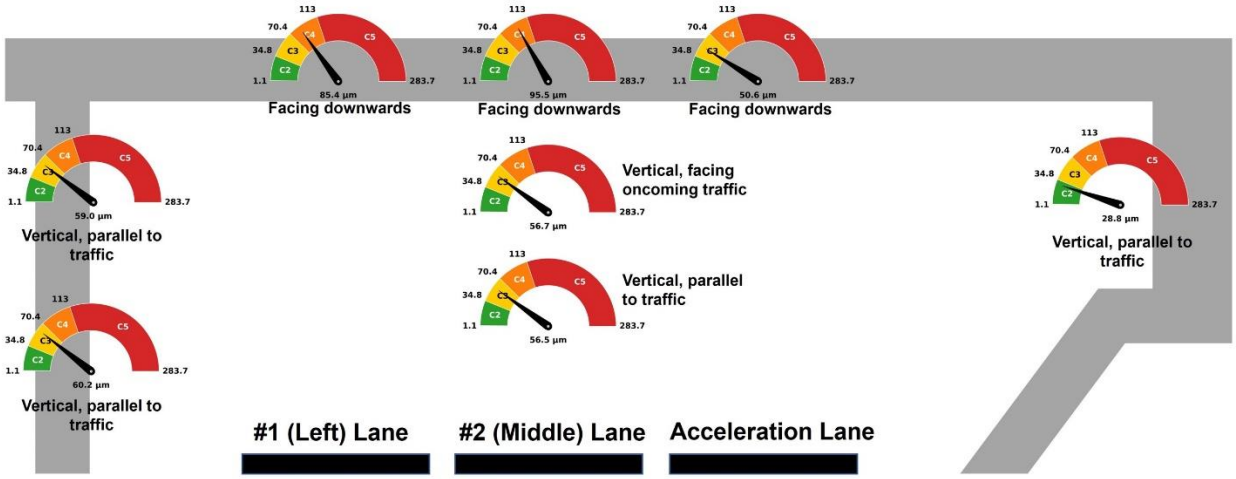

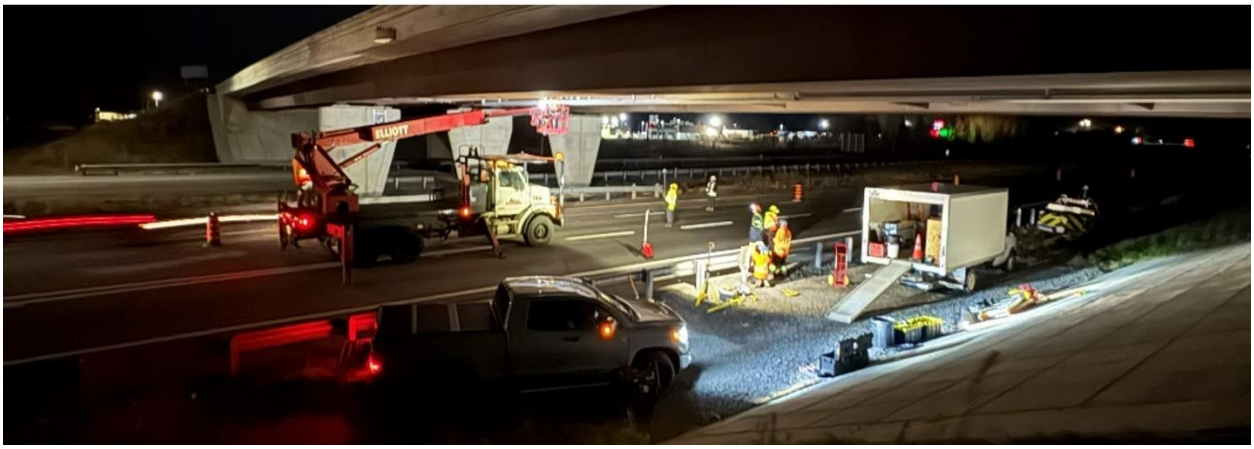

Non-sensitive

July 31, 2026

Dr. Nafiseh Ebrahimi, Ph.D., P.Eng.
Mr. Marc-Olivier Gagné, B. Eng.
Dr. Alban Morel, Ph.D.
Dr. Danick Gallant, Ph.D.

A Practical Guide to Corrosion of Atmospheric Corrosion Resistant Steel Bridges Exposed to De-icing Salt: Understanding Micro-Climate Effects

Nafiseh Ebrahimi, Marc-Oliver Gagné, Alban Morel and Danick Gallant

The authors wish to acknowledge the dedicated contributions of their colleagues at the National Research Council Canada (NRC), who were instrumental to the success of this work, listed here in alphabetical order:

Ms. Joannie Bérubé, Mr. Samuel Croft-Tremblay, Mr. Dennis Krys, Mr. Jean-Nicolas Lachance, Dr. Mojtaba Momeni, Mr. Alexandre Morin, Dr. Olga Naboka, Ms. Xinran Pan, Mr. Mario Patry, Mr. Michel Perron, Mr. Antal Prigli, Dr. Melina Roshanfar, Ms. Amélie Ruest, Ms. Guan Ying Wang, Dr. Jieying Zhang.

The authors also extend their gratitude to the Ministry of Transportation of Ontario (MTO), and especially to Mr. James Combe and Mr. Kris Mermigas, for their commitment and support in making this project possible.

External Review Committee

The authors would like to express their sincere gratitude to the External Review Committee for their valuable time, expertise, and thoughtful feedback throughout the review process listed here in alphabetical order:

Mr. James Combe, P. Eng. Lead Bridge Engineer, Bridge Management & Rehabilitation, Structures Office, Ministry of Transportation, Ontario Public Service

Mr. Ilia Korotkine, P. Eng., M. Eng., ENV SP, PMP, Senior Engineer & Senior Project Manager, Major Bridges and Projects, Housing, Infrastructure and Communities Canada, Government of Canada

Mr. Guy Mailhot, P. Eng., M.Eng., FCSCE, FEIC, Chief Engineer, The Jacques Cartier and Champlain Bridges Incorporated.

Mr. Kris Mermigas, P. Eng, MA. Sc., Head Engineer, Bridge Design, Structures Office, Ministry of Transportation, Ontario Public Service

Cat. No. NR24-146/2026E-PDF

ISBN 978-0-660-99870-1

EXECUTIVE SUMMARY

Atmospheric Corrosion Resistant (ACR) steel, also commonly known as weathering steel, has become a preferred material for bridge construction across Canada and internationally due to its ability to form a self-protecting oxide layer that reduces maintenance requirements and extends service life. Its benefits include eliminating periodic repainting, minimizing traffic disruption, and providing long-term structural resilience. However, its performance is highly dependent on local micro-climatic conditions, particularly exposure to de-icing salts. Premature corrosion failures in weathering steel bridges are most often caused by environmental and detailing factors rather than material deficiencies. This guide develops a framework for the selection, design, and maintenance of weathering steel bridges suited to Canadian environments, bridging the gap between laboratory corrosion science and practical field application.

Weathering steels are low-alloy structural steels containing copper, chromium, nickel, phosphorus, silicon, and manganese in small proportions. Their corrosion resistance arises from the formation of a dense, adherent patina that limits oxygen and chloride penetration. Copper and nickel are critical in producing a compact oxide structure, while chromium contributes to the formation of a secondary passive film. Common bridge grades include ASTM A588, A242, and A709 50W, with enhanced corrosion-resistant grades such as ASTM A1010 offering superior resistance in chloride-rich environments through the formation of chromium oxide rather than a traditional patina. Although A1010 has a higher initial cost, lifecycle cost analysis demonstrates its economic advantage in aggressive environments by eliminating coating maintenance.

Patina formation depends on alternating wet and dry cycles that stabilize the protective goethite phase. In chloride-rich conditions, the less protective akaganeite phase forms instead, creating a porous oxide that accelerates corrosion. Continuous moisture, poor drainage, and persistent chloride exposure prevent proper patina development and result in corrosion rates similar to carbon steel. Using the ISO 9223 classification, unpainted weathering steel is suitable up to Category C4, while C5 environments require coatings or alternative materials. In Canada, de-icing salts raise local corrosivity beyond regional averages. Sodium chloride increases time of wetness and encourages akaganeite formation, while infiltration through leaking joints and traffic spray produces localized corrosion zones, especially on horizontal surfaces and girders near traffic lanes. It is a common and good industry practice to incorporate an additional coating protection system (paint system) locally under expansion joints (to enhance steel protection in these vulnerable areas) and above supporting concrete piers to prevent rust staining of the concrete surfaces.

A 10-year field exposure study conducted under the Highway 404 and Bloomington Road overpass, Ontario, tested seven weathering steel alloys under severe de-icing conditions. Results confirmed that chloride contamination fundamentally alters patina chemistry and structure. The modified GM 9540P cyclic corrosion test was found to best replicate field conditions, while the ASTM G85-A5 (Prohesion) test overestimated corrosion rates. The electrochemical method known as linear polarization resistance used in the study was found

unreliable for predicting atmospheric durability because it lacks drying phases essential to patina stabilization. X-ray diffraction and electron microscopy confirmed a dominant presence of akaganeite ranging from 44 to 70 percent across all alloys, with incomplete patina stabilization and chloride incorporation in every sample. A direct correlation between patina thickness and corrosion rate was established, enabling non-destructive field estimation of corrosion using portable gauges.

Live in-service corrosion and environmental monitoring at the Highway 401 in Lancaster, Ontario, were validated by laboratory experiments. Electrical resistance sensors provided reliable real-time data, slightly conservative but within expected variance, proving effective for continuous structural health monitoring. The monitoring program identified three distinct tiers of micro-environmental corrosivity: the highest corrosion occurred on downward-facing surfaces above traffic lanes, reaching up to 95 µm per year; intermediate corrosion occurred on vertical splash-zone surfaces at 56 to 60 µm per year; and the lowest rates were found on sheltered abutments around 29 µm per year. These results demonstrate that bridges over a road located in regions classified as C2 or C3 as per ISO 9223 can experience localized C4-level corrosion in specific structural zones, emphasizing the need for micro-zone-specific design and maintenance strategies rather than relying on a single macro-environmental classification.

Table of contents

1 Introduction

1.1 Background and Infrastructure Context

The sustainability of national transportation networks depends heavily on the selection of materials that can withstand increasingly aggressive environmental conditions. As bridge inventories age, the civil engineering sector has shifted away from traditional "build-and-replace" models toward "designed durability." Weathering steel (WS) has been explored as a corrosion management approach within this paradigm, offering an autonomous corrosion-protection mechanism that aligns with the requirements of modern sustainable infrastructure. By reducing the reliance on volatile organic compound (VOC)-heavy coating systems and minimizing maintenance-related traffic disruptions to maintain coating systems, WS can provide, if used in an appropriate environment, a distinct advantage in both environmental impact and public utility.

1.2 The Need for a National Framework

Despite the inherent benefits of weathering steel, its performance is highly sensitive to site-specific microclimates [1–3]. Historical data indicates that the premature failure of the protective patina is rarely a result of material deficiency, but rather a consequence of improper environmental assessment or inadequate detailing. In many jurisdictions, the lack of a standardized approach to corrosion allowances and maintenance protocols has led to inconsistent performance across bridge inventories. There is, therefore, a critical need for a centralized technical directive that harmonizes international best practices with regional environmental constraints to ensure the safe and predictable long-term behavior of these structures. This guide is structured to transition from fundamental material science to practical field application. It seeks to bridge the gap between academic corrosion research and the functional needs of design engineers and maintenance bridge owners. The primary objectives are:

- To identify "exclusion zones" where high chloride concentrations or chronic moisture levels render unpainted weathering steel unsuitable [4].[5]
- To leverage sensing technology to characterize the bridge microclimate in real time, enabling better prediction of corrosion risk and more informed maintenance and design decisions.
- To use field data to guide the selection of materials for bridges, optimizing durability and performance under site-specific environmental conditions.

2 Overview of Weathering Steels and Metallurgical Basis

Weathering steels (WS), a distinct classification of high strength, low-alloy structural steels, are intentionally designed to exhibit superior resistance to atmospheric corrosion in comparison to conventional carbon steel [6]. The fundamental metallurgical profile of these materials is characterized by carbon content typically maintained below 0.2 wt.% and the inclusion of specific trace alloying elements. The collective proportion of these critical alloying elements generally does not exceed the range of 3 wt.% to 5 wt.% [7]. This precise microstructural design serves as the foundation for the material's enhanced long-term durability, a critical consideration in infrastructure management.

The core mechanism underpinning the exceptional corrosion resistance of weathering steel is its unique capacity to spontaneously form a dense and tightly adhering protective rust layer, commonly referred to as the patina [5,6,8–13], upon exposure to appropriate atmospheric environments. This patina functions as a physical diffusion barrier, effectively impeding the transport of aggressive species, such as oxygen and corrosive ions, to the underlying steel substrate. Consequently, the long-term corrosion rate is substantially reduced.

The history of weathering steel development dates back to 1928, when it was first introduced as Union-Baustahl by the Vereinigte Stahlwerke AG in Germany [14]. This pioneering effort was followed by the commercial launch of the first trademarked weathering steel, COR-TEN™ steel, by the United States Steel Corporation in the early 1930s (specifically, 1933). The material was originally optimized and marketed for demanding applications, such as railway wagons. The comprehensive findings and mechanistic understanding presented herein contribute significantly to the broader knowledge base of atmospheric corrosion phenomena and provide actionable insights for material selection and maintenance practice.

2.1 Role of Alloying Elements in Patina Formation and Corrosion Resistance

The composition and morphology of the protective layer are fundamentally governed by the presence of specific alloying elements, namely Copper (Cu), Chromium (Cr), Nickel (Ni), Phosphorus (P), Silicon (Si), and Manganese (Mn), each contributing distinct physicochemical mechanisms that collectively enhance the overall corrosion resistance performance [13,15].

Extensive research conducted over the past several decades has established copper as the most critical alloying element in weathering steel formulations, with investigations demonstrating that even minimal additions (approximately 0.05 wt%) can substantially improve atmospheric corrosion resistance [16]. The protective mechanism attributed to copper involves multiple concurrent processes, including the modification of cathodic oxygen reduction kinetics, the retardation of anodic dissolution reactions through enrichment at the metal/electrolyte interface, and the promotion of beneficial goethite (α-FeOOH) formation in the internal rust layer [16]. Furthermore, recent studies have revealed that copper(I) ions can substitute for iron(III) in the magnetite (Fe_3O_4) crystal structure, resulting in excessive negative charge

distributions that contribute to enhanced cation selectivity when chloride ions are present in the corrosive environment [16].

The role of phosphorus in weathering steel formulations has been extensively investigated, despite its generally adverse effects on mechanical properties when present in conventional steel compositions [16]. Research has demonstrated that the synergistic combination of copper and phosphorus effectively promotes the distribution of protective α-FeOOH phases within the inner rust layer while simultaneously inhibiting the formation of less protective magnetic phases such as Fe_3O_4 and γ-Fe_2O_3 [16]. The protective mechanism of phosphorus is attributed to its oxidation to phosphate ions (PO_4^{3-}), which exhibit strong complexing behavior with hydrogen ions and function as effective corrosion inhibitors by reducing both cathodic hydrogen evolution rates and anodic dissolution kinetics [16].

Chromium additions to weathering steels have been shown to significantly influence the morphological characteristics of the protective rust layer, particularly through the promotion of fine α-FeOOH crystal formation that results in enhanced structural density [17]. Investigations utilizing advanced characterization techniques have revealed an inverse linear correlation between chromium concentration and the degree of short-range ordering in α-FeOOH crystals, suggesting that chromium enrichment leads to more disordered crystal structures that may contribute to enhanced protective properties [17].

Recent studies on the role of alloying elements on the corrosion and patina formation of the weathering steels revealed that the combination of niobium (Nb) and boron (B) provides a synergistic effect that enhances the corrosion protection of the weathering steels [13]. This elemental combination is vital for optimizing patina structure. Small additions of Nb accelerate the formation of the dense Goethite (α-FeOOH) phase. Trace amounts of Boron further stabilize this protective layer in saline environments, effectively reducing the presence of deleterious phases like Akaganeite.

Nickel is a critical alloying element in weathering steel, primarily utilized to mitigate the phenomenon of hot shortness, a defect typically induced by copper enrichment during the rolling process [15]. Beyond its metallurgical benefits, Ni significantly enhances the steel's durability in chloride-rich marine atmospheres.

The primary mechanism for this improved resistance is the modification of the rust layer’s electrochemical properties through ion selectivity. Nickel ions frequently incorporate into the corrosion products, forming complex compounds such as $FeNi_2O_4$ [15]. This integration enhances the negative charge density on the surface of the inner rust layer. Consequently, the rust layer undergoes a functional transformation toward cation selectivity. This transition enables the patina to effectively repel aggressive chloride anions (Cl^-) from the metal interface, effectively sequestering them within the outer rust layer and preventing penetration to the substrate [15].

Furthermore, Ni content is directly correlated with patina density. Increased concentrations of Ni promote the formation of smaller, more densely packed corrosion products by providing high-surface-area nucleation sites for iron hydroxyl oxides. This results in a refined grain

structure within the rust layer, which acts as a superior physical barrier against atmospheric moisture and pollutants [15].

While Silicon (Si) is a standard constituent in weathering steel formulations, its specific influence on long-term atmospheric corrosion resistance remains a subject of ongoing investigation [15]. Recent primary sources lack an explicit consensus on Si's isolated role; however, developmental research into chromium (Cr) reduction has yielded significant insights into its effects when co-alloyed [18].

Notably, in high-chromium alloys such as A1010, the addition of 2% Si to steels containing 7% or 9% Cr has been found to be significantly detrimental. Laboratory-based cyclic corrosion testing indicated that at these elevated concentrations, Si impairs the stability of the protective oxide film, leading to higher corrosion rates. This suggests that the benefits of Si are highly dependent on the overall alloy chemistry and the specific concentration thresholds maintained within the matrix [18].

Manganese (Mn) serves as a universal alloying element in weathering steel [15], contributing to both mechanical strength and the early-stage development of the protective patina. In the initial stages of atmospheric exposure—particularly within simulated coastal-industrial environments—Mn tends to enrich within the outer rust layer. Similar to the behavior observed with Copper (Cu), Mn facilitates the development of cation selectivity. Mechanistically, Mn may incorporate into the magnetite (Fe_3O_4) lattice to form manganese ferrites ($MnFe_2O_4$) [16]. This chemical modification strengthens the negative charge of the inner rust layer. By enhancing this electrostatic barrier, Mn prevents the migration of corrosive anions like Cl^- toward the metal matrix, thereby maintaining the integrity of the underlying steel even in environments with high salinity [16].

Despite the substantial progress achieved in understanding individual alloying element effects, several critical gaps remain in the current state of knowledge regarding the complex interactions between multiple alloying elements and their collective influence on patina formation kinetics and long-term protective efficacy. Existing models typically focus on simplified systems or individual element effects, failing to adequately capture the synergistic behaviors that occur in commercial weathering steel compositions under realistic atmospheric exposure conditions. Furthermore, limited quantitative frameworks exist for predicting the temporal evolution of patina characteristics as functions of both alloy composition and environmental variables, particularly in aggressive industrial and marine environments where chloride induced degradation mechanisms become dominant.

2.2 Selection of Weathering Steel Grades for Bridge Applications

The selection of weathering steel (WS) for highway bridge construction requires a critical evaluation of mechanical performance, specifically yield strength, fracture toughness, and weldability, alongside atmospheric corrosion resistance. This balance is particularly vital in aggressive environments where the maintenance of conventional protective coatings is economically impractical or technically unfeasible.

In 1941, ASTM A242 was published as the first standard for WS [19]. In 1968, WS were further classified into two main categories based on phosphorus content: high P (0.07-0.15 wt.%) and low P (<0.04 wt.%). Since the second category of WS has a low P content, it is less resistant to atmospheric corrosion; ASTM A588 was introduced to standardize these low-P alternatives [20]. **Table 2-1** shows the chemical compositions of WS in ASTM A242 and ASTM A588.

Table 2-1. The chemical compositions of WS in ASTM A242 and ASTM A588 (wt.%).

WS	C	Mn	P	S	Si	Cu	Ni	Cr	V	Nb	Mo
ASTM A242	< 0.15	<1.00	<0.15	<0.05	-	>0.20	-	-	-	-	-
ASTM A588 Grade A	<0.19	0.80-1.25	<0.030	<0.030	0.3-0.65	0.25-0.40	<0.40	0.40-0.65	0.02-0.10	-	-
ASTM A588 Grade B	<0.20	0.75-1.35	<0.030	<0.030	0.15-0.50	0.20-0.40	<0.50	0.40-0.70	0.01-0.10	-	-
ASTM A588 Grade K	<0.17	0.50-1.20	<0.030	<0.030	0.25-0.50	0.3-0.50	<0.40	0.40-0.70	-	0.005-0.05	<0.10

For newer construction, ASTM A709, originally published in 1974, is the principal specification for carbon and low-alloy structural steel used in bridge construction in the United States. Over time, the specification has expanded to include weathering steel grades such as 50W, as well as later-developed High Performance Steel (HPS) grades including HPS 50W, HPS 70W, and HPS 100W [21]. The ASTM A709 specification encompasses carbon and low-alloy steel structural shapes, plates, and bars intended for use in bridges. Grades designated with the suffix "W" are engineered to provide atmospheric corrosion resistance approximately two times that of carbon structural steel with copper supplementation.

In Canada, atmospheric corrosion-resistant (weathering) steels are designated with the suffix "AT," where "A" denotes atmospheric corrosion resistance and "T" indicates that the steel has been Charpy V-notch impact tested, confirming adequate notch toughness at low service temperatures; these grades are broadly equivalent to the U.S. weathering steels ASTM A588 or ASTM A709 Grade 50W, where the "W" stands for weathering steel. This is a common source of confusion, because in the Canadian system the "W" suffix means something quite different: grades such as "WT" are weldable, impact-tested carbon steels—the "W" denoting weldability rather than weathering resistance, and correspond to the toughness-qualified grades in ASTM A709 carrying the "T" (or "F") suffix rather than the "W" weathering designation. In short, the Canadian "AT" grades map to the U.S. "W" weathering steels, whereas the Canadian "W/WT" grades map to the plain weldable, impact-tested "T/F" grades, so care must be taken not to equate the Canadian and American "W" designations.

This category includes both conventional weathering steels and the newer generation of High-Performance Steels (HPS). The HPS grades emerged from a collaborative research initiative established in 1992 by the Federal Highway Administration (FHWA), the U.S. Navy, and the American Iron and Steel Institute (AISI). The primary objective was to develop grades that

retain the characteristic self-passivating rust layer of traditional WS while significantly enhancing strength, weldability and toughness.

Nowadays, steelmaking companies in diverse countries manufacture their own WS under various brand names, such as Cor-Ten (US steel), PATINAX (Thyssen Krupp), Mayari (Bethlehem Steel), Atmofix (Czech Republic), and ENSACOR (Spain) [1]. **Table 2-2** lists the most used weathering steels around the world and compares their designation in different regions. The presented comparison shows that most of the currently used weathering steels across the world are developed based on ASTM A242 and ASTM A588 alloys.

Table 2-2. Mostly used weathering steels around the world (US: The United States of America, UK: The United Kingdom of Britain, EU: European Union, AU: Australia) and a comparison of their designations.

US	UK/EU	Japan	China	AU	Key Features/Applications
ASTM A242 (Type 1)	EN S355J0WP	JIS SPA-H	GB/T Q235NH		Original COR-TEN A, housing, freight cars, architectural. Higher phosphorus.
ASTM A242 (Type 2/Corten A)	EN S355J2W	JIS SPA-C	GB/T Q345NH		Thicker plates, urban furnishing, passenger ships, cranes. Lower phosphorus.
ASTM A588 (Grade A)	EN S355J2W	JIS SPA-C	GB/T Q345NH	AS/NZS 3678 WR350A (L0, L20)	Higher strength, welded bridges, structural shapes, plates, bars. Higher phosphorus (Type A Aus).
ASTM A588 (Grade B)	EN S355J2W	JIS SPA-C	GB/T Q345NH	AS/NZS 3678 WR350B (L0, L20)	Higher strength, welded bridges, structural shapes, plates, bars. Lower phosphorus (Type B Aus), better weldability.
ASTM A588 (Grade C)					
ASTM A588 (Grade K)					
ASTM A606					Thin sheet, strip, coil, structural and miscellaneous purposes, enhanced corrosion resistance.
ASTM A709, 50W					Structural steel in bridges, high strength, low alloy, high corrosion resistance index.
ASTM A847					Minimum yield 50 ksi, tensile 70 ksi. Limited information.

US	UK/EU	Japan	China	AU	Key Features/Applications
ASTM A871,65					High strength plate, transmission and lighting poles, aesthetic alternative to galvanized.
	EN S355J0W				Equivalent to Corten B, impact test 0°C.
	EN S355K2W				Similar to S355J2W, higher impact toughness at -20°C.
	EN S355J4W				Very low temp applications, impact test -40°C.
	EN S355J5W				Extremely low temp applications, impact test -50°C.
	EN S235J0W/ J2W				Lower strength grades.
	EN S420J2W/ S460J2W				Higher strength grades, used in bridges.
	PATINAX 355P (S355J2W P+N)				Equivalent to Corten A, higher phosphorus, higher corrosion resistance.
	PATINAX 355 (S355J2W +N)				Equivalent to Corten B.
	PATINAX 275PK (S355J2W P)				Thinner cold-rolled sheet, higher phosphorus.
		JIS G3114 SMA40 0AW			Weldable, no low-temp impact test requirement.
		JIS G3114 SMA40 0BW			Weldable, impact test 0°C min 27J.
		JIS G3114 SMA40 0CW			Weldable, impact test at lower temp than BW.

US	UK/EU	Japan	China	AU	Key Features/Applications
			GB/T Q295NH		Welding weathering steel.
			GB/T Q355NH		High tensile strength, good weldability, low temp impact toughness.
			GB/T Q460NH/Q500 NH/Q550NH		Higher strength welding weathering steels.
			GB/T Q265GNH/Q29 5GNH/Q310G NH/Q355GNH		High weathering steel grades.
				AS/NZS 1594 HW350A	Hot-rolled flat product, good formability.
				AS/NZS 1595 CW300A	Cold-rolled, smoother finish, tighter tolerances.

The alloys mentioned above can be grouped based on their main features and chemical composition as shown in **Table 2-3.**

Table 2-3. Categorizing the weathering steels based on their alloying composition and main features.

Alloy Family & Included Designations	Typical Chemical Composition (wt.%)	Main Features & Applications
High-Phosphorus Weathering Steels (Corten A Equivalents): ASTM A242 (Type 1); EN S355J0WP; JIS SPA-H; GB/T Q235NH; PATINAX 355P / 275PK	C : ≤ 0.15; Mn: ≤ 1.00; P: 0.06 - 0.15; S: ≤ 0.04; Si: 0.25 - 0.75; Cu: 0.25 - 0.55; Cr: 0.30 - 1.25; Ni: ≤ 0.65	Original COR-TEN A properties. Excellent corrosion resistance driven by high phosphorus. Best for thinner plates, architectural facades, housing, and cold-rolled sheets. Limited weldability.
Low-Phosphorus Weathering Steels (Corten B Equivalents): ASTM A242 (Type 2); ASTM A588 (Grades A/B); EN S355J0W, S355J2W, S355K2W; JIS SPA-C, G3114 SMA400; GB/T Q345NH; AS/NZS 3678 WR350A/B	C: ≤ 0.19; Mn: 0.80 - 1.25; P: ≤ 0.04; S: ≤ 0.04; Si: 0.15 - 0.65; Cu: 0.25 - 0.40; Cr: 0.40 - 0.65; V: 0.02 - 0.10	Lower phosphorus allows for thicker plate rolling and excellent weldability. Used for heavy load bearing structures, welded bridges, passenger ships, and cranes. Includes standard impact-tested grades (down to -20°C).
High-Strength & Specialized Weathering Steels: ASTM A709 (50W); ASTM A871 (65); EN	C: ≤ 0.12; Mn: 1.00 - 1.50; P: ≤ 0.03; S: ≤ 0.03; Si: 0.20 - 0.60; Cu: 0.25 - 0.50; Cr: 0.40 - 0.80; Micro-alloyed with Nb, V, Ti	Advanced structural grades utilizing micro-alloying for superior strength-to-weight ratios (Yields 420–550 MPa). Used in

S420J2W, S460J2W; GB/T Q460NH, Q500NH, Q550NH		transmission poles, high-stress bridges, and large-scale infrastructure.
Extreme Low-Temperature Grades: EN S355J4W; EN S355J5W	C: ≤ 0.16; Mn: 0.50 - 1.50; P: ≤ 0.03; S: ≤ 0.02; Si: ≤ 0.50; Cu: 0.25 - 0.55; Cr: 0.40 - 0.80; Ni: ~0.50 (for toughness)	Very specific European grades engineered with tighter sulfur controls and nickel additions to guarantee Charpy V-Notch impact toughness at extreme temperatures (-40°C for J4, -50°C for J5).
Thin Sheet, Coil & Pipe Grades: ASTM A606; ASTM A847; AS/NZS 1594 HW350A; AS/NZS 1595 CW300A	C: ≤ 0.15; Mn: 0.50 - 1.20; P: ≤ 0.04; S: ≤ 0.04; Si: ≤ 0.50; Cu: 0.20 - 0.40; Cr: 0.30 - 0.60	Optimized for formability. Cold-rolled and hot-rolled flat products with tighter tolerances, smoother finishes, and good atmospheric resistance. Used in structural tubing and miscellaneous aesthetic shapes.

The mechanical distinctions between conventional and HPS grades are summarized in **Table 2-4.**

Table 2-4. Mechanical properties and characteristics of ASTM A709 weathering steel grades [21].

Grade	Yield Strength (minimum)	Tensile Strength	Processing & Characteristics
50W	50 ksi (345 MPa)	70 ksi (485 MPa) min	Conventional weathering steel grade widely utilized in standard bridge applications (13).
HPS 50W	50 ksi (345 MPa)	70 ksi (485 MPa) min	Produced via hot rolling or controlled rolling (up to 4 inches). Optimized to meet rigorous toughness protocols (12).
HPS 70W	70 ksi (485 MPa)	85-110 ksi (585-760 MPa)	Processed via Quenching and Tempering (Q&T) or Thermal Mechanical Controlled Processing (TMCP). Exhibits superior ductility at low service temperatures (60F for Zone 3) and improved weldability (12).
HPS 100W	100 ksi (690 MPa)	Not Specified	High-Performance Steel grade that was in development (12).

A critical advancement in HPS grades is the reduction in carbon equivalents, which directly correlates to improved weldability. For instance, HPS 70W permits reduced minimum preheat and interpass temperatures compared to conventional Grade 70W, thereby mitigating fabrication costs and the risk of hydrogen induced cracking. Furthermore, the elevated yield strengths of HPS grades allow for the design of lighter structural members and shallower girders, optimizing the strength-to-weight ratio of the superstructure [1].

For environments where chloride exposure exceeds the passive limits of standard weathering steels, ASTM A1010 offers a viable alternative. Classified as a higher strength martensitic stainless steel, this material is specified for structural, pressure vessel, and architectural applications, meeting the mechanical rigor of ASTM A709 bridge steels while offering superior corrosion kinetics. ASTM A1010 is nominally defined by a Chromium (Cr) content of 12% (specifically 10.5% < Cr < 12.5%). The alloy typically includes up to 1.50% Nickel (Ni) and 1.00% Silicon (Si) [18]. Structurally, it exhibits a dual phase microstructure comprising ferrite and martensite. To achieve the requisite mechanical properties for structural applications, the material undergoes a tempering heat treatment [22]. The fundamental divergence between ASTM A1010 and conventional WS lies in the passivation mechanism:

- Conventional WS: Relies on the gradual development of a protective patina, primarily composed of nanophase goethite (α-FeOOH).
- ASTM A1010: Achieves protection through the immediate formation of a thin, continuous chromium oxide film.

Accelerated corrosion testing indicates that ASTM A1010 exhibits a corrosion rate approximately one tenth to one fifteenth that of ASTM A588. Consequently, it is the preferred material specification for high chloride environments, such as marine crossings or highways subject to heavy deicing salt application, where the formation of stable goethite on standard WS is inhibited.

While ASTM A1010 is available in standard structural grades, Grade 40 (275 MPa) and Grade 50 (345 MPa), its initial material cost is significantly higher than ASTM A709 50W [23]. Therefore, its selection is typically justified through Life Cycle Cost Analysis (LCCA), where the elimination of coating maintenance offsets the higher upfront capital expenditure [18].

The efficacy of conventional weathering steel grades, primarily ASTM A242 (Type 2) and ASTM A588, is contingent upon the formation of patina. The thermodynamic stability of this layer depends on specific environmental and structural parameters. When these thresholds are breached, the protective mechanism fails, and corrosion rates escalate to levels seen in unalloyed carbon steels [18]. The alloying strategies that impart atmospheric corrosion resistance introduce secondary limitations in fabrication and structural performance [12].

Weathering steels typically exhibit higher carbon equivalent values (CEV) than conventional structural steels. This increases susceptibility to hydrogen induced cracking, necessitating stricter control of preheat temperatures, interpass temperatures, and consumable hydrogen levels during welding [1]. Phosphorus is highly effective in enhancing atmospheric corrosion resistance but readily segregates to grain boundaries. At elevated levels, as in A242 Type 1, phosphorus can significantly reduce fracture toughness, limiting its use to thin sections or noncritical structural applications [1]. The rough surface morphology of a stabilized patina introduces distributed micro stress concentrations. This reduces fatigue resistance relative to smooth, unweathered steel. Accordingly, AASHTO design specifications classify UWS as Category B, compared with Category A for comparable carbon steel members [24].

3 Corrosion Mechanism and Protection Principles of Weathering Steels

3.1 Anodic Reaction and Oxide Formation

The deterioration of ferrous metals in aqueous environments is a complex, multistage process that is fundamentally initiated by the anodic dissolution of iron. This is followed by a cascade of chemical and electrochemical transformations that eventually result in the accumulation of corrosion products commonly referred to as rust, or patina in the case of weathering steels. The reactions proceed at the metal/electrolyte interface, where environmental variables such as pH, dissolved oxygen concentration, chloride content, moisture, temperature, and overall water chemistry exert a controlling influence on the rate and nature of corrosion.

The first stage in this process is anodic metal dissolution. At discrete anodic sites on the surface of steel, metallic iron undergoes oxidation to release ferrous ions (Fe^{2+}) and electrons. This step is described by the fundamental electrochemical reaction [25]:

$$Fe \rightarrow Fe^{2+} + 2e^{-} \quad (3\text{-}1)$$

The overall rate of this anodic process is strongly coupled to the kinetics of the associated cathodic reactions, which serve to consume the liberated electrons [26]. The anodic potential (E_a) can be expressed using standard electrochemical relationships involving the anodic Tafel slope (b_a) and the reversible anodic current density ($i_{a,0}$) with a rate expression:

$$i_a = i_{a,0} \exp\left[\frac{\alpha_a n F \eta}{RT}\right] \quad (3\text{-}2)$$

Where i_a is the anodic current density, $i_{a,0}$ is the anodic exchange current density, α_a is the anodic charge transfer coefficient, η is the activation overpotential, *R* is the universal gas constant, and *T* is the absolute temperature. When a dry metallic surface is suddenly wet, the anodic dissolution rate is often temporarily accelerated. The electrons generated at the anode are consumed at the cathode primarily by the reduction of dissolved oxygen in the electrolyte, although in some cases ferric oxides contained within preexisting rust layers may act as electron acceptors [27].

Following anodic dissolution, the ferrous ions released into the electrolyte are not stable in neutral or aerated environments. Instead, they undergo hydrolysis, oxidation, and precipitation to form a variety of hydroxide and oxide phases. Initially, ferrous ions may react with water molecules to form ferrous hydroxide [28]:

$$Fe^{2+} + 2H_2O \rightarrow Fe(OH)_2 + 2H^{+} \quad (3\text{-}3)$$

This hydrolysis process produces protons, which acidify the local electrolyte and thereby

enhance further metal dissolution [28]. In the presence of dissolved oxygen, ferrous hydroxide is rapidly oxidized to ferric hydroxide:

$$2Fe(OH)_2 + H_2O + ½O_2 \rightarrow 2Fe(OH)_3 \quad (3\text{-}4)$$

The ferric hydroxide can accumulate on the metal surface and, depending on its crystallinity and compactness, act as a protective or semi protective barrier. However, the protective ability of these layers is inconsistent, as many of them are porous and permit continued electrolyte penetration.

Over time, the ferric hydroxides are transformed into a suite of more stable iron oxides and oxyhydroxides that constitute the mature rust layer. The specific phases that develop depend on the chemistry of the surrounding electrolyte, the pH, chloride concentrations, temperature, and the metallurgical properties of the steel [28]. Goethite (α-FeOOH) is a relatively stable oxyhydroxide that tends to form compact and partially protective layers [29]. Lepidocrocite (γ-FeOOH), on the other hand, is more porous and less protective, often formed in environments that remain moist and aerated [29]. In chloride rich conditions, akaganeite (β-FeOOH) is commonly observed, as chloride ions both catalyze the dissolution of iron and stabilize ferric hydroxy complexes [28]. Beneath these outer layers, magnetite (Fe_3O_4), a mixed valence oxide containing both Fe^{2+} and Fe^{3+}, may form, while maghemite (γ-Fe_2O_3) is often produced by the further oxidation of magnetite [29]. Archaeological investigations have frequently revealed microstructures in which magnetite and maghemite are embedded within a matrix of goethite, showing the dynamic redox cycling of iron over long timescales [29].

The persistence of corrosion is significantly enhanced by the redox cycling capacity of iron oxides and oxyhydroxides. For instance, γ-FeOOH (lepidocrocite) can be reduced at potentials below –0.2 V (SHE) to regenerate Fe^{2+} ions [27]. These ions then react with additional γ-FeOOH to form magnetite:

$$Fe^{2+} + 2\gamma\text{-}FeOOH \rightarrow Fe_3O_4 + 2H^+ \quad (3\text{-}5)$$

Magnetite, in turn, may be oxidized back to γ-FeOOH or maghemite, thereby establishing a cyclic process where corrosion products themselves act as redox mediators [25]. This cycle allows for continuous anodic dissolution of the underlying metal, even in environments where oxygen availability is limited, such as waterlogged soils. The process is shown schematically in **Figure 3-1**.

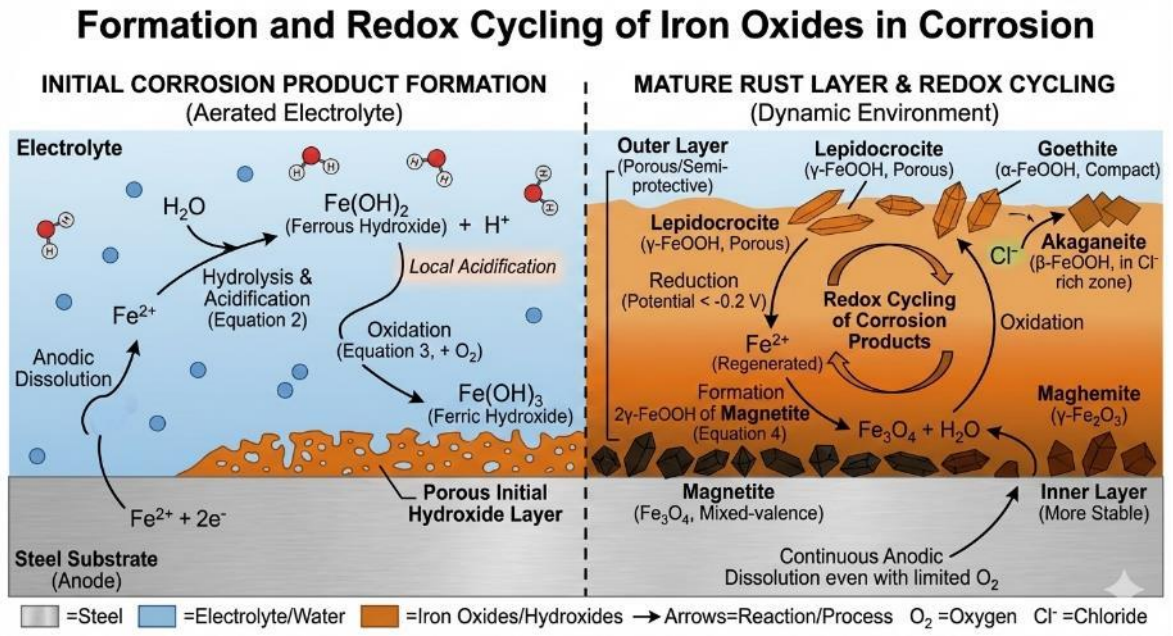

Figure 3-1. Schematic of anodic reactions in the corrosion process of iron.

The severity of corrosion is ultimately dictated by the interaction between environmental chemistry and electrochemical mechanisms. Acidic environments accelerate the dissolution of iron, while chloride ions act as potent promoters of localized corrosion and akaganeite formation [28]. The availability of moisture and oxygen controls the relative balance between ferrous and ferric phases, while the presence of redox active rust compounds ensures that corrosion can persist even under oxygen deficient conditions. Taken together, these processes illustrate the complexity of corrosion mechanisms in aqueous environments and reveal the necessity of considering environmental influences in the design and maintenance of ferrous infrastructure.

3.2 Oxygen Reduction as the Dominant Cathodic Reaction

The cathodic process that balances the anodic dissolution of iron in aqueous environments is most often the reduction of oxygen [30]. A wide range of experimental and theoretical studies confirm that the oxygen reduction reaction (ORR) is the dominant cathodic pathway for corrosion of iron and steel in neutral and alkaline environments where pH exceeds 4. Under such conditions, hydrogen evolution is thermodynamically less favorable, and the electrochemical reduction of oxygen controls the cathodic current.

The overall cathodic oxygen reduction reaction in neutral or alkaline media is expressed as [26]:

$$O_2 + 2H_2O + 4e^- \rightarrow 4OH^- \quad (3\text{-}6)$$

This four-electron process provides the cathodic current that balances anodic iron dissolution. In many cases, intermediate steps involving hydrogen peroxide (H_2O_2) are observed:

$$O_2 + 2H^+ + 2e^- \rightarrow H_2O_2 \quad (3\text{-}7)$$
$$H_2O_2 + 2e^- \rightarrow 2OH^- \quad (3\text{-}8)$$

The formation and subsequent reduction of H_2O_2 are highly dependent on the electronic properties and catalytic sites within the rust layer [31].

In aqueous environments with pH above 4 like atmospheric corrosion, iron surfaces are almost universally covered with a passive film or porous rust scale. As a result, oxygen reduction occurs predominantly within the rust layer rather than directly at the bare metal/electrolyte interface [30]. The rust acts as an extended cathode, where Fe^{2+} states provide electron donors to catalyze O_2 reduction. The Fe^{2+}/Fe^{3+} ratio within the rust layer is therefore a critical factor, as fully oxidized rust is electronically insulating, while partially reduced rust is conductive and highly active.

Mechanistic studies reveal that oxygen molecules diffuse through pores in the rust layer and are reduced at oxide/electrolyte interfaces enriched with Fe^{2+}. The kinetics of this process are governed by both charge transfer and mass transport. In thick electrolyte films, diffusion of oxygen through the rust or electrolyte becomes the rate-limiting step, whereas in thin electrolytes formed during drying cycles, charge transfer on reduced oxides becomes dominant. Fick's law is used to describe the limiting current density (i_{lim}), which is inversely proportional to the thickness of the diffusion layer [32].

$$i_{lim} = \frac{D_w n F c_i}{d} \quad (3\text{-}9)$$

where F is the Faraday's constant (96 485 C/mol), D_w is the diffusion coefficient of oxygen in water (1.90×10^{-9} m^2/s), n is the number of electrons transferred per reaction step, C_i is the bulk oxygen concentration and d is the thickness of diffusion layer.

Experimental evidence supports the internal reduction mechanism. Oxygen reduction current densities observed during corrosion often reach 0.5–1.0 mA cm^{-2} [33], which far exceed what could occur on the geometric surface alone. This indicates that the effective electroactive surface area is orders of magnitude larger, owing to the highly porous nature of rust scales, which can have internal surface areas of 50 m^2/g or more [33]. Marker studies using silver deposition have confirmed that electrochemical activity occurs inside the rust, with silver nuclei found atop α-FeOOH crystals. Permeation experiments with electroactive probes, such as $[Fe(CN)_6]^{3-}$, demonstrate negligible transport across the entire rust layer, confirming that the cathodic activity is localized within the porous oxide and not at the metal/oxide boundary [30].

The catalytic role of Fe^{2+} state is essential. Reduction of Fe^{3+} to Fe^{2+} within α-FeOOH generates electron donors and enhances the semiconducting properties of the oxide [30]. Magnetite (Fe_3O_4), formed during partial reduction, is particularly conductive and provides extended electron pathways. The presence of magnetite strongly enhances oxygen reduction, as it allows cathodic reactions to occur spatially separated from the anodic dissolution of metal.

Re-oxidation of Fe^{2+} sites during drying stages reverses this effect, lowering conductivity and reducing oxygen reduction rates.

3.3 Influence of Electrolyte Parameters on the Corrosion of Metals Under Thin Film Conditions

3.3.1 Electrolyte Volume and Corrosion Control

Electrolyte volume, expressed through the thickness of the water layer, has a direct influence on corrosion kinetics and oxide formation on metallic surfaces [32]. For steels exposed to atmospheric corrosion, the electrolyte layer expands during periods of elevated moisture or rain and snow [31]. These cyclic variations alter both anodic dissolution and cathodic oxygen reduction. The change is schematically shown in **Figure 3-2.**

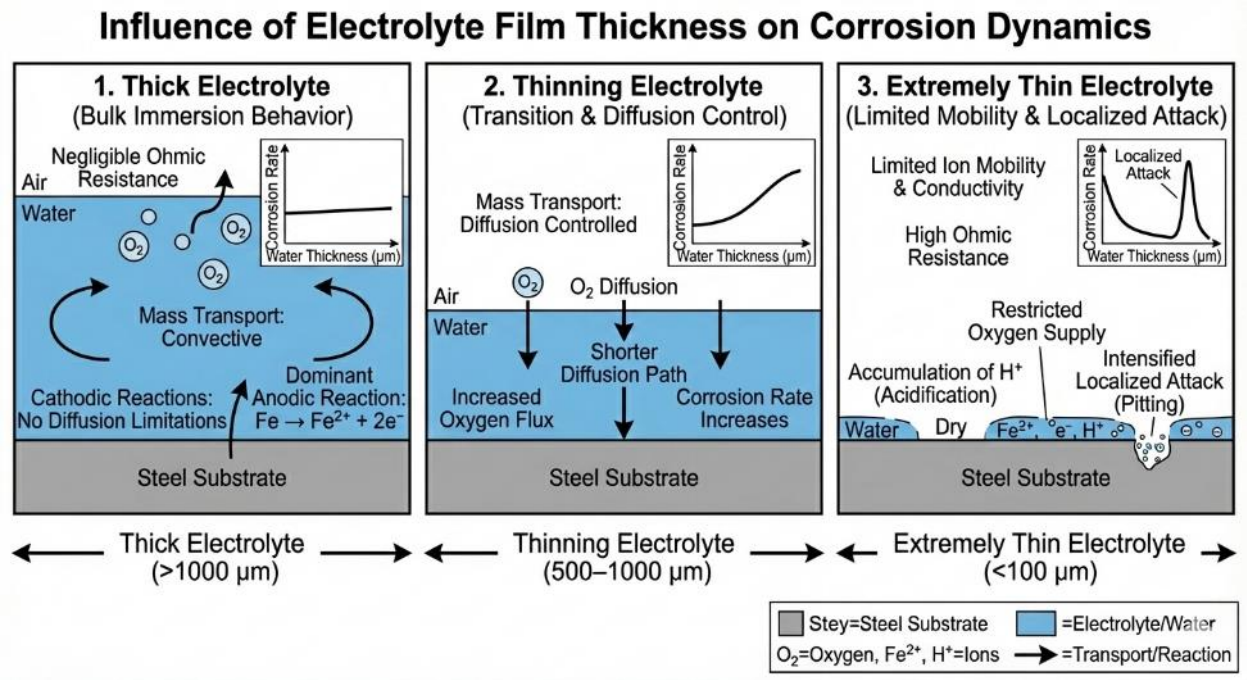

Figure 3-2. The effect of solution thickness on corrosion rate.

When the electrolyte layer is sufficiently thick, typically several millimeters, the system behaves similarly to bulk immersion conditions. Ohmic resistance is negligible, and mass transport is primarily convective, allowing cathodic reactions to proceed without significant diffusion limitations. For steel, the dominant anodic reaction in both bulk and thin films remain metal dissolution.

As the electrolyte layer becomes thinner and approaches the scale of the natural convection boundary layer (approximately 500–1000 μm in ferrous systems), mass transport transitions from convection to diffusion control. Further thinning produces a diffusion limited regime where corrosion becomes increasingly controlled by oxygen transport. In this range, corrosion rates often increase as the water layer thins, because oxygen flux to the metal surface improves when the diffusion path is shortened.

At extremely low film thicknesses, however, ion mobility and electrical conductivity decline sharply. The limited electrolyte volume restricts the supply of both dissolved oxygen and ionic charge carriers, while the ohmic resistance of the film increases. These conditions reduce the cathodic current and lower the overall corrosion rate. Confinement also promotes the accumulation of dissolved metal ions, leading to acidification near the metal surface and intensifying localized attacks.

3.3.2 Diffusion of Species and Corrosion Kinetics

Non uniform electrolyte geometries introduce additional diffusion gradients. In sessile droplets, the edges remain well oxygenated and act as cathodic zones, while the droplet center becomes oxygen deficient and acts anodically [33,34]. This produces oxygen concentration cells that drive localized metal dissolution and generate characteristic pitting and under deposit corrosion patterns. This is shown schematically in **Figure 3-3**.

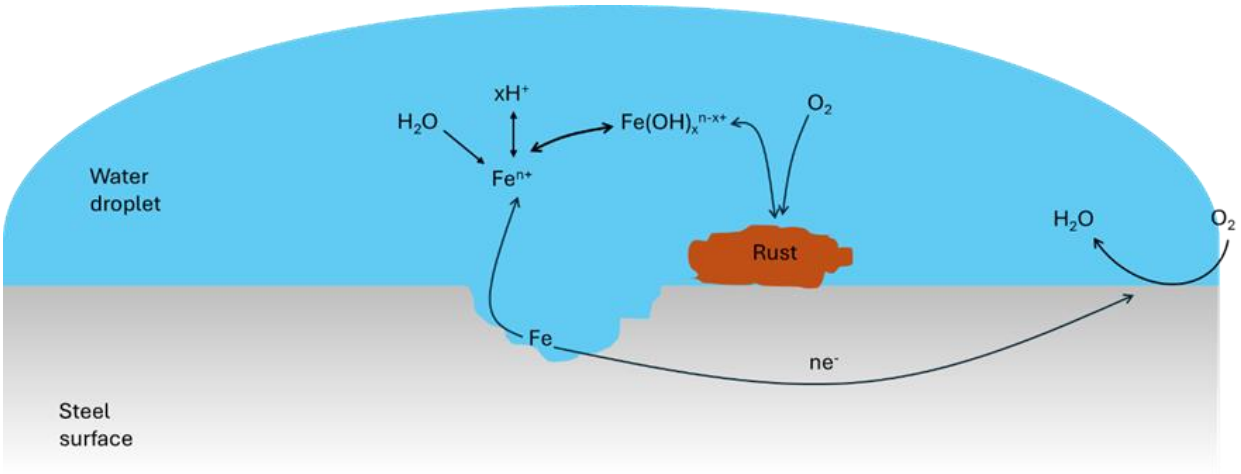

Figure 3-3. Formation of oxygen cell under the low volume electrolyte.

As corrosion proceeds, the formation of rust layers modifies both the reaction front and diffusion pathways. Initially, oxygen reduction occurs directly at the metal surface. With continued oxidation, iron hydroxides and oxyhydroxides accumulate and begin to serve as the primary cathodic interface. Iron(II) ions produced at the metal surface are often oxidized to iron(III) at or within the rust layer. These Fe^{3+} ions subsequently hydrolyze and precipitate as

solid oxyhydroxides such as lepidocrocite (γ-FeOOH). Once a rust layer develops, corrosion may become limited by oxygen diffusion through the corrosion products rather than through the electrolyte film [34].

4 Environmental Suitability and Limitations

4.1 Environmental Classification and the ISO 9223 Framework

The selection of weathering steel is predicated on a quantitative assessment of the site's atmospheric corrosivity. ISO 9223 provides a standardized classification system that categorizes environments based on the first-year corrosion rates (r_{corr}) of standard metallic specimens [35]. These categories (C1 through CX) are determined by the complex interaction of the temperature, relative humidity, sulfur dioxide (SO_2) concentrations, and airborne salinity (chlorides).

4.1.1 ISO 9223 Corrosivity Categories

The following **Table 4-1** summarizes the corrosivity levels and their typical environmental characteristics:

Table 4-1. Corrosivity categories and first-year carbon-steel corrosion rates from ISO 9223:2012 (Tables 1 and 2); the typical-environment examples are illustrative, adapted from ISO 9223 Annexes B–C and general literature. (35).

Category	Corrosivity	First-Year r_{corr} (Carbon Steel) (μm/year)	Typical Outdoor Environments (Temperate Zone)
C1	Very Low	≤ 1.3	Arid or sub-zero zones with negligible pollution (e.g., Antarctica).
C2	Low	$1.3 < r_{corr} \leq 25$	Rural areas and small towns with low SO_2 (< 5 μg/m^3).
C3	Medium	$25 < r_{corr} \leq 50$	Urban/coastal areas with moderate SO_2 (5-30 μg/m^3) or mild chlorides.
C4	High	$50 < r_{corr} \leq 80$	Industrial zones or coastal areas with substantial chloride/de-icing salt exposure.
C5	Very High	$80 < r_{corr} \leq 200$	Industrial/coastal areas with extreme pollution or significant saltwater influence.
CX	Extreme	$200 < r_{corr} \leq 700$	Offshore areas or industrial zones with SO_2 > 250 μg/m^3.

For conventional WS to be technically and economically viable, it must achieve a steady state corrosion rate that ensures structural integrity over the design life without the need for protective coatings.

- **Design Thresholds:** The target steady state corrosion rate for functional WS is typically < 6 μm/year [1]. For C4 this target is ~10x lower than carbon steel and ~2x that of zinc coated steel. If the environmental conditions prevent the patina from stabilizing below this threshold, the material's advantage over carbon steel is lost.
- **Selection Constraints:** Uncoated weathering steel is generally not recommended for environments classified as C3 (Medium) or higher. While inland Europe is frequently categorized as C2, localized pollution or microclimates can quickly elevate a site to C3, necessitating a move toward protective coatings or high-performance alloys [1].
- **Unsuitable Environments:** Applications in C5 (Very High) and CX (Extreme) categories are considered non-viable [7]. Empirical data suggests that if an environment causes a UWS structure to corrode at a rate exceeding 7.5 μm/year (0.3 mils/year), the thermodynamic conditions for a stable, protective oxide coating cannot be maintained [5]. Weathering Steel can be painted and often is, particularly in vulnerable areas such as below expansion joints.

Figure 4-1 shows the corrosion map and corrosivity category created by ICCET in Canada and the U.S. Additional data were added to the figure for Canadian cities from the published article [36]. While most inland locations show a C1–C2 corrosion category, locations near saltwater show corrosion categories of C4 to C5, emphasizing the negative effect of humidity and chloride on corrosion [37]. The salt deposition is also common within 10 kilometers of a sea due to the formation and deposition of salt-bearing aerosols. It has been reported previously that with increasing distance from waterlines; the ISO 9223 category can drop from CX to C4. Compounding the inherent salt risk is salt’s hygroscopic nature, which can result in the formation of liquid droplets from humid air.

It would seem, however, that this mapping originates in large part from marine (sea salt) exposure rather than from de-icing salt application and the associated indirect road-spray exposure that governs most highway bridges. As a result, the map may understate the localized corrosivity experienced by structures spanning or adjacent to salted roadways. A useful Canadian reference point is the Jacques-Cartier Bridge, where field monitoring established a corrosivity level of C3 at a distance of approximately 3.8 m from the roadway; illustrating that road-salt-driven indirect exposure alone can sustain elevated corrosivity classifications well away from the direct line of traffic spray.

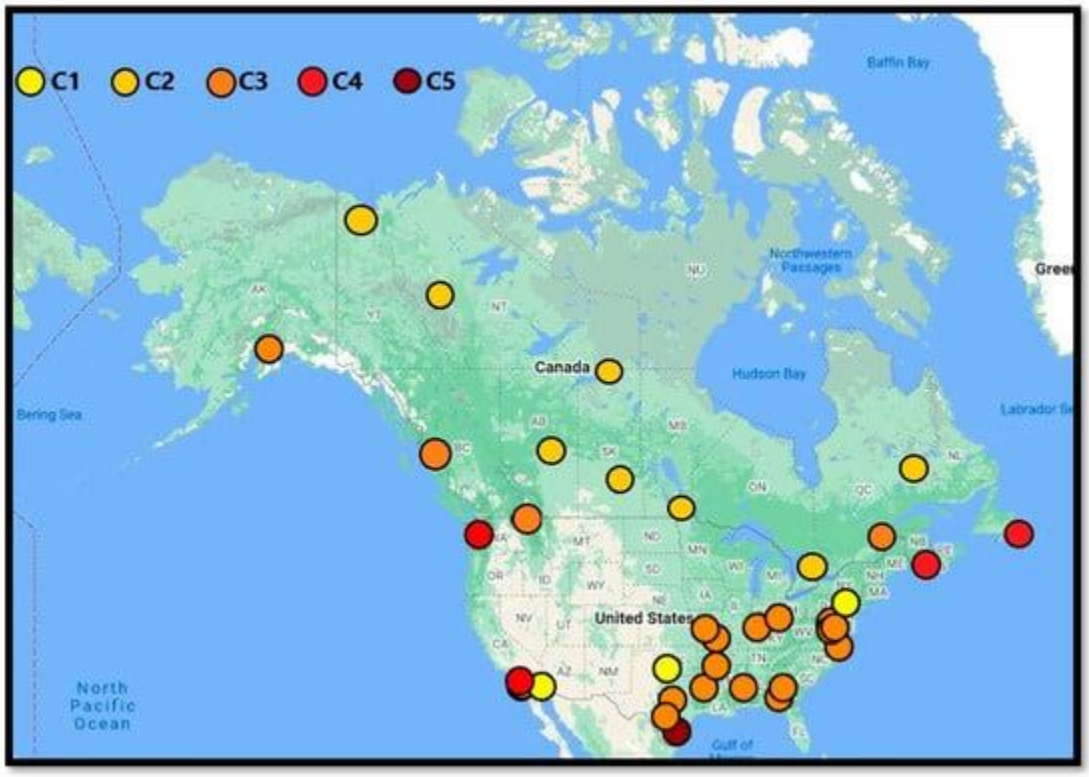

Figure 4-1. ISO 9223 atmospheric corrosivity map of USA and Canada based generated by ICCET; additional data were added to the figure for Canadian cities from article [36].

4.1.2 Factors Driving Corrosivity Escalation

The most fundamental driver of atmospheric corrosion is the Time of Wetness (ToW), defined as the cumulative duration during which a metallic surface is covered by an electrolyte film of sufficient thickness to facilitate electrochemical oxidation. ISO 9223 characterizes ToW across five distinct levels, where Category T5 (> 5,500 hours/year) represents the highest risk profile [4]. This condition is typically observed in damp tropical zones or unventilated, sheltered areas where moisture remains stagnant. Furthermore, corrosion rates exhibit a sharp increase as relative humidity (RH) exceeds critical thresholds, approximately 70% in salt-free environments and decreasing to 55% in salt-laden environments due to the presence of hygroscopic contaminants. For weathering steels, alternate wet/dry cycles are mandatory for the precipitation of a stable, protective oxide patina. Notably, if the steel remains continuously saturated, the protective mechanism fails, and the material corrodes at a rate commensurate with ordinary carbon steel, leading to accelerated section loss [4].In certain circumstances, corrosion rate can be even higher for WS than carbon steels, such as that of Highway 401 in Lancaster Ontario, where validated laboratory models predicted weathering steels thickness loss is almost 42% higher than carbon steel.

Industrial pollution, primarily represented by SO_2 deposition, significantly influences the transition from moderate to high corrosivity categories. When SO_2 dissolves in surface moisture, it undergoes oxidation to form sulfuric acid (H_2SO_4), leading to intense acidification of the electrolyte layer. This chemical shift accelerates the dissolution of the base metal and prevents the formation of a protective patina. High levels of SO_2 pollution, categorized as P3 when deposition exceeds 80–200 mg/m^2/day, lead to unacceptably high corrosion rates and surface pitting [12,38]. However, it is important to note that while SO_2 was a dominant driver in the mid-20th century, modern environmental regulations have drastically reduced its concentration in many regions, thereby lowering the macroenvironmental corrosivity of many former industrial hubs.

Chlorides remain the most aggressive chemical species affecting the performance of structural steels, particularly in coastal or de-iced infrastructure [12]. Proximity to the shoreline introduces airborne marine salts (Cl^-) via wind impingement or salt fog, where corrosivity typically attenuates from CX to C4 as the distance from the shoreline increases. Dominant winds can also affect the microclimate, where for through trusses, winds may reduce salt spray exposure on the windward truss and increase the exposure on the leeward truss.

Standard corrosivity estimations can be significantly understated if the structure's microenvironment is neglected. The local geometry and site conditions often create conditions more severe than the surrounding macroclimate. For instance, the "tunnel effect", characterized by low vertical clearance (< 6.1 m) over roadways, traps salt laden traffic spray that settles on overhead members [4]. This spray cannot be washed away by natural precipitation, leading to localized "poultice" corrosion. Similarly, surfaces sheltered from direct rain washing, such as the interior of girders, often experience higher corrosion rates because pollutants are not naturally rinsed while moisture remains trapped by poor air circulation. Accumulated debris and close-in vegetation further exacerbate these effects by acting as moisture reservoirs and blocking sunlight, thereby prolonging ToW [12].

Finally, escalating global temperatures are projected to drive atmospheric corrosivity through altered environmental variables. Rising temperatures are predicted to increase average humidity by 5% to 10%, potentially causing a structure with a 100-year design life to lose an average of 15 years of service life. In coastal regions, ocean acidification and altered precipitation patterns are expected to accelerate Cl-induced corrosion rates. Recent modeling indicates that these factors may lead to structural failures occurring 3% to 31% earlier than historically anticipated, necessitating more robust maintenance and material selection strategies for future infrastructure resilience [12].

4.2 Impact of Chlorides and De-icing Salts

Chlorides, derived predominantly from marine aerosols and the application of de-icing salts, represent the most significant threat to the long-term structural performance of weathering steel (WS) [18]. Although WS is engineered to develop a protective, adherent patina in most atmospheric environments, high chloride concentrations fundamentally disrupt the electrochemical and chemical processes required for this barrier to stabilize.

4.2.1 De-icing in Canada

For most of the bridges on the highways and within the municipalities, de-icing is the main source of the chloride. The Canadian provinces adopt different de-icing procedures during winter (

Table 4-2). However, most of them follow the idea that the maintenance of Canadian highways and bridges during winter months necessitates a transition from reactive snow clearing to a proactive, "clean surface" philosophy. This strategic approach is anchored in the prevention of a physical bond between frozen precipitation and the pavement substrate, a process primarily achieved through anti-icing pre-treatments. By applying liquid freezing point depressants, such as sodium chloride brines, to the road surface in anticipation of a storm event, maintenance crews can ensure that subsequent mechanical removal remains significantly more efficient. On high-speed corridors, particularly within Ontario’s 400-series network and British Columbia’s Mountain passes, this is often supplemented by pre-wetting solid salts to reduce "scatter" and ensure the material remains active within the driving lanes.

Bridge structures represent a unique challenge within this framework due to their exposure to ambient air on both the upper and lower surfaces, causing deck temperatures to drop more rapidly than adjacent roadways. Consequently, provincial standards prioritize bridge decks for more frequent chemical applications. In these microenvironments, the selection of materials is critical; while sodium chloride remains the standard for general use down to -10°C, colder temperatures or high-priority structural elements often require the use of calcium or magnesium chloride, which remain effective to -25°C. Furthermore, to mitigate the long-term risk of chloride-induced oxidation on steel girders and reinforcing steel, corrosion inhibitors and specialized non-corrosive de-icers are integrated into the maintenance cycle (**Table 4-3**). The operational differences across jurisdictions and the material selection based on environmental conditions are summarized in **Tables 4-2** and **4-3**.

Table 4-2. Comparative analysis of provincial maintenance standards.

Province	Core Philosophy & Priorities	De-Icing Methods & Materials	Mandated Completion (Post-Storm)
Ontario (MTO)	Bare Pavement: High-volume highways (Class 1) prioritized. 24/7 continuous operations.	Pre-wetting salt (NaCl) with liquid brine. Potassium acetate/Calcium chloride for extreme cold.	4–8 hours for Class 1 (major highways) to reach bare pavement.
British Columbia (MoTI)	Service Level Standards: Class A, B, and C routes prioritized for bare pavement.	Anti-icing liquids; winter sand (5% salt) on compact snow roads when below -9°C.	A-Class roads cleared within 4–24 hours depending on the storm severity.
Alberta (Trans.)	Good Winter Driving: Prioritizes "ring roads," hills, curves, and bridges for anti-icing.	Sand/Salt blend (3-5% de-icer) for traction; liquid brines for pre-treatment.	6–8 hours for major highways and high-volume commuter routes.
Saskatchewan (MoH)	AADT Prioritization: Focus on inter-provincial routes (Level 1) with traffic >1,500 daily.	Mechanical plowing at 3 cm accumulation; salt/sand application for ice treatment.	6 hours for Level 1 routes; up to 24 hours for lower-volume roads.
Manitoba (MTI)	Friction Focused: Uses extensive "winter roads" (snow-packed/ice) for remote northern access.	Salt for melting on major roads; heavy use of sanding/chains on northern ice roads.	Priorities range from continuous clearing on major routes to 48 hours for rural.

Province	Core Philosophy & Priorities	De-Icing Methods & Materials	Mandated Completion (Post-Storm)
Quebec (MTMD/MTQ)	Continuous Maintenance: Minister of Transport oversees 100% of provincial highway clearing.	Heavy salt usage in the south; abrasives and cold-weather mixes used in the north.	Priority roads cleared immediately; service targets vary by region/traffic.
New Brunswick (DTI)	Temperature-Sensitive: Pavement sensors help supervisors decide salt vs. sand application.	Salt is used only above -10°C; sand is used for traction on hills/curves below that.	Major highways cleared quickly; residential rural routes follow in priority.
Nova Scotia (DPW)	100-Series Priority: Major highways (100-series) are treated to achieve bare pavement.	Brine mixture used on bridges (less corrosive); sand/salt mix near well-water areas.	8–12 hours for major highways; 24 hours for local paved and gravel roads.
Prince Edward Island	Weight-Sensitive: Protects silty subgrades from frost heaving during freeze-thaw cycles.	Salt on high-traffic routes (Trans-Canada); sand spread on others for traction.	Rotating schedule: High-traffic highways receive 24-hour service.
Newfoundland & Labrador	Daylight Focus: Operations typically run 4:30 AM to 10:00 PM; reduced service overnight.	Salt/sand application; focus on 1,317 bridges which are prone to icing.	Plowing continues until roads are open or visibility makes work unsafe.

Table 4-3. Selection of de-icing and anti-icing materials by environmental context.

Material Type	Effective Temp.	Primary Application	Environmental/Structural Consideration
Sodium Chloride (Road Salt)	Down to -10°C	General highway de-icing and brine production.	High corrosive potential; requires Salt Management Plan (SMP) tracking.

Calcium / Magnesium Chloride	Down to -25°C	Extreme cold events; used as a pre-wetting agent for salt.	Faster melting action; higher cost per ton than NaCl.
Abrasives (Sand/Chips)	All Temps	Rural/Interior routes; compact snow conditions.	Primarily for traction; requires spring clean-up to prevent drain clogging.
Corrosion Inhibitors	N/A (Additive)	Steel-bridge decks and sensitive infrastructure.	Minimizes oxidation of structural steel and rebar.

Canadian winter maintenance for highways and bridges is a high-precision operation balancing motorist safety with environmental stewardship. While all 10 provinces share a "Clean Surface" philosophy, influenced by federal aviation standards such as CAR Standard 622.11, execution varies based on regional climate and infrastructure needs.

4.2.1.1 Procedural Hierarchy and Methods

Maintenance operations follow a tiered response to ensure high-velocity corridors and critical structures remain passable.

- **Anti-Icing (Proactive):** The primary method for high-priority routes involves applying liquid brine (Direct Liquid Application) before a storm. This prevents the initial bond of ice to the pavement, which can require significantly less chemical than reactive melting.
- **Mechanical Priority:** All provinces prioritize plowing over chemical melting. Methods like tandem plowing are used on multi-lane highways to clear the full width of the road simultaneously, preventing dangerous windrows between lanes.
- **Pre-Wetting:** To mitigate "bounce and scatter," dry salt is sprayed with liquid brine as it is discharged from the spreader. This ensures the material adheres to the center of the driving lane rather than being lost to the shoulder.
- **Abrasives vs. Chemicals:** In colder regions like the Alberta and BC interior, operations rely more heavily on winter sand and crushed rock for traction on "compact snow roads" where chemical melting is ineffective due to extreme sub-zero temperatures.

4.2.1.2 Specialized Bridge Protocols

Bridges are treated as unique thermal environments because they lack geothermal insulation, leading to the "flash freeze" phenomenon.

- **Thermal Monitoring:** Departments utilize Road Weather Information Systems (RWIS)—embedded pavement sensors—to monitor real-time surface temperatures and chemical concentrations.
- **Corrosion Mitigation:** Because salt accelerates the oxidation of steel reinforcement, provinces like Nova Scotia and Ontario utilize corrosion-inhibited chemicals or non-chloride de-icers on bridge decks to preserve structural integrity.
- **Mechanical Protection:** Per Alberta Specification 01 93 51, special surfaces or bridge expansion joints require equipment fitted with rubber-tipped blades to prevent scarring or structural damage.

4.2.1.3 Environmental Restrictions and Salt Management

All 10 provinces operate under federal guidelines to minimize chloride loading in Canadian watersheds through Salt Management Plans (SMP).

- **Sensitive Zone Management:** Provinces designate Salt Vulnerable Areas (SVAs) near municipal wells or protected wetlands. In these zones, salt usage is strictly minimized or replaced with sand.
- **Snow Disposal and Stockpiling:** Snow must not be pushed into water bodies, trees, or turf areas (to prevent "chemical burn").
- **Approved Disposal:** Excess snow must be hauled to approved, lined municipal sites designed to capture and treat meltwater runoff.
- **Drainage:** Guidelines mandate that catch basins and bridge scuppers remain clear of snow cover to prevent localized flooding and refreezing.

4.2.2 Microstructural Impact on the Patina

The primary deleterious effect of chloride ions is the inhibition of the protective nanophase goethite (α-FeOOH), which constitutes the stable inner layer of a healthy patina. In environments with elevated chloride levels, the formation of akaganeite (β-FeOOH) is favored [18]. Unlike goethite, akaganeite is a porous, poorly adherent phase that readily incorporates chloride ions into its crystalline lattice. This prevents the development of a dense, impermeable barrier, thereby allowing for the sustained ingress of oxygen and moisture to the steel substrate.

Furthermore, chlorides exert a significant hygroscopic effect, attracting and retaining atmospheric moisture at relative humidity levels as low as 55%. This phenomenon substantially increases the Time of Wetness (ToW), precluding the alternate wetting and drying cycles essential for patina consolidation. Under these conditions, the steel remains in a state of chronic saturation, precluding the thermodynamic stability of protective oxides [18].

4.2.3 Mechanisms of Salt Deposition and Aggravating Site Conditions

Chlorides typically infiltrate bridge structures via two primary pathways: leaking expansion joints and traffic spray. The failure of expansion joints is considered the most critical cause of localized WS degradation, as salt laden runoff water penetrates the deck and wets the girders, bearings, and diaphragms. This moisture often migrates extensive distances along the bottom flange and ascends the web through capillary action. Additionally, high speed vehicle traffic on lower roadways generates a salt laden plume or "fog" that settles on overhead structural members. This effect is most pronounced for fascia girders facing oncoming traffic and for structures with low vertical clearance [12].

The severity of chloride impact is further exacerbated by the "tunnel effect" and "poultice corrosion." Confined spaces, such as those created by narrow depressed roadways between vertically retaining walls, trap corrosive mist and prevent air currents from dispelling the salt spray. On horizontal surfaces, such as the top of bottom flanges, chlorides frequently mix with accumulated dirt, dust, and rust flakes to form a moisture-retaining "poultice." This creates a microenvironment that facilitates continuous corrosion, mirroring the kinetics of fully immersed conditions [12].

4.3 Micro-Environmental Factors Affecting WS Bridges

The microenvironment, defined as the local, site-specific conditions experienced by a structure, often serves as a more decisive factor in weathering steel (WS) performance than the regional macroenvironment. While the macroclimatic categories established by ISO 9223 provide a baseline for material selection, a bridge’s specific geometry and surrounding geographical features can create aggressive localized conditions that fundamentally preclude the formation of a protective patina. The following sections detail the primary microenvironmental factors that dictate the durability and corrosion kinetics of weathering steel infrastructure [12].

4.3.1 The "Tunnel Effect" and Splash Zones

The most severe microenvironments are frequently encountered in grade separation structures spanning heavily trafficked roadways. A combination of low vertical clearance (typically < 6.1 m) and confining features, such as vertical retaining walls or closed abutments, or large widths creates a localized "tunnel effect." In these areas, traffic motion generates air turbulence that suspends fine, salt laden mist. This spray is trapped within the confined overhead space and settles on the structural girders. Notably, sheltered interior girders over traffic lanes do not benefit from natural rain washing; consequently, there is a continuous accumulation of chlorides and pollutants that never undergoes the rinsing necessary to stabilize the oxide layer [12].

4.3.2 Chloride Accumulation and Poultice Corrosion

On horizontal surfaces, such as the upper faces of bottom flanges and bracing connections, chlorides often mix with dirt, rust flakes, and windblown debris to form a moisture-retaining "poultice." This creates a sponge-like medium that ensures extended periods of wetness, resulting in accelerated section loss that mirrors the kinetics of full immersion. Furthermore, girders located in close proximity to adjacent structures may be subjected to direct snow and salt spray from snowplows on neighbouring decks, further escalating the chloride load beyond macroenvironmental predictions [12].

4.3.3 Humidity and Time of Wetness (ToW)

Extended periods of moisture prevent the requisite wet/dry cycles necessary for the consolidation of the protective patina. Low vertical clearance over stagnant or moving water (< 3 m) can cause a localized increase in humidity, maintaining a high ToW. Similarly, dense vegetation in close proximity with the steel or site features that block sunlight for more than six hours per day impede air circulation and surface drying. Transpiration can also impact humidity. Surface orientation also plays a critical role; groundward-facing (bottom) surfaces typically remain saturated longer than skyward surfaces because they are shielded from the evaporative effects of solar radiation [12].

4.3.4 Design and Detailing Factors

Structural detailing can inadvertently exacerbate adverse microenvironments. Failed expansion joints are the most prevalent cause of localized failure, as they allow salt laden runoff to saturate girder ends and bearings directly. Once moisture ponds on a bottom flange, it can be drawn several inches up the web via capillary wicking, transporting dissolved salts into otherwise dry regions of the structure. Additionally, insufficient deck overhangs allow windblown rain to frequently wet fascia girders that would otherwise remain protected, leading to nonuniform patina development and localized thinning [12]. Small details such as the lack of drip groves on the soffit of slabs or on the bottom of flat steel plate elements may allow salt laden water to travel long distances by capillary action. Drainage systems, and in particular inadequate detailing of down spouts may allow deck drainage water to be spayed back onto the lower steel elements.

4.4 Corrosion Allowance and Design Life Adjustments

The application of a corrosion allowance is a critical design adjustment intended to ensure that weathering steel (WS) members maintain their structural integrity throughout their intended service life, despite the gradual loss of metal to the environment. These sacrificial thicknesses

are typically calibrated for design lives ranging from 75 to 120 years and are adjusted based on the predicted corrosivity of the site and the specific metallurgical properties of the steel grade employed [12].

4.4.1 Standard Corrosion Allowances

In the United States, guidelines for corrosion allowances focus on compensating for steady state metal loss in environments where a protective patina is expected to form successfully. For a standard 100-year service life, it is recommended that the thickness of weathering steel members less than 38 mm (1.5 in.) be increased by 0.8 mm (32 mils) per exposed surface. For heavier sections equal to or exceeding 38 mm in thickness, standard production tolerances are generally considered sufficient to compensate for anticipated losses, and no additional sacrificial thickness is required [12].

However, in high corrosivity environments where performance is uncertain or categorized as ISO 9223 C4, a total sacrificial thickness of 1.6 mm (1/16 in.) is recommended for horizontally oriented plates. This specific allowance accounts for the cumulative section loss occurring on both the top and bottom surfaces of the plate over the life of the structure.

International standards utilize the ISO 9223 corrosivity categories to define more graduated corrosion allowances for 100-year or 120-year design lives. As summarized in **Table 4-4**, the permissible use of unpainted weathering steel and the required sacrificial buffer vary significantly by jurisdiction [12]. It is interesting to note that Australia bans the use of weathering steel in C4 environments.

Table 4-4. International corrosion allowances (mm) for 100–120-year design life [7]

Region / Guideline	C1/C2 (Low)	C3 (Medium)	C4 (High)	C5 (Very High)
ECCS (Europe)	0.8 mm	1.0 mm	1.5 mm	Not Allowed
UK (CD 361)	0.5–1.0 mm	1.0–2.0 mm	1.5–3.0 mm	Not Allowed
Australia (AS 5100.6)	1.0 mm	1.5 mm	Not Allowed	Not Allowed

For specialized geometries such as the internal surfaces of ventilated box girders, reduced corrosion allowances (e.g., ~0.5 mm) may be applied where drainage and ventilation are provided to limit moisture accumulation. In practice, even nominally closed or sealed bridge

components are not considered fully moisture-free, as condensation or leakage can occur over service life; therefore, durability design typically relies on drainage detailing, venting, and inspection access rather than assuming complete exclusion of electrolyte formation.

4.4.2 Material Specific Adjustments

The selection of steel grade can fundamentally alter the necessity for a corrosion allowance. Conventional WS design adjustments assume a steady state corrosion rate not exceeding 7.5 µm/year. If site specific environmental factors, such as high chloride deposition or persistent wetness, cause rates to exceed this threshold, the use of unpainted weathering steel is generally discouraged regardless of the allowance provided [7].

In contrast, high performance alloys such as ASTM A1010 form a tenacious chromium oxide film rather than a traditional iron oxide patina. The superior corrosion resistance of this grade often allows for the complete elimination of a corrosion allowance, enabling engineers to design significantly thinner and lighter structural members, with thicknesses as low as 4 mm [12].

4.4.3 Design Limitations and Detailing

It is imperative to recognize that corrosion allowances serve as a buffer for uniform atmospheric corrosion and cannot compensate for the rapid, localized deterioration caused by poor hydraulic design, poor detailing or neglected maintenance. Sacrificial thickness is not a viable substitute for proper drainage or joint integrity. For instance, leaking expansion joints can induce localized corrosion rates in gaps between web and hanger plates as high as 400 µm/year. Such extreme rates would consume even the most generous corrosion allowance within a few years of service [12].

Furthermore, metal loss is consistently more severe on horizontal surfaces where water, salt, and debris accumulate. Consequently, contemporary design philosophies increasingly recommend applying the corrosion allowance primarily to bottom flanges and other horizontal components to target the areas of highest vulnerability [12].

4.5 Integrated Maintenance and Assessment Strategy

The maintenance and assessment of weathering steel (WS) bridges are critical for ensuring long-term structural integrity. Effective management requires a combination of qualitative visual inspections, quantitative physical testing, and proactive preservation strategies to minimize the Time of Wetness (ToW) and eliminate corrosive contaminants, particularly chlorides.

4.5.1 Corrosion Assessment Methodologies

Determining whether a patina is in a stable, protective state or undergoing active, deleterious corrosion requires a multi-faceted approach. Systematic data collection is essential to confirm that the protective patina is developing as intended and to identify localized corrosion before significant section loss occurs.

Inspection and Monitoring Frequencies: Lifecycle management requires a tiered approach. Routine visual inspections should be performed in accordance DOT guidelines. These are supplemented by Level 2 detailed condition assessments typically every three to six years.

Quantitative Performance Tracking: Ultrasonic thickness and corrosion rate monitoring should be conducted every six years in ISO 9223 C3 (medium) environments and every 12 years in ISO 9223 C2 (low) environments. Because corrosion rates are initially elevated, at least 20 years of longitudinal data is required to confirm whether the patina has reached a steady-state equilibrium.

Documentation Standards: Documentation should include accurate as-built drawings and initial plate thickness records. In accordance with OSIM (Ontario Structure Inspection Manual) requirements, bridge inventory and inspection data should be systematically recorded to support condition assessment and deterioration tracking. These data may be integrated into bridge management systems (BMS), which provide a structured platform for lifecycle management, and can be further linked to GIS-based databases where applicable. Condition information may be represented using standardized OSIM inspection ratings and/or quantitative deterioration indicators to support consistent asset management and decision-making.

Routine Maintenance and Preservation Procedures The highest priority in WS maintenance is the management of deck joints, scuppers, and environmental debris to prevent the formation of "poultice" layers that facilitate continuous corrosion. It is worth mentioning that leaking drains (scuppers), downspouts or leaking longitudinal carrier pipes may cause comparable chloride-related issues.

Drainage and Joint Upkeep: Maintaining the integrity of deck joints is the most critical task. Leaking expansion joints allow salt-laden runoff to saturate girder ends and bearings, representing the most common cause of localized failure.

Debris and Vegetation Control: Loose debris, windblown dust, and biological matter (e.g., bird nests) must be removed using compressed air or vacuums. Additionally, vegetation within 3 meters of the steel must be cleared to improve air circulation and sunlight access, ensuring the patina can dry and stabilize effectively.

Preservation Washing: Preservation washing can be categorized based on cleaning intensity and operational objective. High-volume power washing (~380 L/min) is primarily used for chloride removal and bulk decontamination. Pressure washing (~13 L/min at ~1,750 psi) is suitable for flushing, sweeping, and removal of light soil and debris. High-pressure washing

(~19 L/min at ≥5,000 psi) is used for the removal of non-adherent corrosion products and tightly bound surface deposits. For maintenance of exposed steel surfaces, particularly weathering steel in chloride-prone environments, periodic washing is recommended to limit chloride accumulation. Washing is most effective when performed in early spring to remove winter deposited salts before significant migration into the corrosion product layer. Nozzle selection (e.g., 0°–15°) should be adjusted to achieve the required mechanical cleaning intensity. For structures exposed to heavily salted highways (e.g., grade separations), washing at intervals of 1–2 years may be required depending on exposure severity.

4.5.2 Remedial and Rehabilitation Actions

If an assessment identifies significant deterioration or a non-stabilizing patina, more assertive remedial measures must be implemented [12]:

Targeted Painting: This involves painting the steel girder ends, typically for a distance of 1.5 times the girder depth directly beneath expansion joints, to mitigate damage from future leaks. In some applications, coating systems with semi-permeable or moisture-managing characteristics such as Cupten-Coat Aqua have been considered, these systems are designed to reduce chloride ingress while allowing limited moisture transmission, thereby managing corrosion risk in areas subject to intermittent wetting and leakage.

Crevice Sealing: Non-performing crevices in bolted joints can be rehabilitated by disassembling and coating the faying surfaces, or by applying penetrating sealers and caulking to prevent moisture ingress.

Joint Reduction/Elimination: The most effective long-term preservation strategy is reducing or eliminating deck joints through the use of link slabs or by converting the structure to jointless, integral, or semi-integral abutment designs, thereby reducing direct pathways for chloride infiltration. In semi-integral systems, the deck–abutment interface is displaced below the deck level rather than fully eliminated; however, a concealed movement joint remains and any leakage is typically redirected toward the abutment backwall and embankment drainage zone.

4.6 Overview of Testing and Evaluation

The testing and evaluation of weathering steel (WS) and its protective patina involve a complex approach, ranging from accelerated laboratory simulations to in-situ qualitative and quantitative field assessments. These methodologies are designed to predict long-term performance, characterize the chemical composition of the rust layer, and monitor the structural integrity of the steel over its multi-decadal service life.

4.7 Corrosion Rate Calculation

The standard method for calculating average thickness loss is through mass loss measurement in accordance with ASTM G1-03. This procedure involves chemically stripping

the rust from exposed coupons using a specific inhibited acid solution and utilizing the weight difference to determine the average penetration per side. This remains the benchmark for validating the steady state corrosion rates assumed during the design phase.

The standardized measurement of corrosion loss and surface contaminants is achieved through a synthesis of gravimetric analysis, physical thickness monitoring, and specialized chemical extraction techniques. These methodologies are governed by international standards (ISO and ASTM) to ensure data consistency across diverse geographical environments and varying metallurgical grades.

Corrosion loss is typically expressed as average thickness loss per surface or as total corrosion penetration. These metrics are determined through several complementary methodologies, including:

Mass Loss Method (Gravimetric Analysis): This serves as the primary benchmark for calculating corrosion rates. Following ASTM G1-03, rust is chemically stripped from exposed steel coupons using specific cleaning designations, such as solution C.3.5. The average thickness loss is calculated from the weight difference, accounting for the surface area and the density of the steel (typically 7.85-7.86 g/cm³).

Ultrasonic Thickness Measurement: Portable ultrasonic gauges facilitate the in-situ monitoring of residual steel thickness. To obtain accurate "peak-to-valley" readings on weathered surfaces, the oxide layer must be partially ground away. This ensures the probe contacts the base metal peaks, while any localized depressions remain filled with oxide, preventing artificial inflation of the thickness measurement.

Electromagnetic Induction: Utilized primarily to measure non-magnetic film thickness on ferrous substrates, this method is performed according to ISO 19840 for the rough surface profiles characteristic of weathering steel.

4.8 Laboratory and Accelerated Testing Methods

The ability of laboratory-based methodologies to accurately predict the long-term atmospheric corrosion of weathering steel (WS) alloys remains a subject of significant scrutiny. Discrepancies frequently emerge between accelerated tests and real-world field performance, as laboratory setups often struggle to replicate the complex environmental variables encountered over decades of service.

4.8.1 Effectiveness of Cyclic Corrosion Testing (CCT)

Accelerated cyclic corrosion tests aim to compress decades of exposure by subjecting steel to repeated wetting and drying phases. However, the predictive validity of these protocols is highly dependent on the chemical composition of the electrolyte. In a recent study, the performance of two known CCTs were compared to the field test result. The study was conducted on seven different weathering steels, four of them were custom made (A1 to A4)

and three industrial alloys (A5 to A7). The chemical composition of the alloys is presented in **Table 4-5.** For the field test, all seven plates were exposed to natural atmospheric corrosion and mounted onto a bridge at the Hwy 404 and Bloomington Road overpass, Greater Toronto Area, Ontario (**Figure 4-2**), in August 2012 and removed after 10 years of exposure [13]. The exposed environment is defined by the heavy application of de-icing salts, a sag curve, and a 'tunnel effect' from the closed bridge abutments, combined with high traffic volumes at this bridge, where the existing ACR (Atmospheric Corrosion-Resistant) girders had not performed adequately. All seven plates were also subjected to two different CCT tests in Surface Science Western laboratory to determine the effectiveness of CCTs. The following results were obtained.

Table 4-5. Chemical composition of the examined weathering steels [13].

Element	**Steel Sample Code**						
	A1 (+Mo/P)	**A2 (+Ni/Mo)**	**A3 (+Nb/B)**	**A4 (+Ni/Cr/Mo)**	**A5 (ASTM A1010)**	**A6 (ASTM A709 HPS 70W)**	**A7 (3.5% Ni)**
C	0.05	0.05	0.05	0.05	0.03 max	0.11 max	0.17 max
Mn	1.37	1.37	1.37	1.37	1.37	1.5 max	1.1-1.3
S	0.007 max	0.007 max	0.007 max	0.007 max	0.01 max	0.006 max	0.025 max
P	0.025	0.025 max	0.025 max	0.025 max	0.04 max	0.02 max	0.025 max
Si	0.42	0.42	0.5	0.42	1.0 max	0.3-0.5	0.13-0.45
Cr	0.55	0.5	0	0.75	10.5-12.5 max	0.45-0.7	-
Ni	0.3	0.7	0.3	1.25	1.5 max	0.4 max	3.18-3.82
Cu	0.3	0.3	0.35	0.3	-	0.25-0.4	-
Mo	0.4	0.4	0.3	0.5	-	0.02-0.04	-
Al	0.027	0.027	0.027	0.027	-	0.01-0.044	-
Nb	0	0	0.03	0	-	-	-
V	0.07	0	0	0	-	0.04-0.08	-
B	-	-	0.0028	-	-	-	-
Ti	-	-	0.04	-	-	-	-
Ca	Treated	Treated	Treated	Treated	-	-	-

Figure 4-2. Steel plate samples installed under the Hwy 404 and Bloomington Road overpass [13].

Modified GM 9540P (now GMW14872): This protocol exhibits the strongest alignment with 10-year field performance due to its inclusion of bicarbonate anions and specific chloride concentrations (**Figure 4-3**). These elements more accurately simulate the aggressive, salt-laden micro-climates and industrial pollutants found in bridge environments.

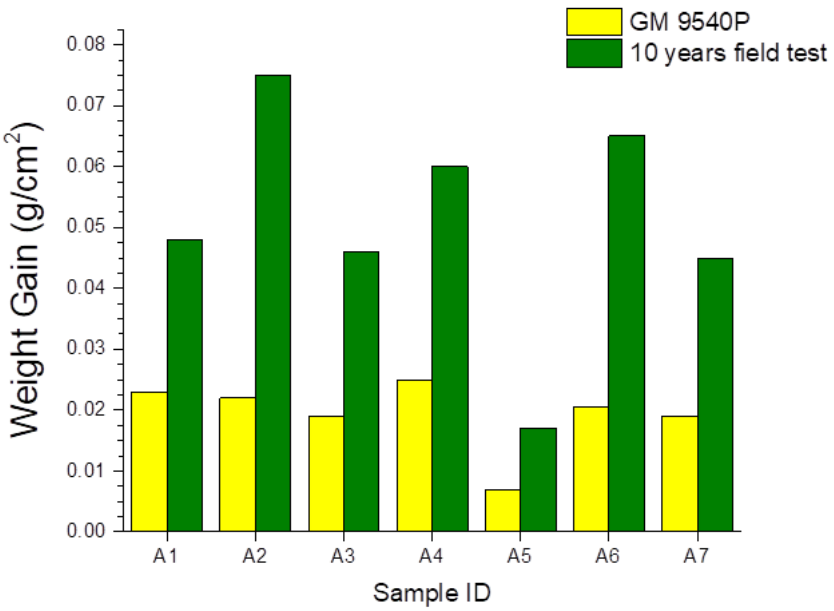

Figure 4-3. A comparison of the weight gain in the modified GM 9540P laboratory setting with the field test data.

ASTM G85-A5 (Prohesion): While a standard in the industry, this method frequently deviates from field results (**Figure 4-4**). Evidence suggests weight gains in Prohesion tests can be significantly higher than those observed in situ, potentially leading to an overestimation of an alloy's corrosion susceptibility.

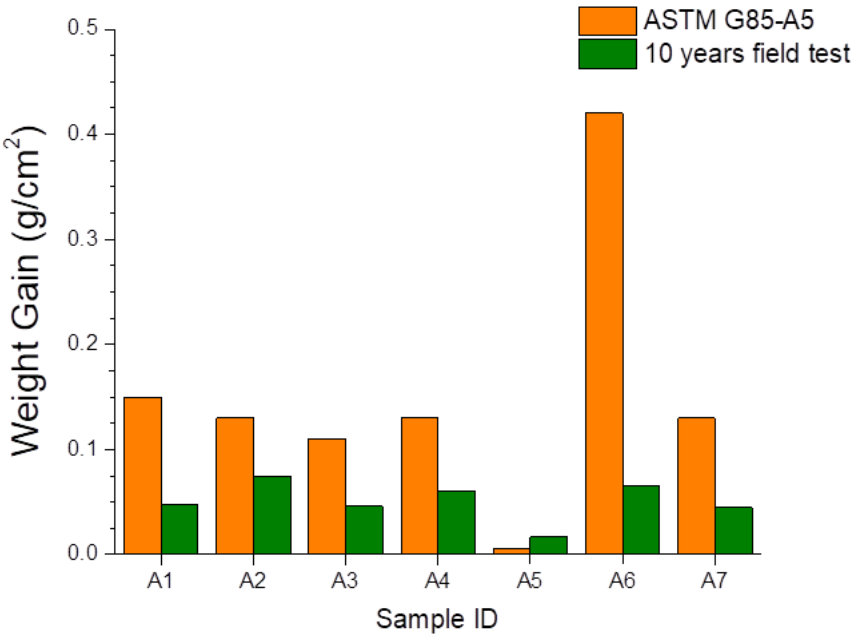

Figure 4-4. A comparison of the weight gain in the laboratory setting with the field test data.

4.8.2 Limitations of Linear Polarization Resistance Electrochemical Measurement

The comparison of laboratory electrochemical test results and the field test on the seven examined alloys indicates that Linear Polarization Resistance (LPR) measurement fail to predict long-term atmospheric durability (**Figure 4-5**). Sample A5 displayed a continuous increase in polarization resistance (R_p) after an initial decrease and rebound. For other alloys, the R_p value eventually reached a steady state, indicating the formation of a protective patina. This increase in R_p suggests a gradual modification of the patina's microstructure, which likely reduces active corrosion sites. This phenomenon indicates that the patina acts as an effective barrier to both anodic and cathodic reactions, thereby increasing polarization resistance. Previous field studies confirm that once a patina forms, corrosion is primarily controlled by the transport of species through this oxide layer.

After an initial 8-hour period, Sample A6 exhibited a stable R_p. However, a significant discrepancy was observed between these electrochemical measurements and the results from

field and cyclic corrosion tests. In LPR testing, Sample A6 emerged as the most corrosion-resistant weathering steel (A5 belongs to ASTM A1010 as a high-chromium alloy), while Sample A3 was the least. This sharply contrasts with field and cyclic data, where A3 consistently demonstrated superior resistance and A6 was among the least resistant. This deviation is particularly remarkable as the electrolyte used for electrochemical testing was identical to that employed in the GM 9540P cyclic test.

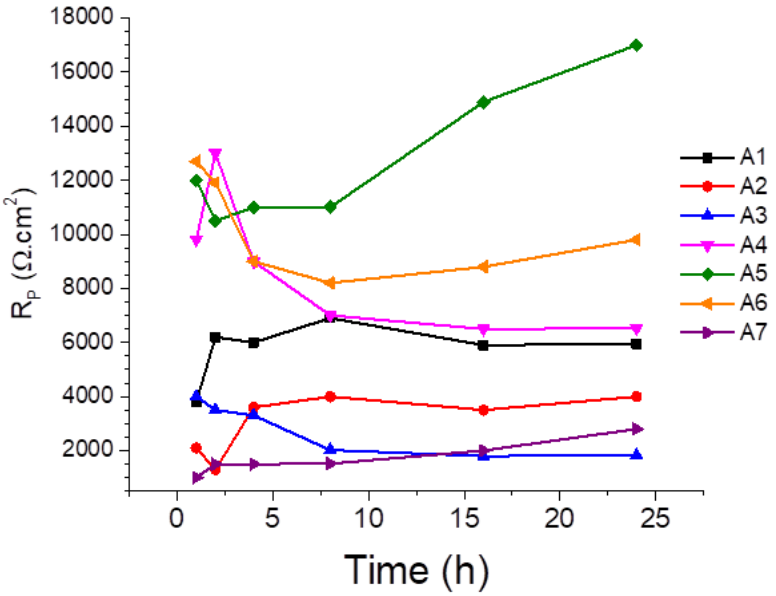

Figure 4-5. LPR measurements conducted on the weathering steel alloys.

The main reasons for the failure of this specific electrochemical testing method, which normally is conducted in large solution volumes, are most likely the different corrosion mechanisms as described in detail in Section 3, and summarized as follows:

Volume Discrepancy: This LPR electrochemical testing method utilizes a large volume of electrolyte, allowing for unhindered ion mobility. This is fundamentally unrepresentative of atmospheric corrosion, where the electrolyte is restricted to transient micro-droplets.

Absence of Drying Phases: A critical characteristic of this electrochemical method is the lack of a drying stage. In field applications, the drying phase is essential for the precipitation of stable iron oxyhydroxides that form the protective patina.

Buffering Effects: Bulk-solution setups buffer local pH fluctuations, whereas in actual field conditions, pH changes within small droplets drive the formation of either protective or non-protective oxides.

While the Modified GM 9540P test offers a promising accelerated assessment for bridge applications, the engineering of a high-fidelity electrochemical protocol to more precisely simulate in-situ wetting and drying kinetics is proposed as a vital direction for future work.

Ultimately, a holistic approach that synthesizes these accelerated laboratory cycles with long-term field data remains essential for ensuring the structural reliability and durability of weathering steel in critical infrastructure. The lack of correlation is often driven by fundamental differences in the physical and chemical mechanisms occurring in each environment:

Oxide Composition Mismatch: Standard laboratory protocols, typically utilize a high Time of Wetness (ToW). This promotes the formation of maghemite (γ-Fe_2O_3), a phase common in laboratory corroded samples but notably absent in actual bridge field environments, particularly those exposed to de-icing salts.

Divergent Failure Modes: Accelerated tests like the neutral salt spray and continuous immersion often induce failure through blistering. This failure mode is rarely observed in actual exterior bridge exposures, where degradation is more commonly characterized by localized pitting or laminar exfoliation.

Chloride Sensitivity Thresholds: Laboratory models for inorganic zinc systems suggest a high sensitivity to low chloride levels (e.g., 7 mg/cm^2). However, empirical field data support a significantly higher sensitivity threshold, typically ranging from 30 to 50 mg/cm^2, indicating that laboratory environments may overstate the aggressiveness of low-salinity conditions.

4.8.3 On-Site Prediction

A primary finding of the 10-year field exposure of seven weathering steels in a Canadian bridge evaluation is the strong correlation between patina thickness and weight gain, establishing thickness as a reliable in-situ proxy for corrosion rates (**Figure 4-6).**

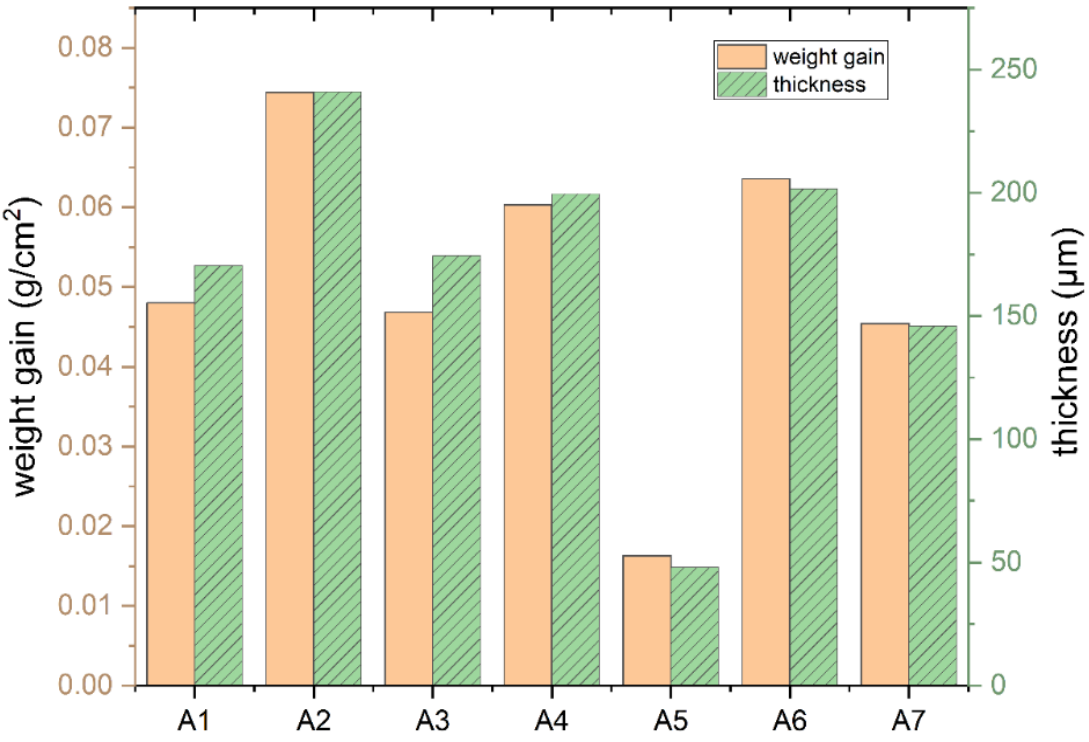

Figure 4-6. Correlation between the weight gain and oxide thickness of the formed patina layer on the surface of the examined weathering steels.

The study used portable gauges to allow inspectors to measure the non-magnetic patina layer over the ferrous substrate with high precision. This non-destructive approach is rapid and cost-effective, making it ideal for routine asset management. In addition, the study established a weight gain factor of approximately 3.04 g/cm³. This coefficient allows for the conversion of measured thickness into an estimate of cumulative corrosion, accounting for the porous, granular nature of the surface oxide and the presence of chloride contaminants.

By applying this weight gain factor to in-situ thickness measurements, bridge owners can quantitatively estimate the accumulation of oxides and hydroxides. This methodology provides an empirical indicator of the overall corrosion resistance of weathering steel in critical infrastructure, allowing for more informed maintenance and lifecycle interventions.

4.9 Surface Characterization and Spectroscopy

Advanced analytical tools are utilized to investigate the nanostructure and chemical phases of the protective patina, as the ratio of these phases dictates the material's durability.

4.9.1 Raman Spectroscopy

This vibrational technique is particularly effective for identifying amorphous and nanocrystal structures of metal hydroxides and oxides, such as ferrihydrite, which are often undetectable by standard X-ray diffraction (37).

4.9.2 X-Ray Diffraction (XRD)

Standard XRD remains the preferred method for identifying and quantifying major crystalline phases, including goethite (α-FeOOH), lepidocrocite (γ-FeOOH), and the deleterious akaganeite (β-FeOOH) (37). The XRD patterns obtained on steel plates A1 to A7 (case study) are shown in **Figure 4-7**. The peaks were assigned to three main phases: G for Goethite (α-FeOOH), A for Akaganeite (chloride-containing β-FeOOH), and L for Lepidocrocite (γ-FeOOH). The presence of Magnetite and Hematite was not possible to determine visually due to heavy peak overlapping; however, taking into account that they are often present in mature corrosion products, we used all five of them in the XRD pattern fitting in the quantitative analysis [1].

Quantitative analysis was also performed with full pattern fitting using identified corrosion products. Taking into account the different chemical compositions of tested samples, the patina of each alloy can have slightly different crystalline structures due to the possible incorporation of metal ions other than Fe. Cell parameters, preferred orientation of crystals, and crystallite size were refined for each pattern. Additionally, the structure of akageneite was further refined. Because Akaganeite contains Cl^- anions in a tunnel space of crystalline cells that can be exchanged with other anions, resulting in variation of its composition, Hydroxyl anion (OH^-) would be the most expected anion to exchange with Cl^- during atmospheric exposure. Therefore, the Akaganeite structure was refined to contain a variable amount of Cl^- to allow for the variations in different samples. The results of quantitative analysis are presented in **Table 4-6.**

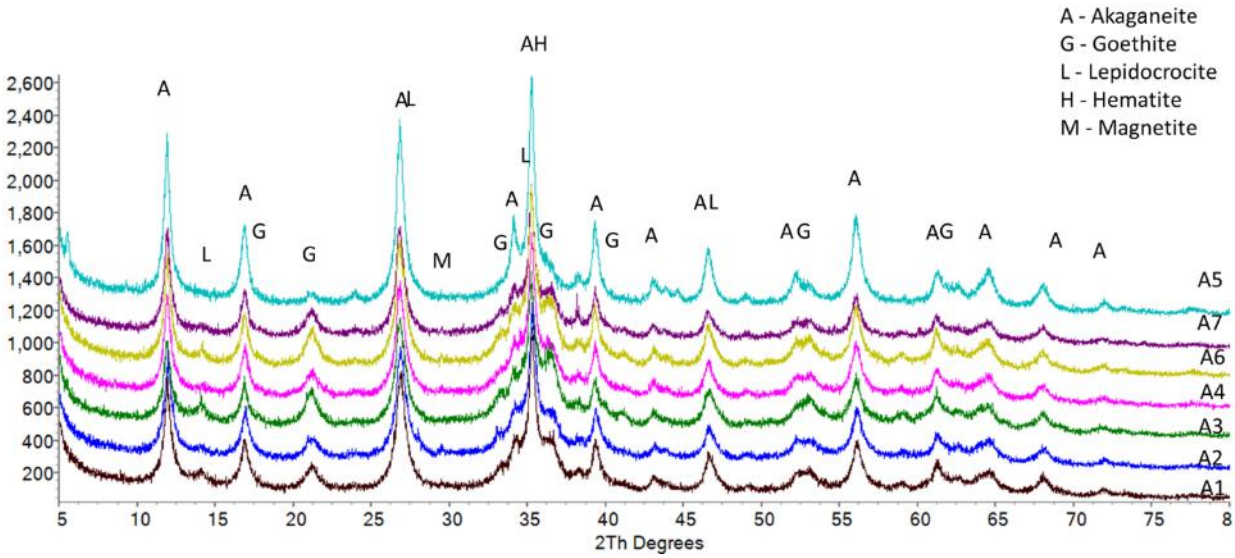

Figure 4-7. XRD patterns of corrosion products of tested steel specimens.

Table 4-6. Composition of rust products of tested weathering steels.

Sample	Akaganeite [%]	Goethite [%]	Lepidocrocite [%]	Magnetite [%]	Hematite [%]	α/γ (1)	α/γ* (2)	(β+s)/γ* (3)
A1	55.3	26.3	14.4	0.4	3.6	1.83	0.37	0.79
A2	56.6	26.5	12.1	0.5	4.4	2.19	0.38	0.83
A3	44.3	37.6	14.7	0.5	3.0	2.56	0.63	0.75
A4	59.7	24.8	11.7	0.3	3.5	2.13	0.35	0.84
A5	70.1	17.2	6.6	0.3	5.8	2.61	0.22	0.91
A6	55.4	27.7	14.8	0.4	1.7	1.87	0.39	0.79
A7	58.2	26.7	11.2	0.5	3.4	2.39	0.38	0.84

(1) α/γ is the mass ratio of goethite and lepidocrocite; **(2) α/γ*** is the mass ratio goethite and sum of lepidocrocite, akageneite and magnetite; **(3) (β+s)/γ*** is the mass ratio of sum of lepidocrocite and magnetite and sum of lepidocrocite, akageneite and magnetite.

4.9.3 Mössbauer Spectroscopy

This technique is considered an indispensable tool for identifying and quantifying nano phasic iron oxides that are "transparent" to other spectroscopic methods. It is uniquely capable of differentiating between stable goethite and less protective phases (37).

4.9.4 Scanning Electron Microscopy – Energy Dispersive Spectroscopy

Scanning Electron Microscopy – Energy Dispersive Spectroscopy (SEM-EDS) provide high resolution imagery of rust morphology and elemental distribution maps (e.g., Cr, Ni, Cu, P)

through the depth of the rust layer, allowing for the observation of the enrichment of alloying elements at the metal/rust interface. **Figure 4-8** shows SEM images of the examined steel surfaces at an original magnification of 1000x, providing details of the patina and its oxide features at the micro-scale. The results from **Figure 4-8** depict a granular morphology in the oxides on all observed surfaces, featuring pores and boundaries between grains. These microscopic features may serve as pathways for electrolytes to access the metallic surface, facilitating the formation of new oxides. A recurring observation was the presence of surface charging localized specifically on the oxide regions, as both the oxides and the EDS-detected salt deposits are highly insulating. This result is entirely consistent with the de-icing conditions experienced over the 10-year exposure period.

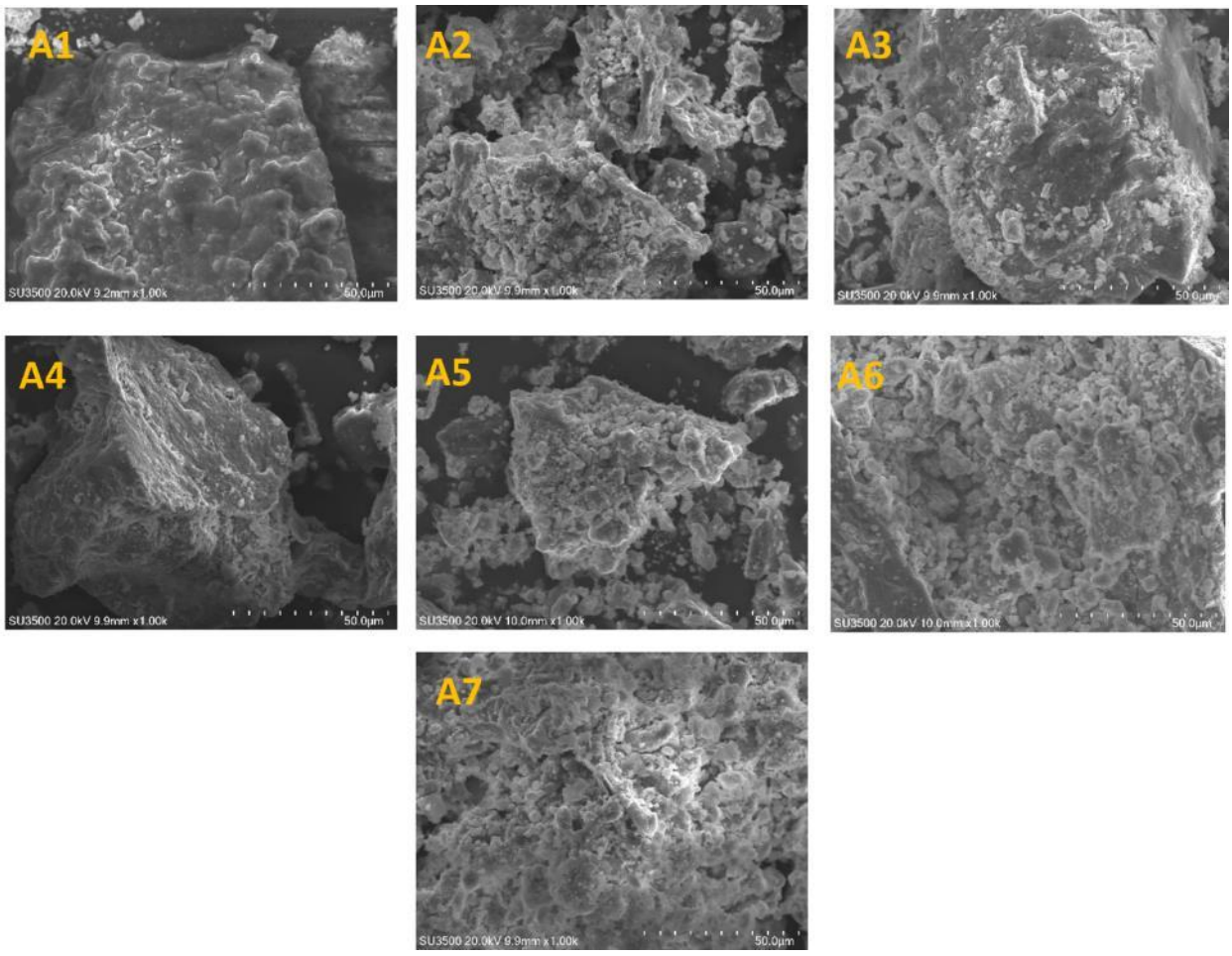

Figure 4-8. SEM analysis of the patina layer formed on the steel surfaces shows granular oxide films with pores. Note the charging effect observed in all samples.

Table 4-7 presents how the EDS results can help identify the corrosion mechanism and patina formation. It revealed iron (Fe) and oxygen (O) as the primary elements on the surface, aligning with expectations of the formation of iron oxides/hydroxides on the surface. The chromium signal in the case of A5 is related to the nature of the A5 sample as it is a stainless

steel and contains high chromium content. The Si, Ca, and Na signals most likely originated from dust and sand. One important observation for all examined surfaces was the presence, in all examined patina layers, of Cl arising from the de-icing process during winter. As mentioned before, chloride ions play a crucial role in shaping the composition of surface oxides (2,16).

Table 4-7. The EDS analysis of the patina layer formed on the steel surfaces shows iron and oxygen as the main elements, which confirms the formation of iron oxides/hydroxides on the surface.

Element	A1	A2	A3	A4	A5	A6	A7
Fe (Iron)	44.12	52.50	42.67	45.43	60.62	59.17	87.26
O (Oxygen)	51.35	39.97	55.26	51.05	31.67	36.99	6.55
Cl (Chlorine)	2.66	1.41	1.103	0.92	1.55	1.65	0.14
S (Sulfur)	0.96	0.26	0.35	0.23	0.22	0.20	-
Mn (Manganese)	0.72	1.23	0.63	0.72	0.80	1.00	0.87
Al (Aluminum)	0.18	0.50	-	-	-	-	0.36
Ca (Calcium)	-	1.46	-	0.14	0.26	0.65	4.43
Si (Silicon)	-	0.87	-	0.17	0.46	0.33	0.40
Na (Sodium)	-	1.81	-	1.24	1.61	-	-
Cr (Chromium)	-	-	-	-	1.90	-	-

4.10 Patina Quality Assessment (Qualitative and Quantitative)

The assessment of the protective patina on weathering steel (WS) is essential to verify its performance as a functional barrier against atmospheric degradation. This evaluation relies on a combination of qualitative observations and quantitative physical diagnostics.

4.10.1 Qualitative Patina Assessment

Visual inspection remains the primary tool for preliminary evaluation and is most effective when conducted at close range (within 1 meter). Inspectors utilize specific morphological cues to determine the state of the oxide layer.

Color Progression: A stable patina typically transitions through a predictable color sequence, moving from an initial yellow, orange to light brown, and eventually to a dark chocolate brown or purple, brown. Conversely, black or dull gray tones are often indicative of non-protective oxides formed under conditions of excessive moisture or high salinity (7).

Surface Texture and Flake Size: A healthy patina is fine grained and smooth. Standard engineering guidelines utilize rust flake size as a primary metric for performance classification:

Excellent/Protective: Tightly adherent; particles are generally less than 3 mm (1/8 in.) (4).

Poor/Non-Protective: Characterized by large, loose flakes exceeding 12 mm (1/2 in.) or the presence of laminar sheets (slab rust) and nodules (4).

Adherence Testing: Because visual cues can occasionally be deceptive, adherence must be verified physically. This is typically achieved by tapping the surface with a hammer or prying with a putty knife; a protective layer will resist removal, whereas a failing patina will shed significant rust particles upon light contact (5).

4.10.2 Quantitative Physical Assessment

Quantitative methods provide objective data to support visual findings, particularly when patina performance is borderline or environmental conditions are aggressive.

Tape Adhesion Test: Standardized under ASTM D3359, this method involves pressing clear tape onto the surface and peeling it off to analyze the size and spatial density of captured rust particles. This provides a permanent, comparative record for longitudinal monitoring across inspection cycles (13).

Ultrasonic Thickness Measurement: This technique determines the "peak-to-valley" thickness to assess remaining structural capacity. For accurate readings, the oxide must be partially ground away so the probe makes contact with the base metal peaks, preventing the measurement of the oxide layer itself (13).

Chloride Contamination Testing: Field kits, such as Chlor*Test, extract surface salts to measure chloride concentration. However, these tests often exhibit low extraction efficiency (typically <10%) because chlorides are frequently sequestered deep within the porous rust matrix, making them more suitable for identifying risk than for precise service life predictions (13).

4.10.3 Microstructural and Scientific Indices

In laboratory settings, advanced analytical tools are employed to characterize the chemical phases of the patina, providing a definitive measure of its thermodynamic stability.

Protective Ability Index (PAI): This index utilizes the mass ratio of goethite (α-FeOOH) to lepidocrocite (γ-FeOOH). A ratio of $\alpha/\gamma > 2$ is generally considered the threshold for a stabilized, protective layer (30).

Modified Indices for Saline Environments: In chloride rich regions, a more complex ratio (α/γ^*) is employed. This calculation accounts for the presence of akaganeite (β-FeOOH), a non-protective, crystalline phase that readily harbors chloride ions and facilitates continued corrosion ingress (30). A ratio below 1 indicates that the patina is active and poorly protective. A value above 1 indicates a stable, dense, and protective patina has formed. A mature, highly protective patina often has an α/γ^* value ranging from 1.0 to 3.0 (or even higher on very old structures).

4.11 Micro-Corrosion Analysis and Sensor Integration

To accurately evaluate the performance of weathering steel (WS) in the Canadian climate, it is insufficient to treat a bridge as a single environmental unit. Traditional evaluation often fails because it ignores micro-corrosion, the localized electrochemical degradation that occurs due to varying micro-climates across different structural components.

Weathering steel's ability to form a protective patina (predominantly α-FeOOH) is highly sensitive to local conditions, and as mentioned before in Section 4.3, the microenvironment affects corrosion performance significantly. Therefore, studying corrosion by section is highly recommended. The integration of sensors into the testing protocol is a proxy to provide data:

Real-Time Corrosion Rate Monitoring: Using the electrochemical testing parameters, the sensors allow engineers to see instantaneous corrosion spikes. This is critical for evaluating how a bridge reacts to specific winter salt-application events in real-time.

Validating Time of Wetness (ToW): Sensors measure the exact duration of time that the steel surface remains damp. If a sensor reveals a ToW exceeding limits defined in ISO 9223, it provides an early warning that the patina will never stabilize, allowing for intervention decades before a structural deficiency arises.

Mapping "Hot Spots": Deploying a sensor network across a "representative span" (e.g., placing sensors at the pier, mid-span, and fascia) creates a high-resolution map of environmental aggressiveness. This data can be used to calibrate the Corrosion Allowance used in future Canadian bridge designs.

Objective Lifecycle Documentation: Sensors remove the subjectivity of human inspectors. The digital output (measured in μm/year) provides an immutable record for the Bridge Management System (BMS), ensuring that maintenance budgets are allocated based on measured risk rather than visual estimates.

5 In-Service Bridge Monitoring

5.1 Sensor-Based Characterization of Macro-Environmental Conditions

5.1.1 Temperature/Relative Humidity Probe

Ambient air temperature and relative humidity (RH) within the macro-environment are continuously monitored utilizing a Campbell Scientific CS215-L digital probe (**Figure 6-1**). Data transmission from the probe to the central acquisition system is executed via the SDI-12 communications protocol, ensuring robust digital signal integrity and minimizing signal degradation across the extended cable routing of the bridge monitoring network.

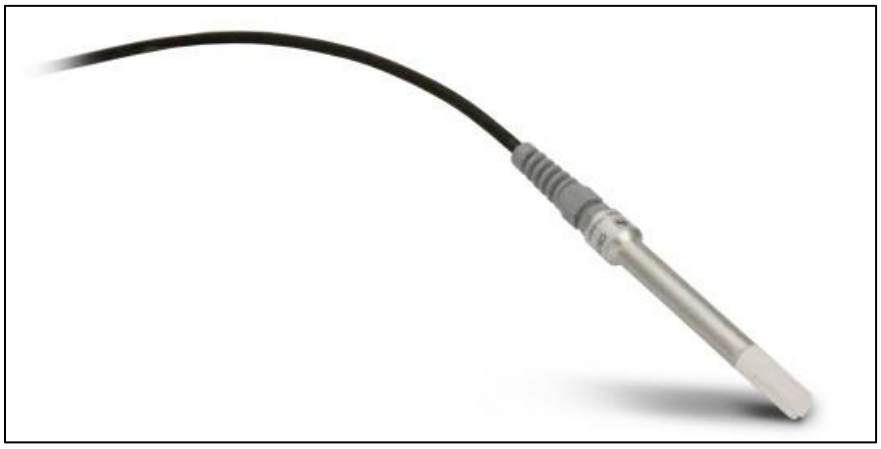

Figure 5-1. Campbell Scientific CS215-L digital probe utilized for continuous monitoring of ambient temperature and relative humidity.

Unlike the ambient temperature and relative humidity (T/RH) probe, which captures macro-environmental conditions that remain relatively uniform across the entire structure and thus only requires a single deployment, the highly localized nature of corrosion necessitates a distributed monitoring approach. To properly understand the complex material degradation mechanisms at play, integrated plates composed of multiple specialized sensors, such as galvanic assemblies, thickness loss, and time of wetness (ToW) sensors, have been installed at various strategic locations across the bridge. This spatial distribution is critical because localized structural micro-climates, driven by factors such as proximity to vehicular splash zones, sheltering from direct precipitation, and exposure to concentrated chloride runoff, create drastically different corrosion environments that cannot be accurately captured or extrapolated from a single centralized measurement. The characterization of these localized micro-environments and the deployment of their associated sensor arrays are the primary focus of Section 5.2.

5.2 Quantifying Spatial Variability in Micro-Environmental Corrosivity

To comprehensively evaluate the localized environmental conditions and corresponding material degradation mechanisms, a customized array of sensors and physical specimens, shown in **Figure 6-2**, was deployed at each designated monitoring location across the bridge structure. The sensing network includes a series of galvanic specimens (A–D), each prepared with distinct material combinations to specifically quantify dissimilar metal interactions and evaluate local galvanic driving forces. Beyond measuring absolute currents, these specimens serve as a critical diagnostic layer to track the validity of other sensor signals. Furthermore, by utilizing couples with varying sensitivities to solution resistance and reaction kinetics, this array allows the system to decorrelate the effects of parameters such as electrolyte conductivity and thickness. To establish a standardized baseline for environmental corrosivity at each micro-location, standard carbon steel calibration panels (E) are included in the assembly. The localized atmospheric "time of wetness", a critical driver for corrosion activity, is directly monitored using integrated leaf wetness (ToW) sensors (F). The specific corrosion behavior of

weathering steel is evaluated through a dual-faceted approach. This includes standard bare weathering steel coupons (G) for bulk mass-loss assessment, alongside advanced weathering steel thickness loss sensors (TLS) designed to provide continuous, high-resolution data on active corrosion rates (H).

Figure 5-2. Samples and sensors that were installed at each monitored area on the bridge: (A-D) Galvanic specimen using different combination of materials, (E) carbon steel calibration panels, (F) leaf wetness sensors, (G) weathering steel coupon, (H) weathering steel thickness loss sensor, (I and J) are not the object of this report.

A detailed description of the design, function, and purpose of each of these sensors and material specimens is provided in the subsequent sections.

5.2.1 Time of Wetness Sensor

The ToW sensor (**Figure 6-3**, F in **Figure 6-2**), manufactured by METER Environment, is designed to detect small amounts of water or ice on its surface. Frequently used in weather stations, this sensor provides a reliable and accurate measurement of the wetness of the environment. Combined with other sensors and samples in the context of corrosion monitoring, the ToW provides key information on the duration, intensity and frequency of wet events. It is a fully analog sensor which outputs a voltage of varying intensity depending not only on the fraction of the sensing surface that is wet but also on the conductivity of the electrolyte.

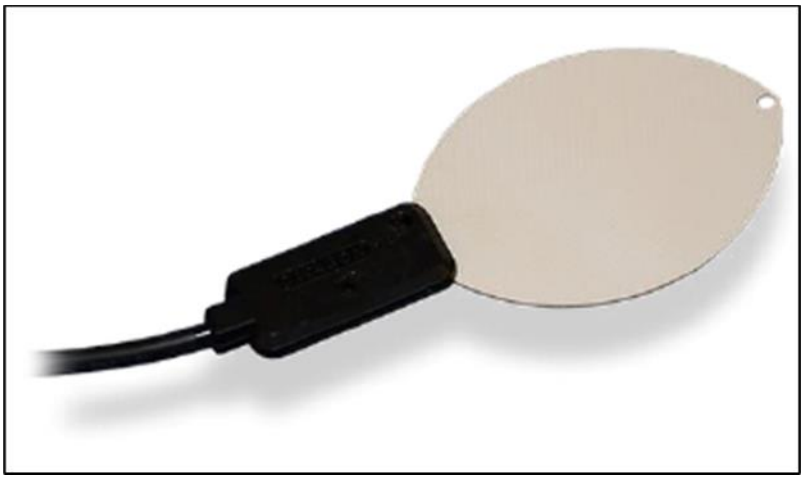

Figure 5-3. METER Environment LWS analog leaf wetness sensor.

5.2.2 Galvanic Corrosion Sensors

Galvanic corrosion is a prevalent, naturally occurring electrochemical phenomenon that is typically detrimental when multi-material assemblies are exposed to corrosive media. This process is initiated whenever three fundamental conditions are met: the materials must possess distinct corrosion potentials, both must be in contact with a common corrosive electrolyte, and an electrical connection must exist between them. In this configuration, the material with the higher (more noble) corrosion potential functions as the cathode and is protected, while the material with the lower (less noble) potential acts as the anode and undergoes accelerated corrosion.

Through strategic design and material selection, galvanic corrosion can be utilized to monitor environmental aggressiveness and characterize corrosion behavior. To quantitatively measure the localized driving force of galvanic corrosion between dissimilar structural materials, a modified sensor architecture was employed to allow for continuous in-situ monitoring. As depicted in the operational schematic (**Figure 6-4**), standard galvanic coupling, such as the interaction between a highly anodic aluminum alloy and a cathodic carbon fiber reinforced polymer (CFRP), involves direct physical contact. Under these native conditions, the electron flow generated by the anodic dissolution of the aluminum ($Al \rightarrow Al^{3+} + 3e^-$) travels directly across the material interface to facilitate cathodic reduction reactions on the CFRP ($O_2 + 2H_2O + 4e^- \rightarrow 4OH^-$), rendering the active corrosion current unmeasurable. To overcome this limitation, the experimental sensors were designed to physically decouple the anodic and cathodic elements. An inert dielectric layer is interposed between the two test materials, effectively preventing direct short-circuiting. Prior to assembly, the composite materials, such as the CFRP, are mechanically ground to remove the insulating polymer matrix and fully expose the active, conductive carbon fiber network. With direct internal electron transfer blocked by the dielectric barrier, the materials are electrically bridged via an external macro-cell measurement circuit. This configuration forces the galvanically generated electrons to

travel entirely through the external pathway. To quantify this flow without significantly impeding the natural corrosion kinetics, a precision 1Ω shunt resistor is integrated into the circuit. By utilizing the central datalogger to continuously measure the voltage drop across this known resistance, the active, real-time galvanic current can be directly and autonomously calculated using Ohm's law.

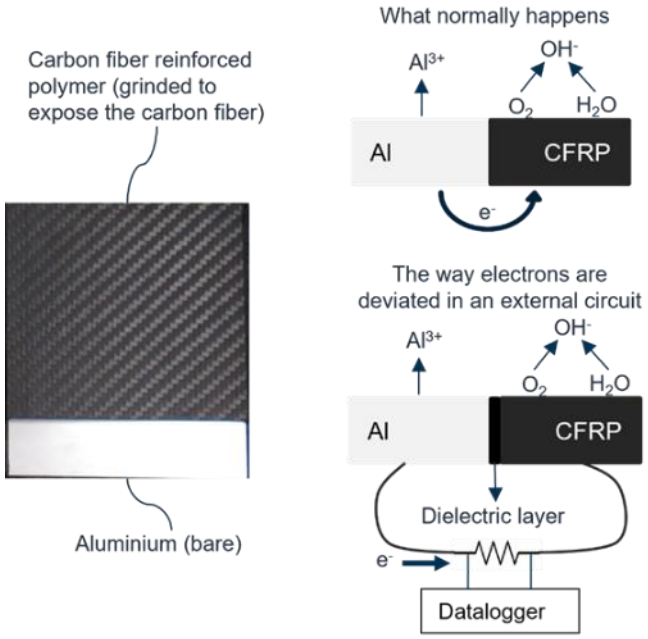

Figure 5-4. Physical configuration and operational schematic of the galvanic current sensors. A dielectric layer isolates the anodic and cathodic materials, routing the galvanically driven electron flow through an external measurement circuit equipped with a 1Ω resistor for continuous current quantification. In the shown sensor, the cathodic surface area (carbon fiber here) is the main corrosion driver.

Figure 6-2 illustrates the configuration of four distinct galvanic current sensors (designated A through D) deployed to monitor localized electrochemical activity. The specific material pairings for each sensor assembly, detailed in **Table 6-1**, were selected to evaluate a range of dissimilar metal interactions. These assemblies consist of carbon fiber reinforced polymer (CFRP) coupled with weathering steel (WS-CFRP), weathering steel coupled with 6061-T6 aluminum (WS-AA6061), a reference pairing of weathering steel (WS1.18-WS2.0), and CFRP coupled with 6022-T6 aluminum (CFRP-AA6022). These sensors are engineered to generate a measurable galvanic current only when the exposed metallic surfaces are physically bridged by a conductive electrolyte. Because the distinct electrochemical potential difference of each material combination drives the reaction, each sensor configuration provides a unique, highly specific quantifiable response to the prevailing environmental conditions at its installation site.

Table 5-1. Identification and material composition of the four galvanic specimen configurations (A–D) utilized to quantify dissimilar metal interactions and evaluate site-specific corrosive driving forces.

Reference in Figure 6-2	Materials (Top / Bottom in Figure 6-2)	Name
A	Weathering Steel 2.0 mm thick / CFRP	WS-CFRP
B	Weathering Steel (2.0 mm) / AA6061-T6	WS-AA6061
C	Weathering Steel 1.18 mm / Weathering Steel 2.0 mm	WS1.18-WS2.0
D	CFRP / AA6022-T6	CFRP-AA6022

Figure 6-5 shows the initial surface conditions of the bare weathering steel specimens, specifically the 2.0 mm and 1.18 mm thickness variants, prior to field deployment. A clear visual distinction is evident between the two panels, with one exhibiting a significantly darker (2.0 mm), grayer hue compared to the lighter, matte finish of its counterpart (1.18 mm). These color variations are physical indicators of distinct oxide layer characteristics, likely resulting from differences in the manufacturing process or the maturity of the mill scale. In a corrosion context, such visual heterogeneity is a surrogate for different electrochemical properties. **Figure 6-6** presents the electrochemical behavior of two weathering steel specimens, revealing that even when the bulk chemistry is identical, variations in surface oxide properties can establish a significant galvanic driving force. As shown in the open circuit potential (OCP) (a) and potentiodynamic polarization (b) plots, the distinct maturation and protective qualities of the individual patinas shift their respective corrosion potentials (E_{corr}), creating the ~170 mV gap observed between the noble (red) and active (blue) curves. Note that the potential is reported with reference to saturated calomel electrode (SCE), which has a zero value almost 75 mV below the zero voltage of $Cu/CuSO_4$ reference electrode, normally used in the field measurements. As a result, once coupled, the specimen with the less stable oxide layer will act as the anode, undergoing accelerated degradation to protect the more stable, cathodic counterpart. Finally, in **Figure 6-6b**, the intersection point of the anodic branch of the more active metal and the cathodic branch of the more noble metal provides the predicted galvanic corrosion current and the resulting mixed potential of the coupled assembly.

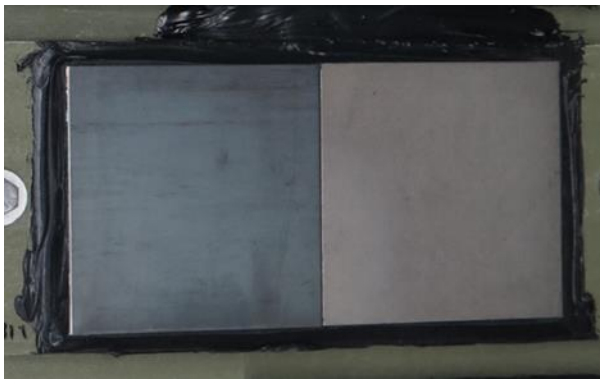

Figure 5-5. Typical surface condition of the bare weathering steel materials utilized in the monitoring array, illustrating the 2.0 mm (left) and 1.18 mm (right) variants.

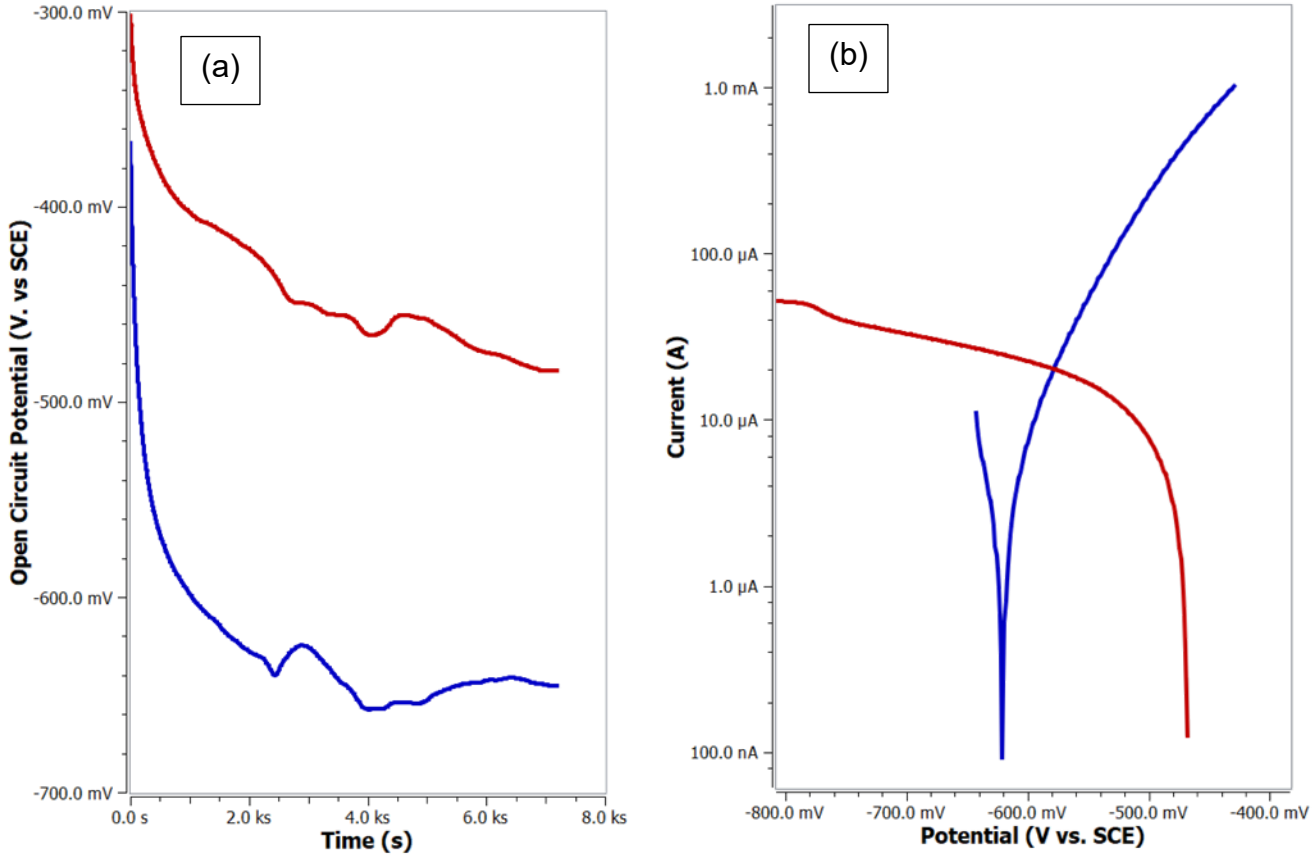

Figure 5-6. Electrochemical characterization of the 1.18 mm (blue) and 2.00 mm (red) thick weathering steel specimens in a naturally aerated 3.5% NaCl solution. (a) Open circuit potential (OCP) evolution over time, and (b) potentiodynamic polarization curves.

5.2.3 Connected Weathering Steel Thickness Loss Sensors

This sensor (H in **Figure 6-2**) was designed and fabricated for the autonomous, high-resolution quantification of weathering steel (WS) thickness loss (TL) across the bridge's diverse micro-climates. The corrosion monitoring was conducted using an electrical resistance (ER) method described in Diler *et al.* (2017) paper [39], in which governing equations can be found. This technique operates on the principle that the electrical resistance (R) of a metallic conductor evolves as a function of its resistivity (ρ) and its geometric dimensions. Because material resistivity is also dependent on temperature, the ER sensor utilizes a differential measurement approach to isolate material loss from temperature fluctuations. The probe consists of two specific tracks:

- **A sensing track:** Exposed directly to the environment, experiencing both material loss due to corrosion and ambient temperature variations.
- **A reference track:** Masked and protected from the corrosive environment, experiencing only temperature fluctuations.

By continuously measuring the resistance of both tracks (see **Figure 6-7**), the system compensates for temperature changes. The mean TL is dynamically calculated using the initial resistance values of the reference ($R_{ref,ini}$) and sensing ($R_{sens,init}$) tracks before exposure, alongside their respective continuous resistance values (R_{ref} and R_{sens}) measured throughout the exposure period.

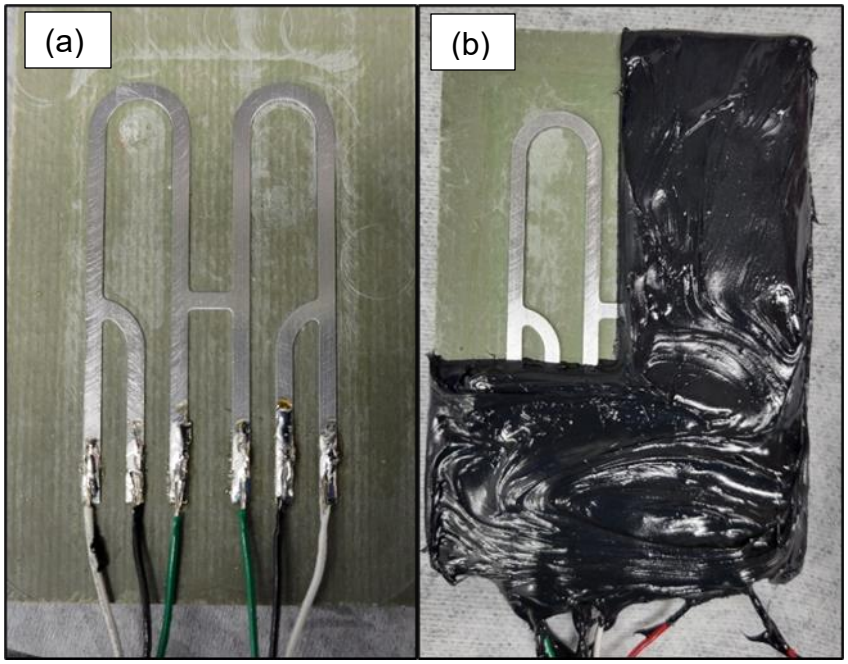

Figure 5-7. Preparation of the sensor assembly: (a) the exposed sensor elements prior to coating, and (b) the application of a protective sealant to isolate the reference side.

5.2.4 Weight Loss of Weathering Steel

5.2.4.1 WS Coupons on the Instrumented Panels

Standardized weathering steel (WS) mass-loss coupons (100 mm × 100 mm) were securely mounted at each monitoring location (G in **Figure 6-2**), co-located with the corresponding Thickness Loss Sensors (TLS). The physical thickness loss measured from these coupons is cross-referenced with the continuous data streams from the TLS units to validate and correlate real-time electrochemical kinetic measurements directly with long-term, macroscopic material degradation.

5.2.4.2 WS Coupons on the Side Rail Plate

To systematically evaluate how discrete seasonal variations influence weathering steel kinetics, a staggered exposure matrix was implemented for the mass-loss coupons on the side

rail plate. This dual-track strategy incorporates isolated single-season exposures (Winter, Spring, Summer, and Fall) alongside a cumulative annual set initiated in winter. By decoupling these environmental drivers, the methodology allows for the quantification of specific seasonal stressors, such as winter chloride loading versus summer thermal kinetics, while revealing how the initial “incubation” conditions dictate the long-term protective efficacy of the resulting rust patina.

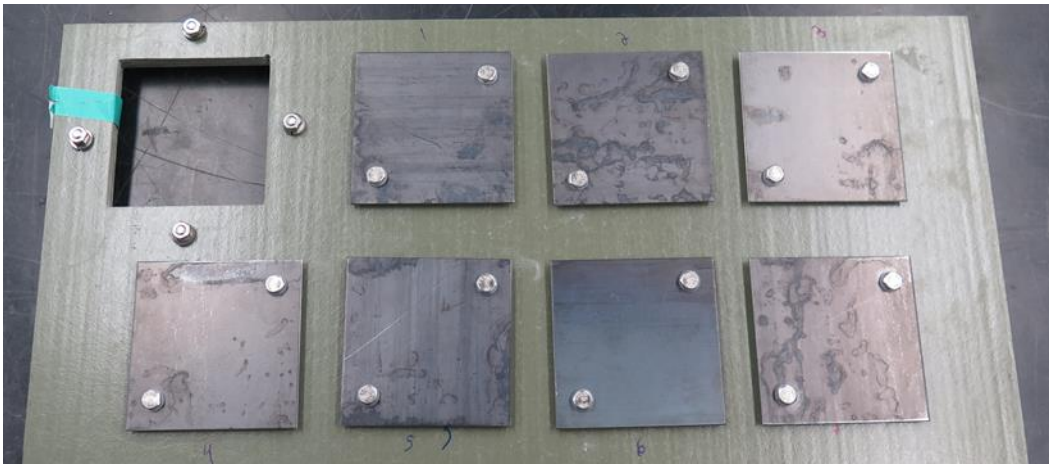

Figure 5-8. Configuration of the weathering steel mass-loss coupons mounted on the side rail plate. This physical array implements the staggered exposure matrix designed to systematically evaluate the influence of discrete seasonal environmental variations on the structural corrosion kinetics.

5.2.5 Thickness Loss on Cold Rolled Calibration Steel Panels

These calibration steel panels serve as the foundational baseline for determining environmental corrosivity levels according to ISO 9223. To accurately quantify the targeted thickness loss of an unprotected, flat steel surface under operational conditions, standardized cold-rolled steel panels (approximately 0.8 mm × 75 mm × 100 mm) were prepared for deployment (E in **Figure 6-2**). The bulk surface of these panels was subjected to a rigorous preparation protocol consisting of alkaline cleaning, a conversion coating, and an electro-coat (e-coat) application. To isolate the specific corrosion kinetics of the bare substrate, a precisely defined 19.0 mm × 63.5 mm rectangular window was intentionally left without the e-coat finish. During handling and field installation, this vulnerable bare steel region was shielded by a protective green tape. To ensure the absolute integrity of the initial surface state, this tape was removed precisely at the onset of the field evaluation, thereby exposing a perfectly fresh, uncontaminated bare steel surface directly to the ambient environment.

5.3 Autonomous Data Acquisition System and Sensor Network Architecture

A centralized, autonomous data acquisition system was engineered to continuously monitor environmental and electrochemical parameters across the bridge exposure sites. As illustrated

in the system architecture schematic in **Figure 6-9**, the network is built upon two primary Campbell Scientific datalogger enclosures, spatially separated by 100 feet cable routing. The entire monitoring network is self-sustaining, powered by a localized solar panel array coupled with a four-battery reserve bank. To capture high-resolution transient environmental events, the core program was configured to execute a complete data collection sweep at a uniform interval of 10 minutes.

To accommodate the high-channel-count sensor array, each CR1000X datalogger is equipped with channel expansion modules, specifically AM25T and 16/32B multiplexers. The system monitors eight distinct sensor clusters (corresponding to the eight plates). Every cluster uniformly incorporates one weathering steel thickness loss sensor and four galvanic current sensors (totaling 8 and 32 sensors, respectively). Furthermore, 13 ToW leaf sensors are strategically distributed among the clusters. A single ambient temperature and relative humidity probe (CS215) is integrated next to the first sensor cluster to establish baseline macro-environmental conditions.

The datalogger software was programmed utilizing measurement protocols tailored to the electrical requirements of each sensor type. The thickness loss sensors are interrogated using a full-bridge measurement instruction (BrFull), applying a precise excitation voltage to determine the micro-resistance changes correlated with material degradation. The 32 galvanic sensors are monitored via differential voltage instructions (VoltDiff) configured to a 200-mV range, capturing the minute voltage drops across precision shunt resistors to calculate active galvanic currents. The ToW leaf sensors are evaluated using a half-bridge configuration (BrHalf) to measure the electrical resistance of surface moisture films.

Remote data retrieval is facilitated by an RV50 4G LTE Sierra Wireless cellular modem integrated into the primary datalogger enclosure. This configuration enables the autonomous transmission of compiled 10-minute interval datasets over the Bell cellular network to a centralized server environment. Final automated archiving is executed via File Transfer Protocol (FTP) to a secure remote database, ensuring a continuous data stream for remote analysis and real-time performance monitoring.

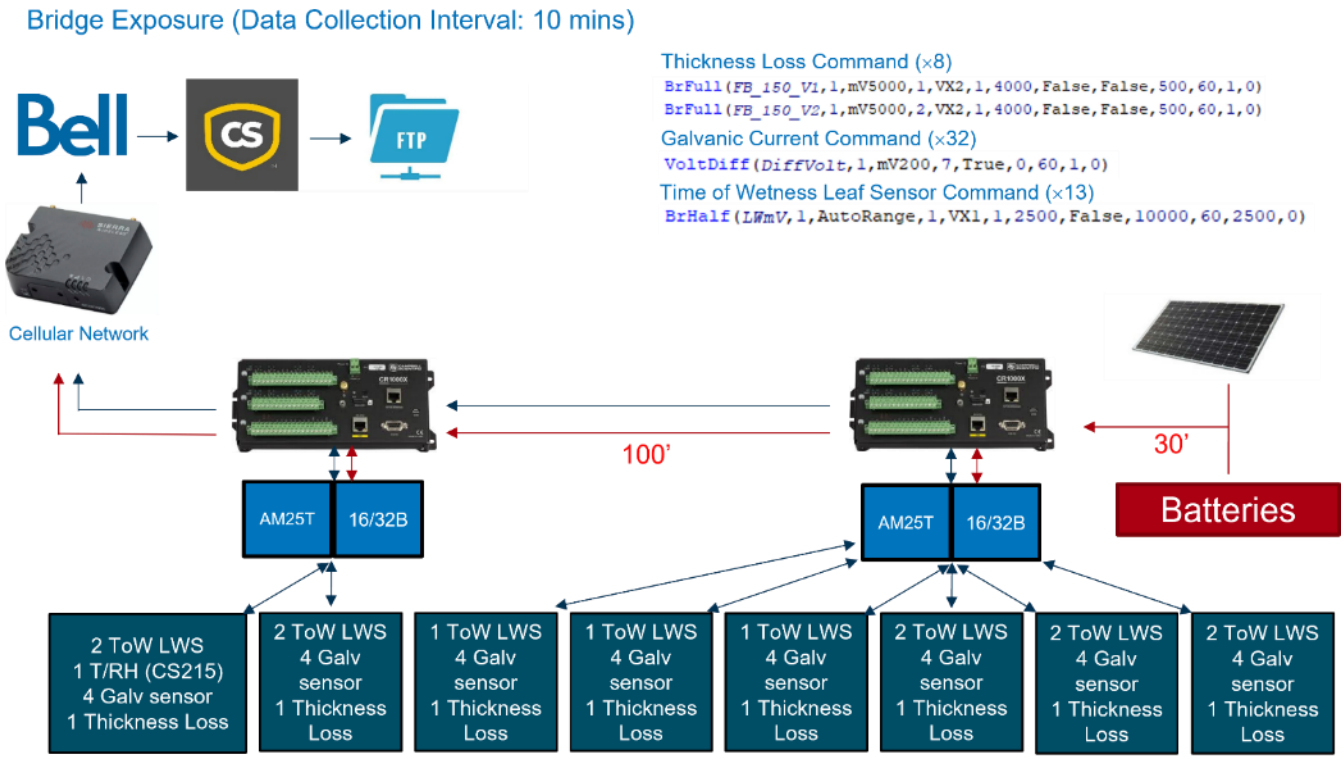

Figure 5-9. Schematic architecture of the autonomous data acquisition and transmission system. The network features dual Campbell Scientific dataloggers powered by a solar-battery array, integrating 8 thickness loss sensors, 32 galvanic current sensors, and 13 ToW sensors across eight monitoring sites. Data is transmitted via a cellular modem to a remote FTP server at 10-minute intervals.

5.4 Preparation of Mounting Plates with Coupons and Sensors

Figure 6-10 illustrates the mounting configuration of the galvanic sensor specimens on the 60 cm × 60 cm plates. To ensure long-term reliability in harsh service conditions, extensive volumes of sealants were applied to protect the pre-wired sensor leads and prevent electrolyte infiltration behind the assembly. This robust environmental sealing protocol was applied with identical rigor to all wired sensors across the entire monitoring network to maintain uniform protection of the electrical connections.

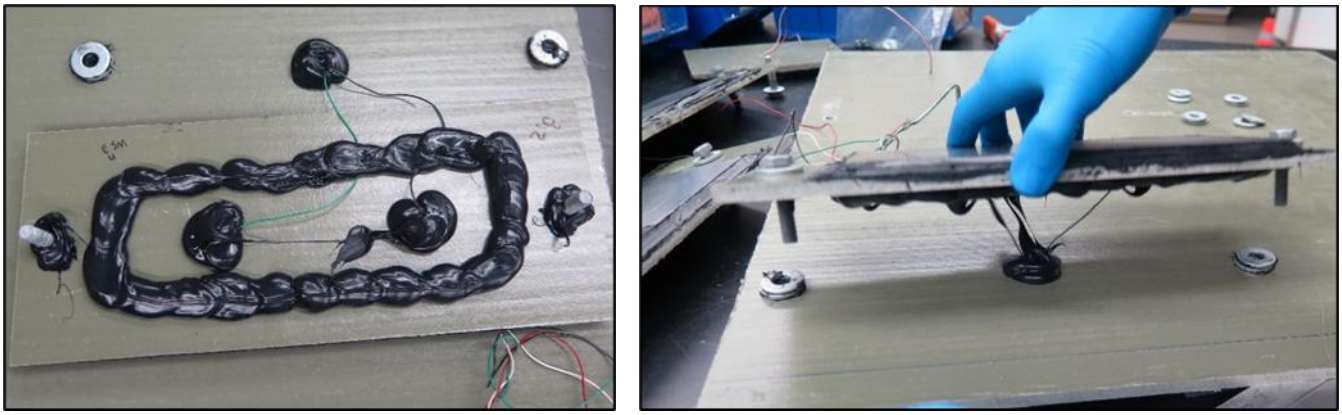

Figure 5-10. Installation detail of the galvanic sensor specimens on the 60 cm × 60 cm mounting plates. Extensive application of sealant is utilized to protect the pre-wired sensor connections and to ensure a moisture-tight seal, preventing electrolyte infiltration behind the sensor assembly.

Once the specimens are securely positioned, the sensor lead wires are routed along the rear of the 60 cm × 60 cm mounting panels (**Figure 6-11**). To ensure maximum durability against the aggressive bridge environment, these rear-mounted wires are fully encased within a thick, uniform layer of sealant. This additional protective barrier serves to immobilize the cabling against vibrations and provides a secondary line of defense against moisture ingress. Furthermore, all wires are inserted within a split loom tubing for the entire length between the plates and the instrument enclosures, ensuring the long-term integrity of the signal transmission to the central data acquisition system.

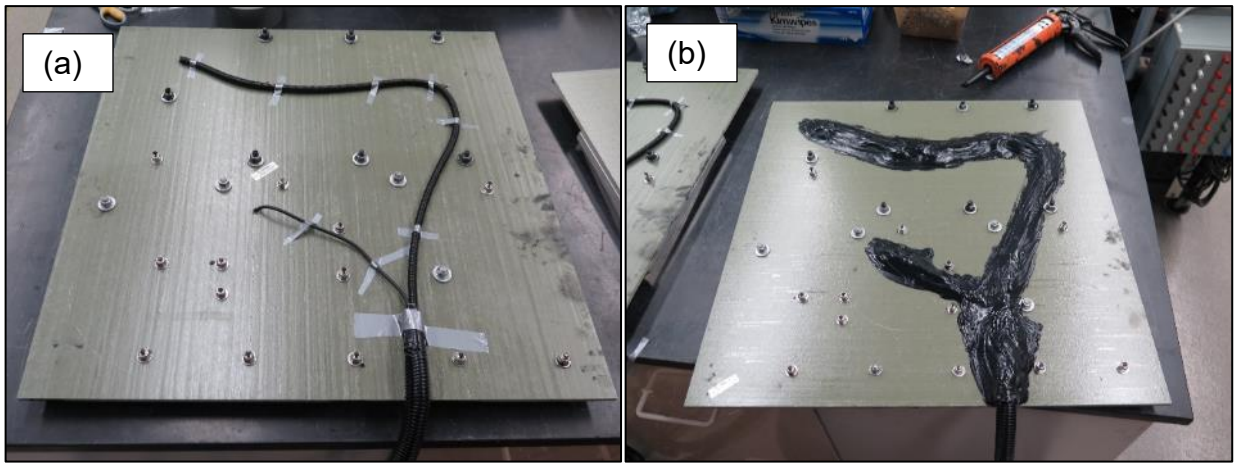

Figure 5-11. Rear view of the mounting panel illustrating the wire routing in a split loom tubing and protection protocol: (a) initial cable management and routing of sensor leads, and (b) the application of a thick sealant layer to environmentally isolate and secure the wiring against the structural substrate.

To ensure the electrochemical isolation of the sensors and specimens, plastic washers and inserts were utilized at all mounting points to prevent any direct metallic contact between the attachment bolts, nuts, and washers. For the mass-loss coupons (G in **Figure 6-2**), a specific

standoff distance was maintained to create an air gap at the rear of the samples. However, it is important to note that the subsequent analysis of these results must be conducted with care; the thickness loss on the sheltered rear surface is unlikely to be as significant as that on the primary forward-facing surface.

5.5 Installation of the Sensors on the Bridge

5.5.1 Selection of the Bridge

The targeted structure name is Highway 401 Underpass at County Road 2 & County Road 34 I/C, shown in **Figure 6-12**. It is the Highway 2 & 34 Interchange overpass, spanning 401 Highway in Lancaster, Ontario (45°08'11.3"N, 74°29'48.2"W). The site was selected for its high traffic volume and representative exposure to aggressive winter de-icing salts within a critical transportation corridor.

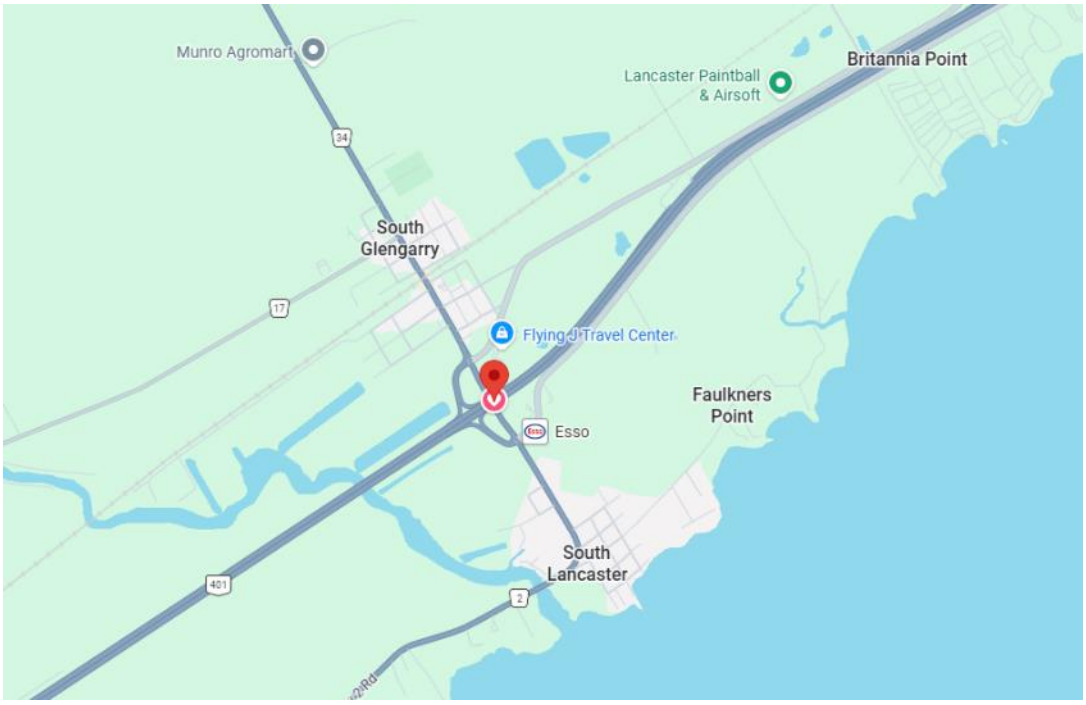

Figure 5-12. Geographical location of the monitored structure at the Highway 401 Underpass at County Road 2 & County Road 34 I/C", in Ontario, Canada (45°08'11.3"N, 74°29'48.2"W).

The monitoring equipment is installed on a multi-span highway overpass characterized by weathering steel box girders supported by reinforced concrete piers and abutments (see **Figure 6-13**). The site represents a complex corrosive environment, as the structure spans multiple high-speed traffic lanes where the lower flanges and webs of the girders are directly subjected to aerosolized de-icing salts and moisture plumes from vehicles below.

The sensor panels are distributed across various zones visible in the image, including:

Abutment wall: Visible on the far right, where baseline sheltered sensors are positioned.

Concrete piers: The vertical surfaces of the V-shaped piers provide mounting points for measuring corrosivity at different elevations from the roadway, on its left side.

Steel superstructure: The horizontal and vertical faces of the girders over the travel lanes and shoulders serve as the primary locations for evaluating the real-time WS thickness loss and galvanic currents.

Figure 5-13. Field perspective of the Highway 401 Underpass at County Road 2 & County Road 34 I/C. The image illustrates the primary installation environment, featuring weathering steel girders and reinforced concrete piers. Sensor plates are strategically distributed across these structural elements, including the abutment (right), the central piers, and the girder webs over the traffic lanes, to capture varying degrees of exposure to roadway splash and aerosolized de-icing salts.

The sensor mounting plates are secured to the bridge using hot-dip galvanized (HDG) mounting rails, which were strategically installed across the steel diaphragms (cross-frames, see **Figure 6-14**) between the primary weathering steel box girders. This arrangement provides a stable, rigid framework for the instrumentation while maintaining sufficient clearance from the girder webs to ensure representative airflow. The use of hot-dip galvanized steel for the mounting rails ensures long-term structural integrity of the support system itself. These rails allow for the secure attachment of the 60 cm × 60 cm mounting panels in various orientations as required by the experimental matrix.

In addition to the interior K-frame locations, the steel beam guide rails, visible in the foreground of **Figure 6-14**, serve as a secondary mounting environment. These rail's posts are utilized for

the staggered exposure matrix, where WS mass-loss specimens are installed at different intervals throughout the year. Mounting specimens in this specific location allows for the direct monitoring of seasonal effects, as the steel beam guide rails is highly susceptible to fluctuating environmental variables (e.g., Wind-driven rain, seasonal changes in the concentration of roadway and de-icing salt spray).

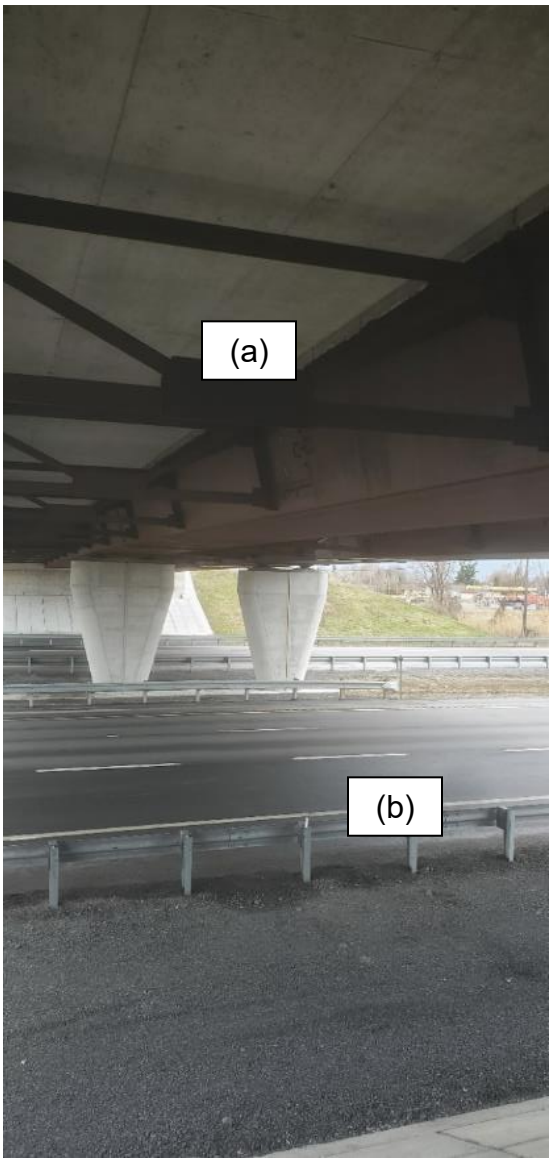

Figure 5-14. Perspective of the bridge's interior girders and the exterior steel beam guide rail. (a) The steel cross-frames between the box girders. These structural elements serve as the anchor points for the hot-dip galvanized mounting rails used to secure the experimental sensor panels. (b) The steel beam guide rail serves as a critical exposure site for the staggered WS mass-loss coupons; as these specimens are not mounted at height, they allow for straightforward seasonal retrieval. This accessibility facilitates a systematic evaluation of how discrete seasonal environmental variations influence the long-term corrosion kinetics of the weathering steel structure.

In **Figure 6-15**, the view from the bridge structure highlights the acceleration lane and the heavily traveled Highway 401 corridor, which serves as a major transportation artery through Ontario. The close proximity of the structural monitoring sites to this high-speed traffic flow ensures that the sensor arrays are consistently exposed to "splash-and-spray" zones. During the winter months, vehicles traversing these ramps and main lanes aerosolize runoff containing high concentrations of chloride-based de-icing salts. This transport mechanism delivers aggressive ions directly to the bridge's weathering steel girders and concrete supports, creating the high-corrosivity micro-climate for which its effect is monitored in real-time via the thickness loss and galvanic current sensors.

Figure 5-15. Panoramic view of the Highway 401 entry ramp and main corridor from the monitoring site.

5.5.2 Execution of Bridge Instrumentation

Sensor plates were strategically mounted at the structural locations shown in **Figure 6-16**, and detailed positions and orientations for each of these eight stations are provided in **Table 6-2**. **Figures 6-17** through **6-19** illustrate the comprehensive installation work conducted by the project team over the course of two nights. The installation of sensors and instruments on the bridge was conducted between 19 and 21 November 2024. The following series of images documents the progression of the deployment sensor cabling to the final positioning of the eight integrated monitoring plates across the bridge's structural spans. By performing the work during these overnight windows, the team was able to safely access high-exposure zones over the Highway 401 travel lanes while ensuring all solar power, telemetry, and sensor components were fully commissioned and verified for continuous data transmission.

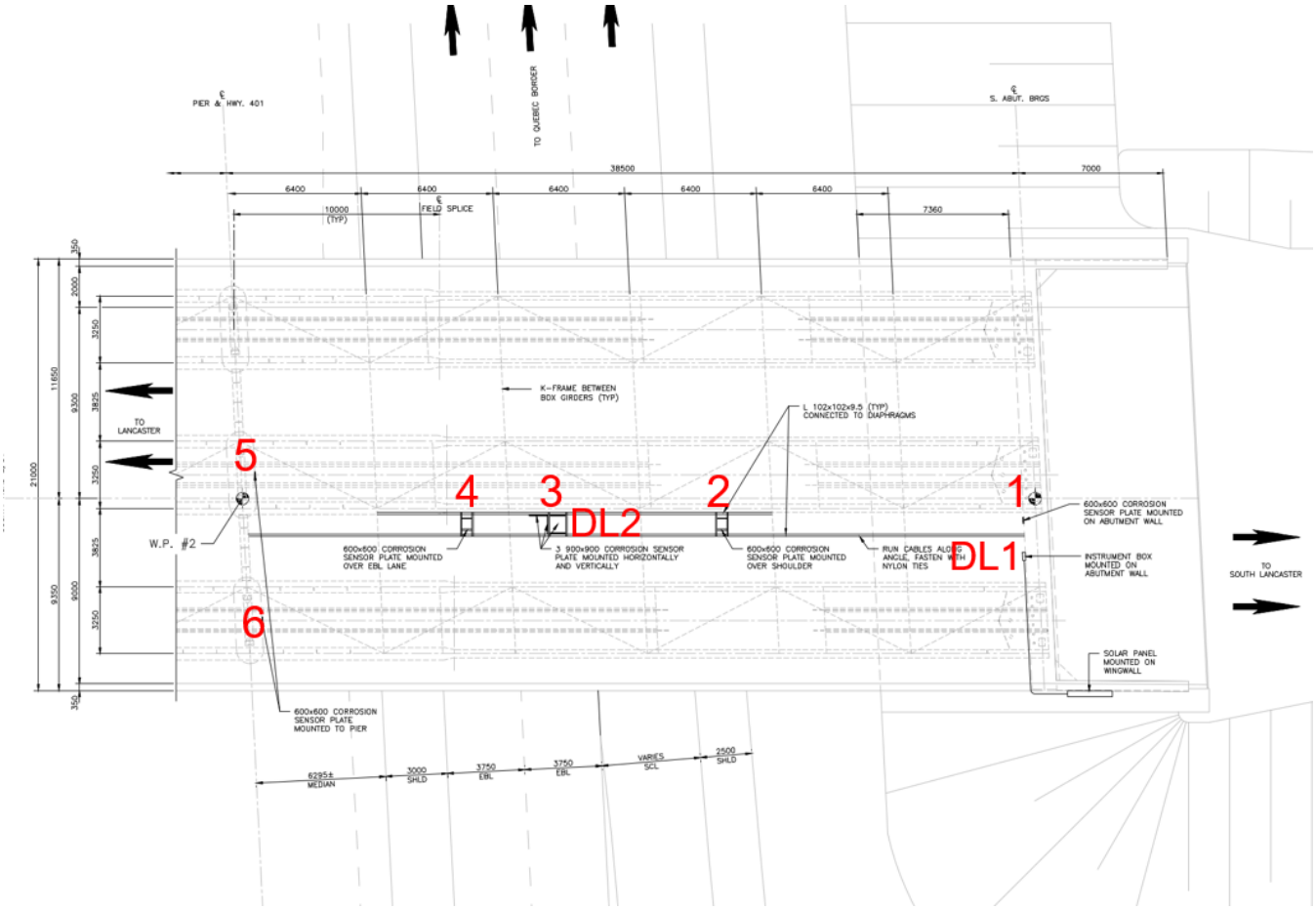

Figure 5-16. Structural plan view showing the spatial distribution of the eight sensor plates and the positioning of the two primary dataloggers (DL1 and DL2) relative to the abutment and structural spans. Plate 3 cluster evaluates the influence of orientation on corrosion rates above the #2 middle lane: Plate 3.1 faces downwards, Plate 3.2 is mounted vertically and parallel to traffic, and Plate 3.3 is mounted vertically and perpendicular to traffic, directly facing oncoming flow

Table 5-2. Spatial distribution and orientation parameters for the eight sensor-equipped monitoring plates.

Plate #	Position	Orientation
1	On the abutment wall, relatively far from the right side of the road	Vertical, parallel to traffic direction
2	Above the acceleration lane	Facing downwards, parallel to traffic direction
3.1	Above the #2 (middle) lane	Facing downwards, parallel to traffic direction
3.2	Above the #2 (middle) lane	Vertical, parallel to traffic direction
3.3	Above the #2 (middle) lane	Vertical, facing oncoming traffic
4	Above the #1 (left) lane	Facing downwards, parallel to traffic direction
5	Lower section of the second (middle) pier, at an approximate elevation of 2 m	Vertical, parallel to traffic direction
6	Top of the first pier	Vertical, parallel to traffic direction

Figure 5-17. Overview of the nighttime field operations, illustrating the Highway 401 lane closure and the vehicles utilized for the transport and deployment of monitoring instrumentation.

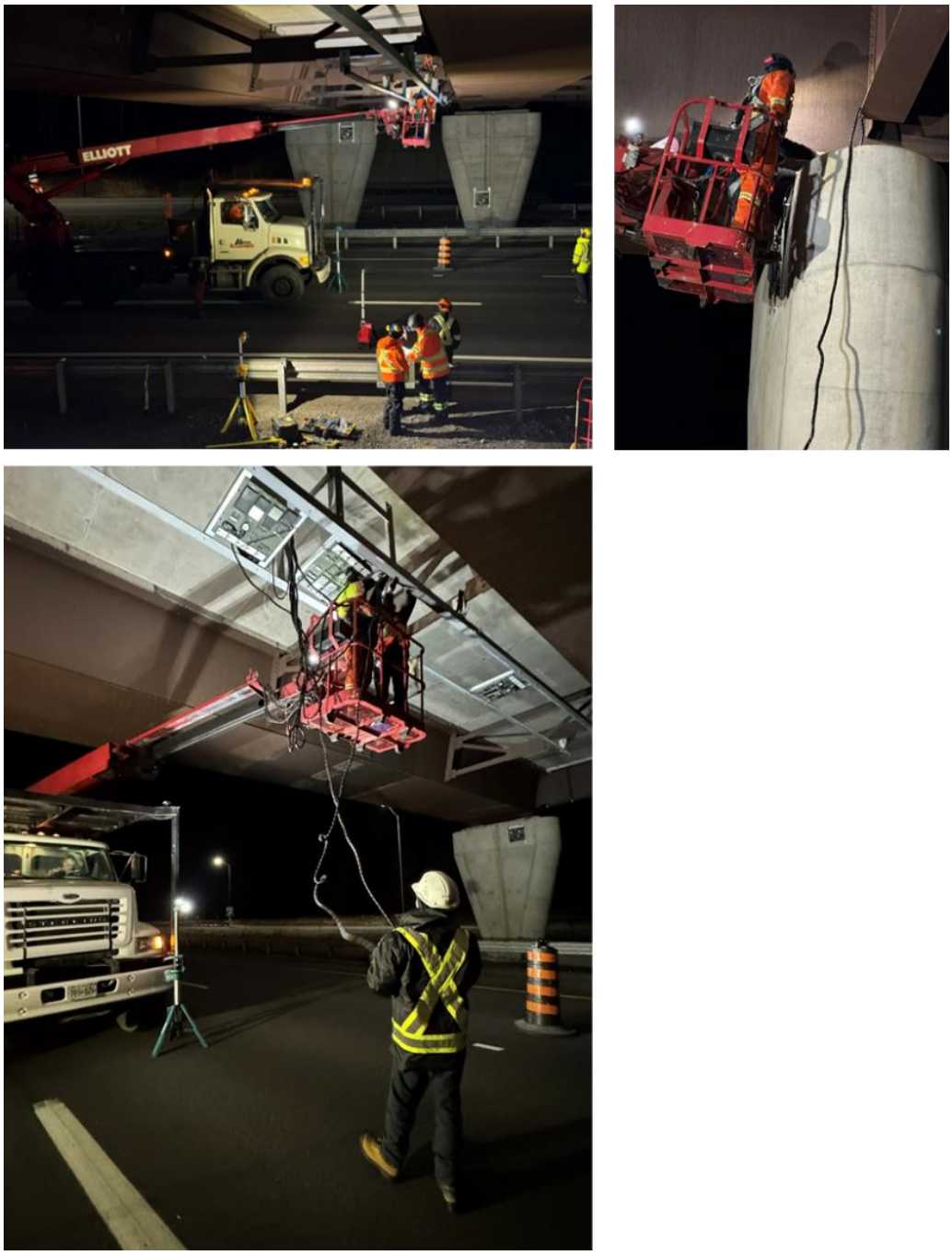

Figure 5-18. Field photographs documenting the nighttime installation work to secure specimen plates at various locations on the bridge. ***Top left:*** *workers in a mobile elevated work platform are being raised towards the superstructure between box girders;* ***Top right:*** *workers in a basket mount a specimen plate on a pier, close to the girder;* ***Bottom left:*** *workers in a basket attach specimen plates over the slow lane, with another worker assisting and managing wiring and safety perimeter on the ground.*

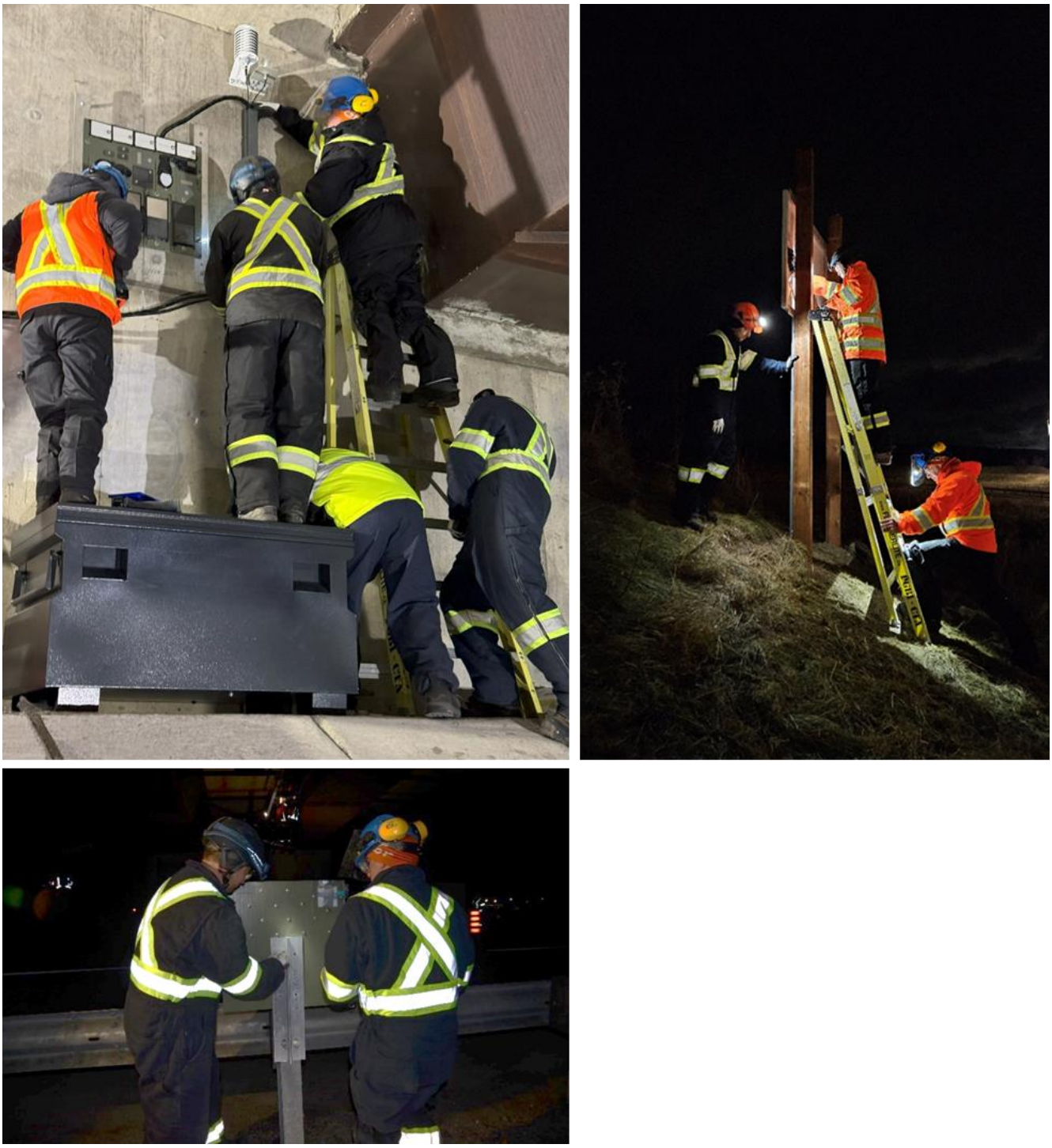

Figure 5-19. Final commissioning of the key system components. ***Top left:*** *installation of Plate 1 on the abutment wall along with the integrated T/RH sensor;* ***Top right:*** *deployment of the solar panel array on the embankment.* ***Bottom left:*** *mounting of the WS mass-loss specimen holder on the side rail's post.*

5.5.3 Final Configuration and Deployment of the In-Service Monitoring Network

Figure 5-20. View of the autonomous solar power system. The panel is mounted on a rigid support structure on the south-facing embankment to provide a continuous renewable energy source for the bridge's remote monitoring and data transmission instrumentation.

Figure 5-21. Detailed view of the right abutment wall. This installation includes Plate 1, positioned vertically to serve as a baseline monitoring site, and an integrated T/RH sensor for local atmospheric data collection. On the flat surface against the abutment wall is positioned the weather-resistant enclosure that houses the system batteries and the main datalogging hardware. Cables are neatly routed and protected, ensuring long-term structural monitoring and continuous data transmission from this central hub.

Figure 5-22. Close-up view of the mounting plate secured to the rail post. This station holds a series of weathering steel (WS) mass-loss coupons, specifically configured to monitor the corrosive impact of seasonal variations and roadway splash at the structure's exterior boundary.

Figure 5-23. Wide-angle view of the structural monitoring system in place after the final day of installation. The image captures the sensor plates mounted across the concrete piers and the weathering steel box girders.

Figure 5-24. Detailed view of the monitoring stations installed on the primary mounting rail over the acceleration lane and #2 middle lane. In the foreground, the Plate 3 cluster evaluates the influence of orientation on corrosion rates above the #2 middle lane: Plate 3.1 faces downwards, Plate 3.2 is mounted vertically and parallel to traffic, and Plate 3.3 is mounted vertically and perpendicular to traffic, directly facing oncoming flow. In the background, at the farthest extent of the rail, Plate 2 is positioned to monitor the micro-climate specifically associated with the acceleration lane.

Figure 5-25. Interior longitudinal view of the mounting rail system spanning the primary bridge girders. The image illustrates the sequential positioning of the instrumentation stations from front to back (top to bottom of photograph): Plate 2 (situated above the acceleration lane), the Plate 3 cluster (above the #2 middle lane), and Plate 4 (at the farthest extent above the #1 left lane). This alignment ensures that the monitoring network covers the full width of the traffic-induced spray.

Figure 5-26. Interior view of the bridge superstructure highlighting the instrumentation mounted on the reinforced concrete support piers. Plate 5 is installed on the lower section of the second pier (right), positioned at a standardized "splashing height" to monitor high-intensity roadway runoff. Plate 6 is secured to the upper section of the first pier (left), near the girder interface, to evaluate the corrosivity of the environment at a higher elevation. The central mounting rail and its associated over-lane sensor clusters are also visible, illustrating the vertical and horizontal distribution of the monitoring network.

The layout as presented in **Figure 6-27** provides a comprehensive overview of the instrumentation as it currently exists in the field. After two days of on-site work, all eight primary monitoring stations were secured to their respective locations, ranging from the sheltered abutment walls to the high-exposure zones above the traffic lanes.

The figure serves as a final record of the deployment, documenting:

- **Final hardware positioning:** The successful mounting of the solar power array, cellular telemetry units, and dual datalogger enclosures.

- **Spatial orientation:** The final placement and orientation (vertical, horizontal, or traffic-facing) of Plates 1 through 6, ensuring each station is correctly positioned to capture its intended micro-climate.
- **Specimen matrix:** The finalized configuration of the 60 cm × 60 cm panels, with all specimens and electronic sensors fully integrated, sealed, and wired for continuous data collection.

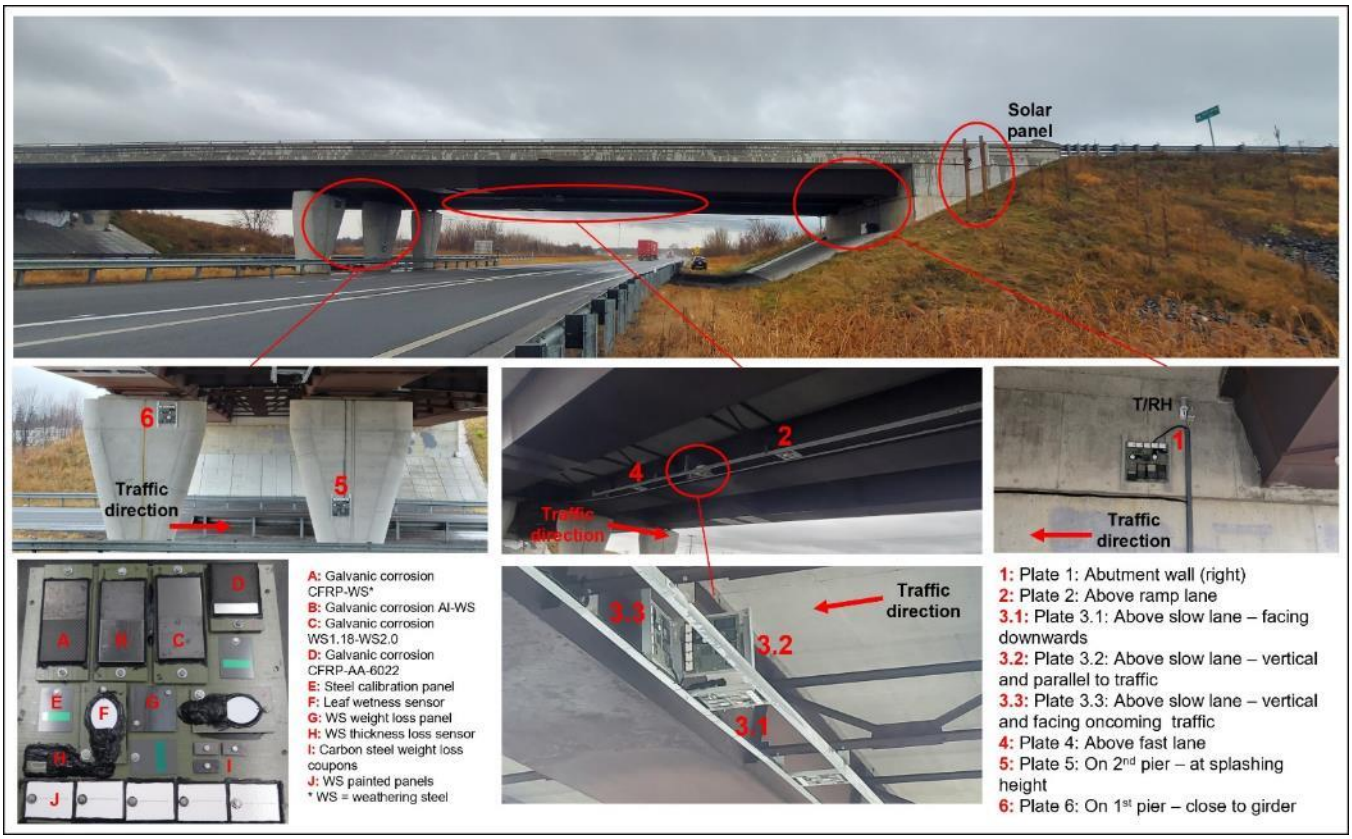

Figure 5-27. Comprehensive layout of the bridge monitoring system. The primary image shows the global positioning of the solar power supply and sensor clusters. Insets provide detailed views of the structural mounting locations (Plates 1–6) and the standardized configuration of the experimental specimens integrated onto each mounting panel. Please note the (I and J) are not the object of this report

5.6 Corrosion Measurements Procedures in Laboratory

5.6.1 Accelerated Laboratory Testing: GMW14872 Cyclic Corrosion Exposure

An 8-week accelerated cyclic corrosion test (CCT) was performed to define the laboratory parameters necessary to accurately replicate the corrosion kinetics and material degradation observed at Lancaster bridge (Hwy 401 Underpass at County Road 2 & County Road 34 I/C). The primary objective of this phase is to identify the specific environmental conditions under

which in-field results can be reliably mimicked in a controlled setting, thereby establishing a robust correlation between laboratory performance and field data for both Thickness Loss Sensors (TLS) and traditional Weight Loss (WL) coupons. This validated relationship enables the direct assignment of ISO 9223 corrosivity classifications (C1 through Cx) to various bridge micro-climates based on real-time TLS data streams. The results stemming from the evaluation are not just applicable to steel and steel coatings but also to the characterization of the chloride loading environments for reinforced concrete and prestressed concrete durability monitoring.

5.6.1.1 Test Methodology and Parameters

The exposure was performed in a Q-Lab cyclic corrosion chamber using the GMW14872 (formerly GM 9540P) protocol. This cycle is widely recognized for its ability to simulate realistic outdoor corrosion mechanisms through a complex sequence of salt mist, humidity, and drying phases.

- **Test solution:** 1% NaCl + 0.25% sodium bicarbonate ($NaHCO_3$) (no addition of $CaCl_2$).
- **Claimed correlation factor:** 80 days of exposure under this protocol is considered equivalent to approximately 3 to 4 years of in-service environmental exposure [12].
- The 24-hour cycle:
    1. Repeat steps 2-4, 4×.
    2. 25°C / 45% RH for 27 minutes.
    3. Salt shower at 25°C for 3 minutes.
    4. 25°C / 45% RH for 1.5 hours.
    5. 49°C at 100% RH for 7.5 hours (including a 1-hour linear ramp).
    6. 49°C at 95% RH for 30 minutes.
    7. 60°C at 25% RH for 8 hours (including a 3-hour linear ramp).
    8. Go to step 1.

5.6.1.2 Specimens Configuration and Preparation

A total of 80 individual specimens and sensors were prepared and monitored. All coupons were degreased using acetone followed by hexanes to ensure a contaminant-free surface prior to initial weighing.

Table 5-3. Summary of specimen types, material specifications, and removal frequency for the 8-week laboratory cyclic corrosion test (CCT).

Specimen Type	Material	Weekly Removal	Total
Steel WL	Carbon Steel 1010 (50 mm × 50 mm)	3 units	24 units
Zn WL	Zn 99% pure (50 mm × 50 mm)	3 units	24 units
Calibration steel panels, TL	Cold rolled steel (CRS)	3 units	24 units
Connected WS TLS	Weathering steel (0.70 mm)	1 unit	8 units

5.6.1.3 Additional Monitoring

- **Galvanic Specimens:** 3× CFRP-AA6022 assemblies to monitor dissimilar metal interactions.
- **Time of Wetness (ToW):** 1× sensor mounted at 20° relative to vertical to track surface moisture duration throughout the cycles.

5.6.1.4 Spatial Distribution and Removal Protocol

To mitigate localized variations within the chamber ("edge effects"), specimens were distributed evenly across the internal volume:

- **Suspended specimens:** Steel and Zn WL coupons were hung via tie-wraps on suspension bars using a ¼" hole in the corner, ensuring no physical contact between samples.
- **Slotted bar specimens:** Calibration panels, CFRP-AA6022 assemblies, and ToW sensors were mounted at a 20° angle relative to the vertical plane.

5.6.1.5 Weekly Sampling

On Friday mornings, the chamber was paused during the ambient phase (25°C / 45% RH). Samples were collected from varying positions within the chamber to ensure a statistically representative average of the corrosion rate for that time interval. For each removal, the exact date and cumulative chamber hours were logged to maintain a precise time-to-corrosion-loss curve.

5.6.2 Post-Exposure Processing and Deoxidation Protocols

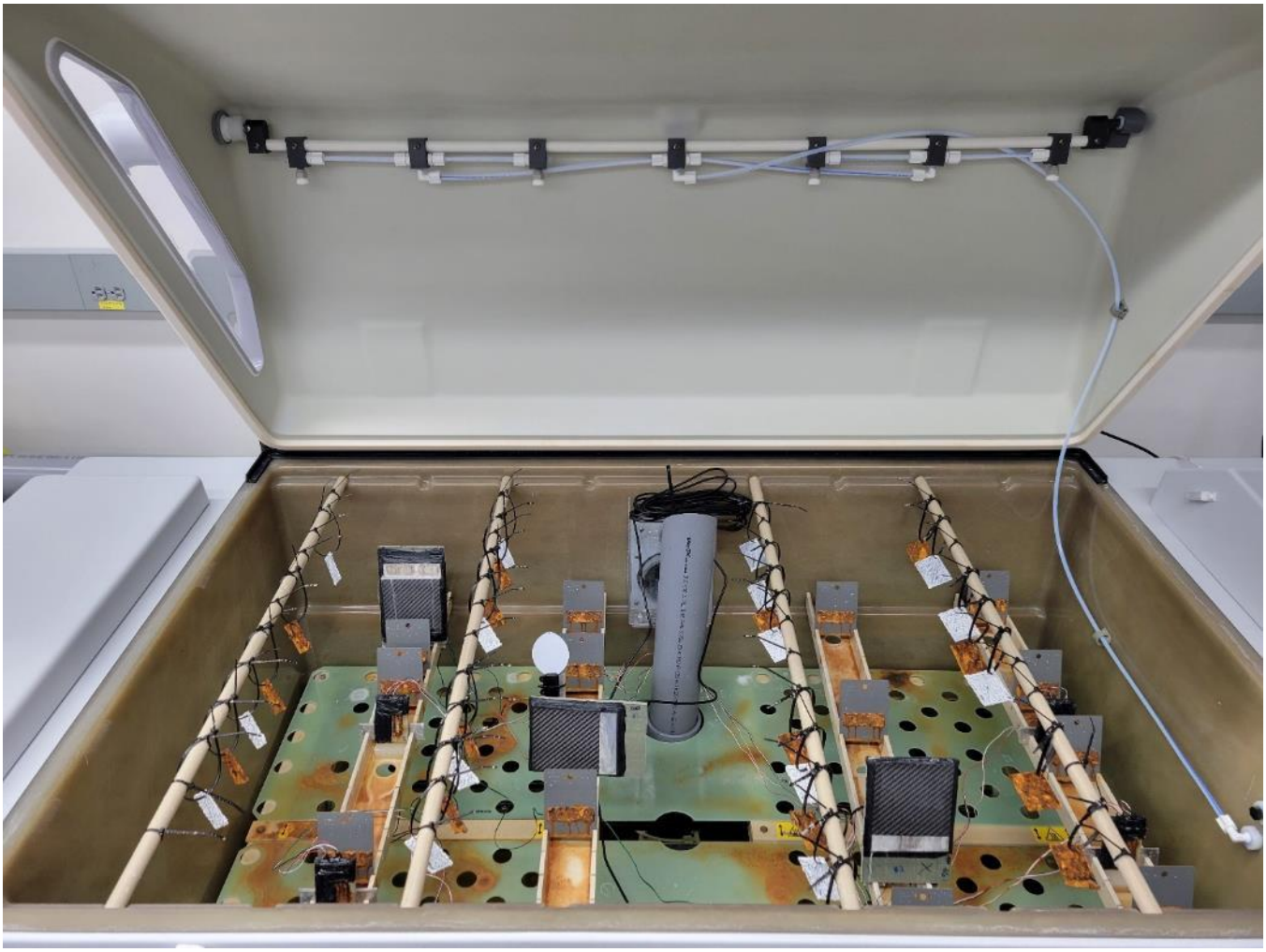

Figure 5-28. Interior view of the Q-Lab cyclic corrosion chamber (at the end of Week 4) illustrating the experimental setup for the GMW14872 exposure. The image shows the systematic distribution of carbon steel and zinc weight-loss coupons suspended from the upper bars, alongside instrumented weathering steel TLS sensors and CFRP-AA6022 galvanic assemblies mounted at a 20° angle on the slotted floor rails. This configuration ensures uniform exposure to the salt mist and humidity cycles for all 80 specimens.

5.6.2.1 Weight Loss Coupons (Steel and Zinc)

To determine mass loss, the 50 mm × 50 mm steel and Zn (base metal) coupons were processed through a multi-stage cleaning and deoxidation sequence:

- Immediate Stabilization: Within the first hour of removal, specimens were rinsed with deionized (DI) water and dried using a pressurized nitrogen (N_2) stream.
- Mechanical Pre-Cleaning: Loose oxides were removed manually using a plastic brush under running tap water, then patted dry with industrial wipes.
- Chemical and Mechanical Deoxidation:
  - Steel: Immersion in the deoxidizing solution for a maximum of 25 minutes at 20-25 °C. Solution C3.2, as per standard ISO 8407: 1000 mL of concentrated HCl (ρ = 1.19 g/mL) + 20 g Sb_2O_3 + 50 g $SnCl_2$.
  - Zinc: Immersion in the deoxidizing solution C9.1 for a maximum of 10 minutes at 20-25 °C. Solution C9.1, as per standard ISO 8407: 250 g of glycine in a 1-L solution. In cases where solution C9.1 proved insufficient, use Solution C9.2, as per standard ISO 8407: 100 g of ammonium chloride in a 1-L solution (5 minutes at 70°C).
  - For both steel and Zn, in cases where chemical cleaning procedures proved insufficient, light grit-blasting was employed (white alumina grit 220 at 80 psi) to achieve a clean metallic surface.
  - In all instances, the selected deoxidation methods, whether chemical or mechanical, must be carefully controlled to ensure negligible attack or metal loss of the base substrate.
- Final Weighing: Cleaned specimens were rinsed under tap and DI water and dried in an oven at 50°C for 2 hours. Final weights were recorded once the samples reached room temperature.

5.6.2.2 Calibration Steel Thickness Loss Panels

The calibration steel panels were processed specifically for cross-sectional metallographic analysis:

- Cleaning: Specimens were rinsed with tap water and brushed to remove surface oxides within the first hour. After a final DI water rinse and N_2 drying, they were oven-dried at 50°C for 3 hours.
- Sectioning: Each panel was subjected to three strategic cuts to expose representative cross-sections of the corroded and uncorroded (protected) zones.
- Imaging: Microscopic imaging was used to collect 30-40 thickness measurements within the central corroded area and 5-10 measurements on the lateral uncorroded reference zones (see **Figure 6-29**). This differential allows for a precise calculation of total thickness loss.

(a)

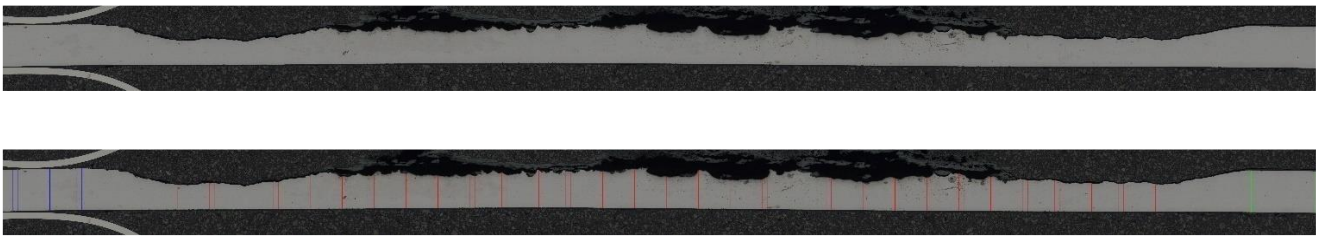

(b)

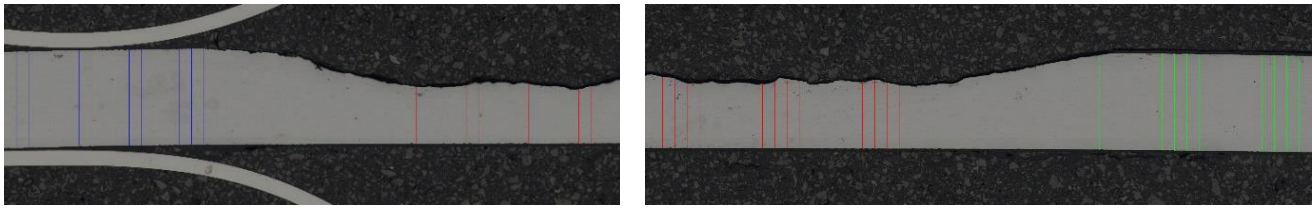

Figure 5-29. Microscopic cross-sectional images of the sensor element illustrating the differential thickness measurement technique, with colored markers denoting in red the 30-40 sampling points within the central corroded region (a), and in blue and green the 5-10 reference measurements on the lateral uncorroded zones (b).

5.7 Evaluation of Carbon Steel and Zinc Corrosion Behavior Under GMW14872 Exposure

5.7.1 Analysis of Mass Loss Kinetics: Overview of Carbon Steel vs. Zinc

The characterization of material degradation under accelerated conditions is fundamental to establishing the long-term structural health profile of the monitored bridge. The dual-axis plot (**Figure 6-30**) illustrates the cumulative mass loss of carbon steel and zinc specimens subjected to the GMW14872 cyclic corrosion protocol over a total duration of 1,236 hours (8 weeks).

The experimental results demonstrate a significant divergence in the corrosion kinetics between the two alloy systems. Carbon steel (represented on the primary blue Y-axis) exhibits a near-linear progression of mass loss throughout the exposure period, reaching a final value of approximately 2900 g/m^2. This linear trend indicates that the iron oxide (rust) layers formed under these specific cyclic conditions, alternating between salt spray, high humidity, and drying phases, are porous and non-protective. Consequently, the electrolyte maintains consistent access to the reactive base metal, preventing any stabilization of the corrosion rate. This

shows that the first year corrosion rate normally presented in standards, such as those reported in Table 4-1 may not be conservative.

In contrast, zinc (represented on the secondary orange Y-axis) displays substantially lower overall degradation, with a peak mass loss of approximately 750 g/m^2. It is important to note that the secondary axis scale is approximately three times smaller than that of the primary axis, highlighting the inherent corrosion resistance of zinc in chloride-rich environments. The zinc curve exhibits a prominent “hump” near the 800-hour mark, followed by a distinct plateau in the corrosion rate. This trend is characteristic of the formation of adherent corrosion products that provide a physical barrier effect, effectively hindering further oxidation. Because the development and stability of this protective layer occur stochastically, with varying degrees of efficacy across individual specimens, the resulting inconsistency in localized protection accounts for the escalating standard deviation (SD) observed in the zinc data as the exposure progresses.

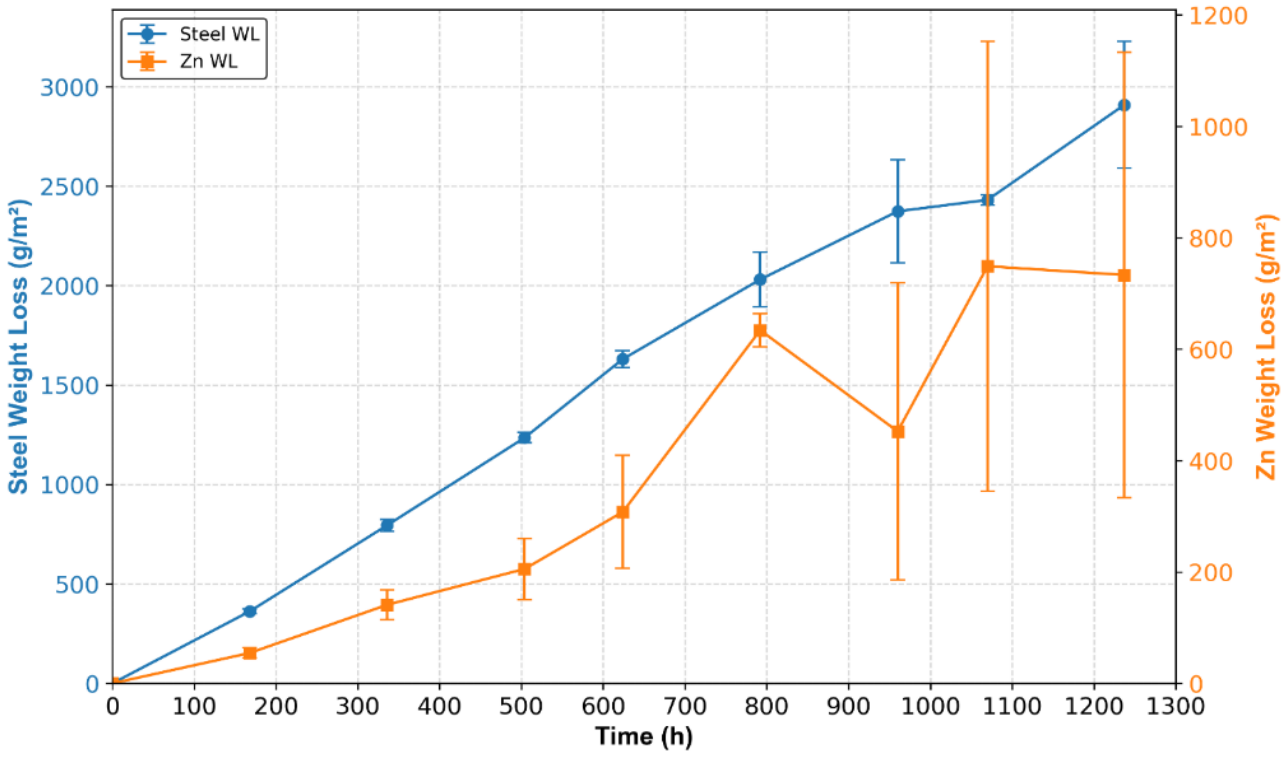

Figure 5-30. Cumulative mass loss (g/m^2) as a function of exposure time (h) under GMW14872 cyclic conditions. The data points represent the mean of three independent specimens, with error bars indicating one standard deviation. Note the distinct scales for Steel (left) and Zinc (right).

5.7.2 Analysis of Carbon Steel Mass Loss and ISO 9223 Corrosivity Mapping

To contextualize the laboratory results within international standard frameworks, the cumulative mass loss of the carbon steel specimens was mapped against the ISO 9223 corrosivity categories (C1 through CX). This mapping, illustrated in **Figure 6-31**, provides a clear benchmark for the aggressiveness of the GMW14872 protocol relative to standardized environmental classifications.

The experimental data reveals a rapid progression through the lower ISO corrosivity tiers. Within the first 125 hours of exposure (as highlighted in the inset “Zoom” plot), the steel specimens quickly surpass the C1 (Very Low) and C2 (Low) thresholds. By the 168-hour mark (Week 1), the material has already entered the C3 (Medium) category, which typically represents urban or coastal environments with moderate sulfur dioxide or chloride levels. As the exposure continues, the slope of the mass loss curve remains steep and predominantly linear. The specimens transition through the C4 (High) and C5 (Very High) zones within the first 300 hours. By the conclusion of the 8-week test (~1250 hours), the cumulative mass loss reaches approximately 2,900 g/m^2, placing the environmental conditions firmly within the CX (Extreme) category. The transition from C1 to CX within 600 hours underscores the high acceleration factor of the GMW14872 protocol. While ISO 9223 categories are traditionally based on one-year outdoor exposure values, the laboratory environment achieves “Extreme” classification by maintaining a high Time of Wetness (ToW) and aggressive chloride concentrations. The almost linear progress of the curve, until the end of the C5 zone, confirms that no protective rust scale is forming on the carbon steel. However, as the specimens progress deep into the CX zone, there is a notable increase in the standard deviation (SD) values. While the variance remains minimal during the initial tiers, the error bars expand significantly during the final weeks of exposure. This phenomenon suggests that under “Extreme” corrosivity conditions, the degradation mechanism becomes increasingly heterogeneous. At these high mass-loss levels, the accumulation of thick, bulky corrosion products, while non-protective, can create localized micro-environments on the coupon surfaces. Variations in the moisture retention and chloride entrapment within these heavy rust layers likely lead to the observed divergence between replicates.

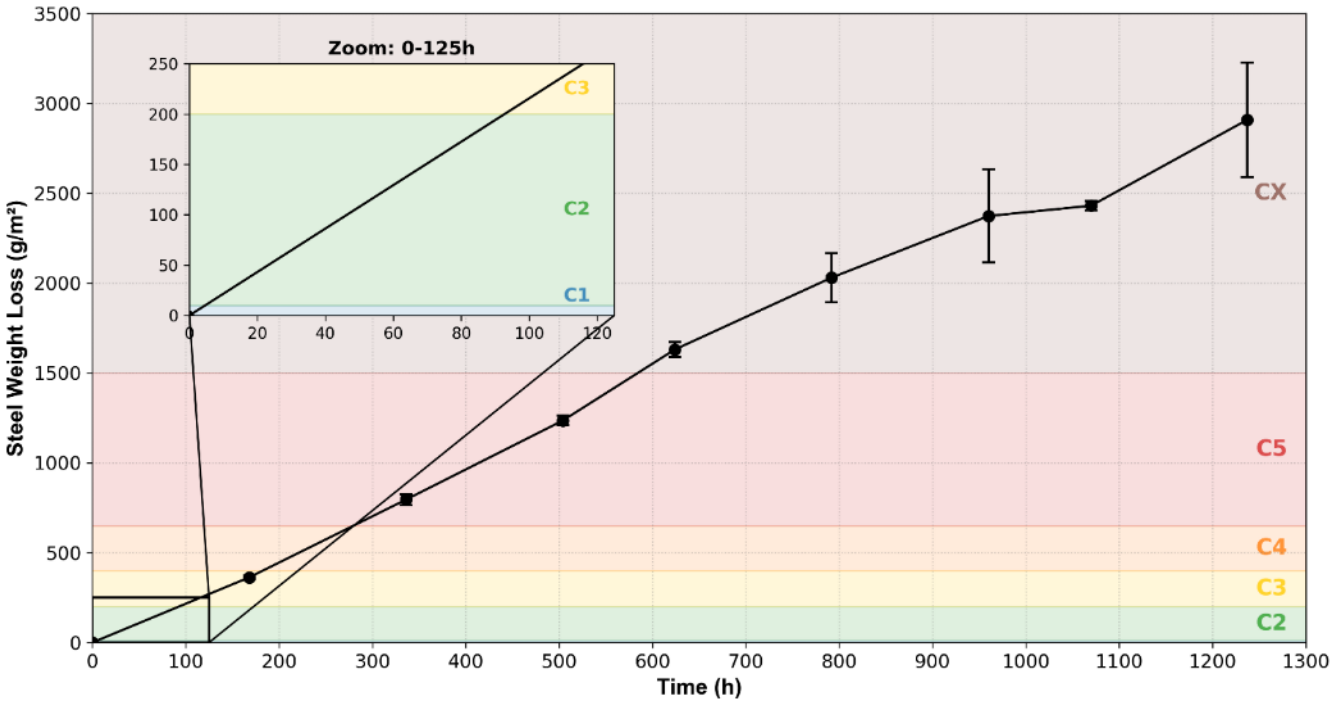

Figure 5-31. Weight loss of carbon steel (g/m^2) as a function of exposure time (h), indexed against ISO 9223 corrosivity categories (C1 through CX) with an inset detail highlighting the interpolated initial mass loss within the C1, C2, and C3 zones.

5.7.3 Analysis of Zinc Mass Loss and ISO 9223 Corrosivity Mapping

The mapping of zinc mass loss against the ISO 9223 corrosivity categories (**Figure 6-32**) provides a critical secondary validation of the GMW14872 protocol's aggressiveness. While zinc is inherently more corrosion-resistant than carbon steel, its progression through the ISO tiers highlights the extreme nature of the laboratory environment, particularly concerning galvanized components. As shown in the inset "Zoom" plot in **Figure 6-32**, the transition through the initial corrosivity stages occurs almost instantaneously. Assuming a linear trend from the beginning of the exposure, it is seen that the zinc specimens surpass the C1 (Very Low), C2 (Low), and C3 (Medium) thresholds within the first 20 hours of exposure. By the end of the first week (168 hours), the cumulative mass loss has already reached the C5 (Very High) category, at 10 hours of reaching the CX (Extreme) zone. The zinc curve exhibits a slight upward curvature (acceleration) as it goes beyond the CX zone after ~ 450 hours. As zinc corrosion products accumulate over time, they form thick, non-uniform layers that stochastically trap chlorides and moisture, leading to divergent localized attack across replicates, directly resulting in the observed increase of standard deviation values.

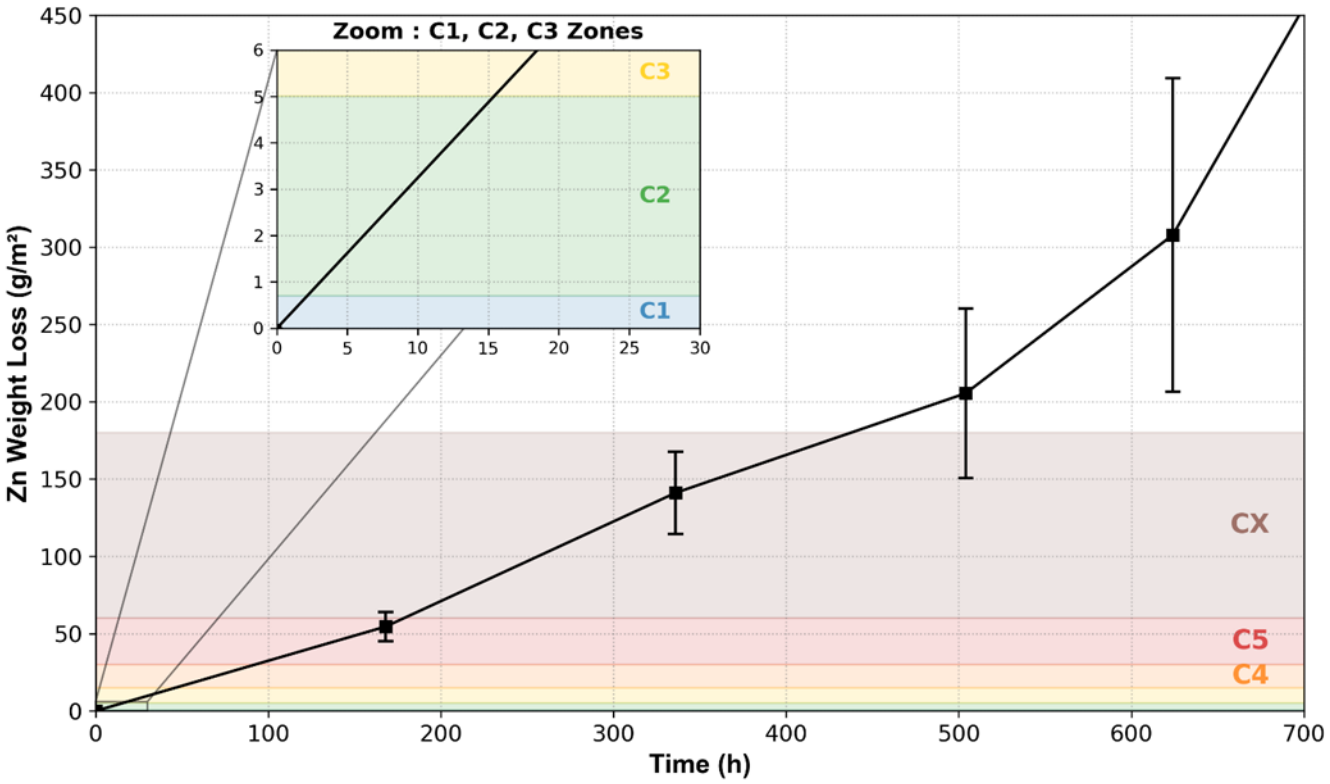

Figure 5-32. Weight loss of zinc (g/m^2) as a function of exposure time (h), indexed against ISO 9223 corrosivity categories (C1 through CX) with an inset detail highlighting the interpolated initial mass loss within the C1, C2, and C3 zones.

5.7.4 Temporal Analysis of Corrosivity Zone Transitions Based on Carbon Steel and Zinc Mass Loss Measurements

Table 6-4 summarizes the elapsed exposure time required for carbon steel and zinc specimens to transition between the ISO 9223 corrosivity categories under the GMW14872 protocol. This data provides a quantitative measure of the laboratory's acceleration factor and serves as the temporal baseline for site-specific corrosivity modeling.

The transition times highlight the aggressive nature of the cyclic exposure, with both materials exiting the "Low" corrosivity categories (C1 and C2) in under five hours. The data reveals a significant difference in how quickly the standardized thresholds are reached for each metal:

- Carbon steel progression: Carbon steel takes over three times longer (584.4 hours) than zinc to reach the CX zone. However, in absolute terms, achieving an "Extreme" classification in less than 25 days, a transition that may require years of outdoor exposure, demonstrates a massive acceleration factor.

- Zinc sensitivity: Zinc reaches the CX (Extreme) threshold in only 178.6 hours (approximately 7.4 days). This rapid progression through the ISO categories suggests that the GMW14872 environment is exceptionally severe for zinc, even though the salt load used in this test was low.

Table 5-4. ISO 9223 corrosivity zone entry times for steel and zinc based on weight loss measurements.

ISO 9223 Zone	Steel Entry Time (h)	Zinc Entry Time (h)
C1	0	0
C2	4.6	2.2
C3	92.7	15.4
C4	182.6	46.2
C5	279.6	92.4
CX	584.4	178.6

5.7.5 Analysis of Steel Thickness Loss Using Calibration Panels

As shown in **Figure 6-33**, the steel calibration panels exhibit a rapid and predominantly linear reduction in thickness during the initial phases of the test. Similar to the weight loss results (**Figure 6-31**), the panels surpass the C2, C3, and C4 thresholds within the first 300 hours. By the conclusion of the test at approximately 1250 hours, the total thickness loss reaches approximately 270 μm. This final measurement places the panels deep within the CX (Extreme) corrosivity zone. The sustained slope of the curve indicates that the corrosion products formed on these panels offer no efficient barrier protection, leading to a continuous and predictable thinning of the substrate. The error bars increase as the panels enter and progress through the CX zone.

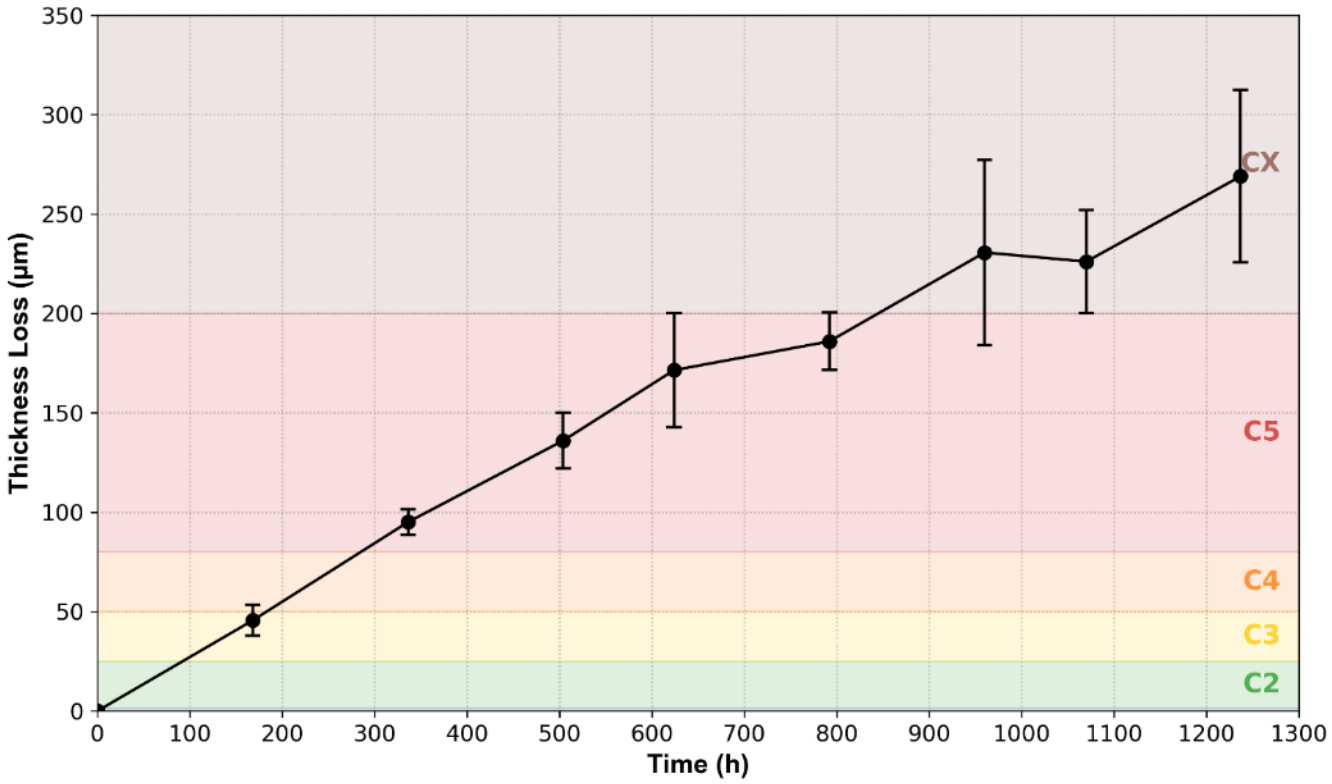

Figure 5-33. Global thickness loss (µm) of calibration steel panels mapped against ISO 9223 categories.

To isolate the initial degradation rate, **Figure 6-34** presents a linear fit of the first four experimental data points for the curve shown in **Figure 6-33**. As can be seen, these panels exhibit a rapid and predominantly linear reduction in thickness during the initial phases of the test.

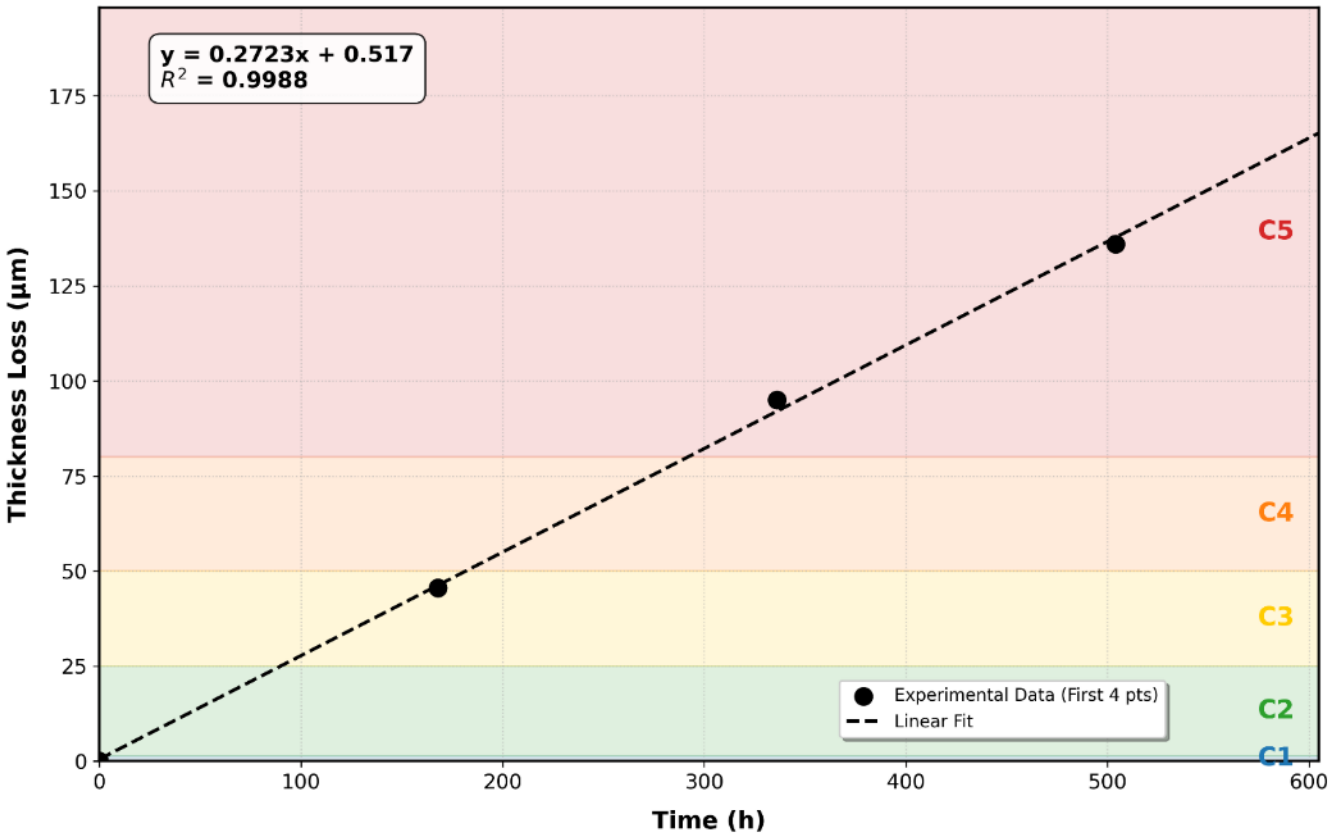

Figure 5-34. Global thickness loss (µm) of steel calibration panels mapped against ISO 9223 categories. The linear fit (TL (µm) = 0.2723t (h) + 0.517) across the first four data points of the graph shown in Figure 6-33.

5.7.6 Comparative Analysis of ISO 9223 Entry Times for Steel: Thickness Loss vs. Weight Loss Specimens

Table 6-5 summarizes the exposure durations required for steel calibration panels and weight loss specimens to reach various ISO 9223 corrosivity categories. These “entry times”, derived from physical thickness loss and the weight loss specimens, reveal a strong correlation during the initial phases of exposure. The transition through the C2 to C5 categories shows a variance of less than five hours, suggesting that mass loss and physical thinning progress at highly predictable and reproducible rates under moderate corrosion conditions. This close alignment between the two independent measurement types further validates the deoxidation protocols employed for the WL specimens, confirming that the verified cleaning methods effectively removed corrosion products without attacking the base substrate. However, a significant discrepancy of 260.4 hours is observed at the CX (Extreme) entry point, a gap directly tied to the escalating stochastic nature of extreme corrosion and the corresponding high standard deviation values recorded for both specimen types during the latter half of the 8-week test.

Table 5-5. Comparison of ISO 9223 entry times in the different categories for steel weight loss and calibration panels.

ISO 9223 Zone	Calibration Thickness Loss Specimens (h)	Weight Loss Specimens (h)
C2	4.7	4.6
C3	91.1	92.7
C4	181.3	182.6
C5	283.8	279.6
CX	844.8	584.4

5.8 Characterization of Weathering Steel Corrosion Sensor Behavior Under GMW14872 Exposure

Building upon the established benchmarks for carbon steel and zinc, the study continued with an evaluation of how weathering steel (WS) behaves under the accelerated GMW14872 cyclic protocol. To produce **Figure 6-35**, the experimental setup utilized one sensor dedicated to generating a continuous thickness loss trend via automated resistance logging, while a series of identical sensors provided discrete thickness loss measurements at specific sampling intervals. The sensors reached a maximum thickness loss of roughly 350 μm by 800 hours. This calculation accounts for the symmetrical degradation occurring on all sensor faces, including the interface beneath the bond, as will be demonstrated in the following sections.

Figure 6-35, which illustrates the performance of the weathering steel TLS under GMW14872 exposure, reveals a distinct two-stage kinetic profile prior to sensor saturation. During the initial induction phase (0 to ~200 hours), a relatively slow rate of thickness loss is observed, likely attributed to the time required for the chloride-rich electrolyte to penetrate native oxides and establish active electrochemical paths. Beyond this threshold, the sensor transitions into a predominantly linear regime that persists until approximately 700 hours, reaching a thickness loss of 250 μm. The discrete measurements follow the continuous curve closely until the end of the C5 region (200 μm), validating the sensor's precision during steady-state growth. However, upon entering the CX region, the discrete points exhibit significant scattering and deviation from the continuous trend; this behavior is driven by the stochastic nature of extreme corrosion, where localized surface variations and non-uniform oxide development dominate the kinetics before the sensor reaches its saturation limit at approximately 800 hours.

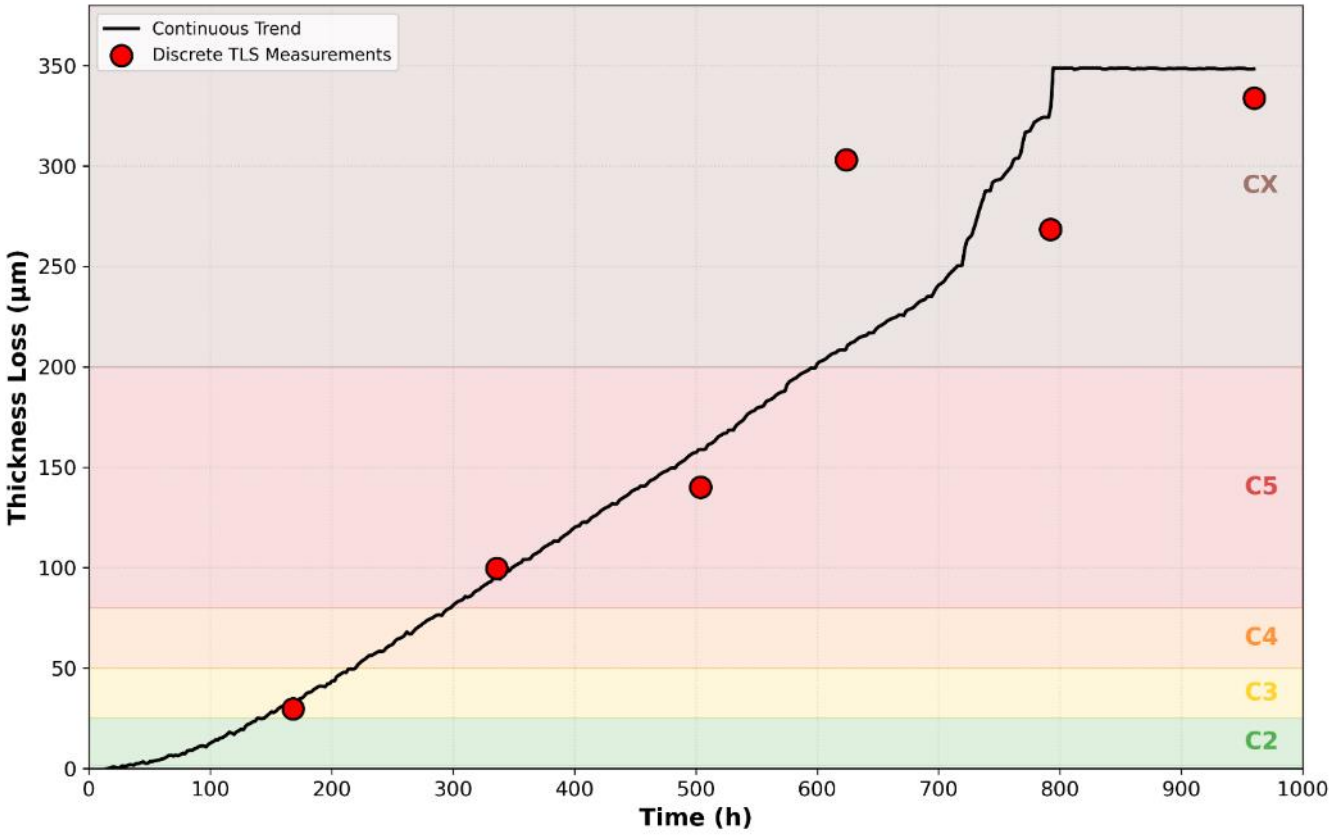

Figure 5-35. Comparison between continuous thickness loss trends (µm) and discrete sensor measurements for weathering steel over time (h), indexed against ISO 9223 atmospheric corrosivity categories from C2 to CX as they are defined for carbon steel.

The comparative analysis of entry times into the ISO 9223 corrosivity zones for carbon steel and weathering steel, presented in **Table 6-6**, reveals a significant kinetic delay in the WS sensor during the early stages of exposure compared to the carbon steel calibration panels. Specifically, the WS sensor takes nearly six times longer to exit the C2 zone (27.2 h vs. 4.7 h) and significantly lags through the C3 and C4 thresholds. This delay can tentatively be explained by the presence of alloying elements (such as Cr, Cu, and Ni) in the weathering steel, which facilitate a more robust native passive film that requires a longer induction period to break down under the chloride-containing GMW14872 cycles. However, as the environment transitions into the more aggressive C5, the gap narrows considerably. This late-stage acceleration suggests that once the initial passive film is compromised under chloride-rich and moisture conditions, the weathering steel undergoes a rapid thickness loss.

Table 5-6. Comparative analysis of ISO 9223 corrosivity zone entry times (as described for carbon steel) for carbon steel calibration panels versus weathering steel (WS) sensors.

ISO 9223 Zone	TL Threshold (μm)	Entry time, Calibration steel panels (h)	Entry time, Weathering Steel TLS (h)
C2	1.3	4.7	27.2
C3	25	91.1	138.7
C4	50	181.3	219.7
C5	80	283.8	297.8
CX	200	844.8	598.8

In **Figure 6-36**, to mathematically characterize the transition from surface stabilization to active degradation, a hybrid dual power law model was applied to the weathering steel TLS data. The initial incubation phase (Regime 1: 0-160 h) is defined by the equation $TL = 0.00172 \cdot t^{1.936}$, where the exponent of approximately 1.94 describes the accelerating breakdown of the native passive film as active corrosion sites are established.

Following a seamless transition at 160 h, the sensor enters a steady-state regime (Regime 2: 160-650 h) governed by $TL = 0.231 \cdot (t - 160)^{1.082} + 31.9$. The shift to a near-unitary exponent (1.082) confirms a linearized kinetic profile, indicating that the material is undergoing a sustained reduction in thickness at a constant rate.

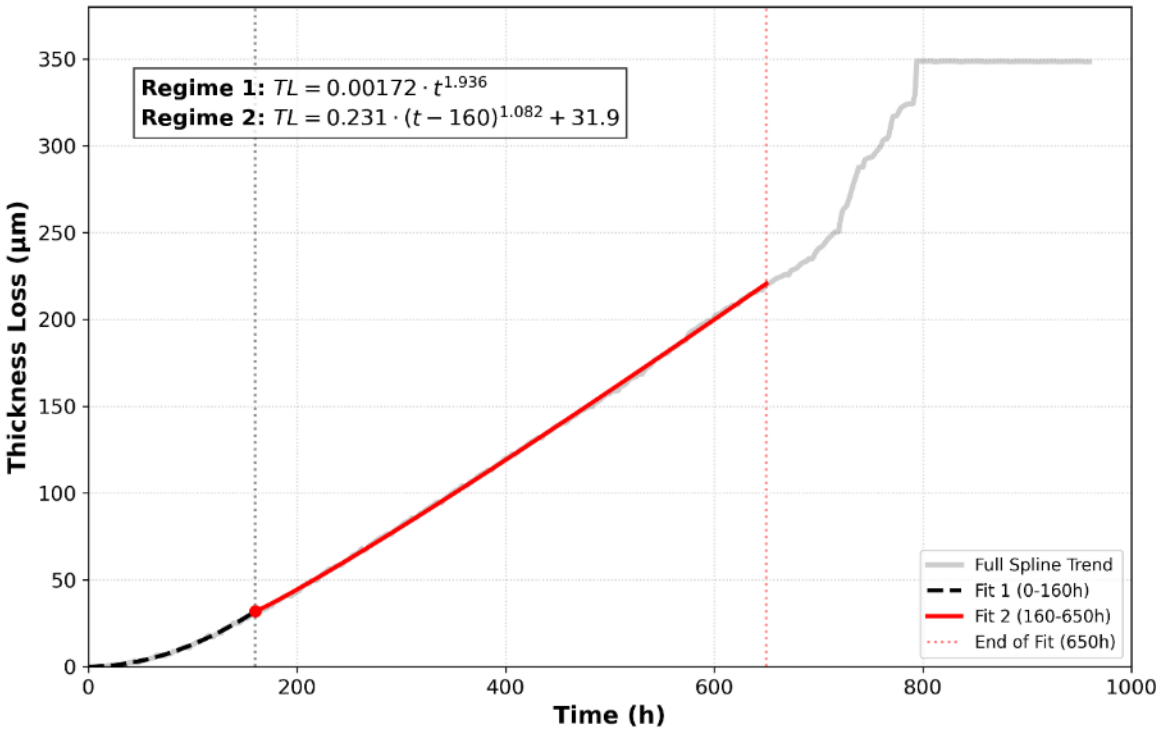

Figure 5-36. Hybrid dual power law model applied to the thickness loss (µm) of weathering steel over time (h), featuring a seamless transition at 160 hours between the initial induction phase (Regime 1) and the stabilized propagation phase (Regime 2).

5.9 Comparative Evaluation of Bridge Micro-Climates: Analysis of Data Obtained from Remote Monitoring Using TLS, ToW, and Galvanic Sensors

The evaluation of the infrastructure's structural health begins with a high-level review of the real-time data obtained via remote access from the various instrumentation suites deployed across multiple strategic positions on the bridge. This sensor network, comprising thickness loss sensors (TLS), Time of Wetness (ToW) leafs, and galvanic couples, was specifically designed to capture localized corrosion rates. By analyzing these data streams in parallel, it is possible to characterize the distinct micro-climates formed by structural geometry, traffic-induced salt spray, and varying exposure to natural washing.

The primary objective of this global assessment is to determine how spatial orientation and height above the roadway, or away from it on left or right sides, dictate the onset and rate of corrosion. Unlike the uniform conditions of a laboratory chamber, the bridge environment presents stochastic triggers, where brief spikes in galvanic activity often correlate with specific

ToW events or de-icing salt applications. This section details the comparative performance of these sensors across the structure, providing the necessary context to understand why certain locations progress through the ISO 9223 corrosivity zones more rapidly than others. This positional analysis ultimately serves to bridge the gap between the controlled kinetic models established in the laboratory and the heterogeneous reality of the bridge's service environment.

5.9.1 Temperature, Relative Humidity, and Time of Wetness Conditions

The atmospheric conditions at the Hwy 401 Underpass at County Road 2 & County Road 34 I/C bridge site were monitored continuously since the beginning of exposure. Between November 25, 2024, and November 25, 2025, i.e., during the Year-1 exposure, the site experienced an average temperature of 8.3°C and an average relative humidity (RH) of 70.5%. As illustrated in the daily time-series and monthly average profiles (**Figures 6-37** and **6-38**), the environment exhibits significant seasonal volatility; temperatures ranged from summer peaks exceeding 30°C to winter lows dropping below -20°C. The relative humidity remained consistently high throughout the year, frequently peaking near 100%. Notably, the monthly analysis reveals that the highest average humidity levels occur during the winter months (December to February), coinciding with the period of greatest de-icing salt application.

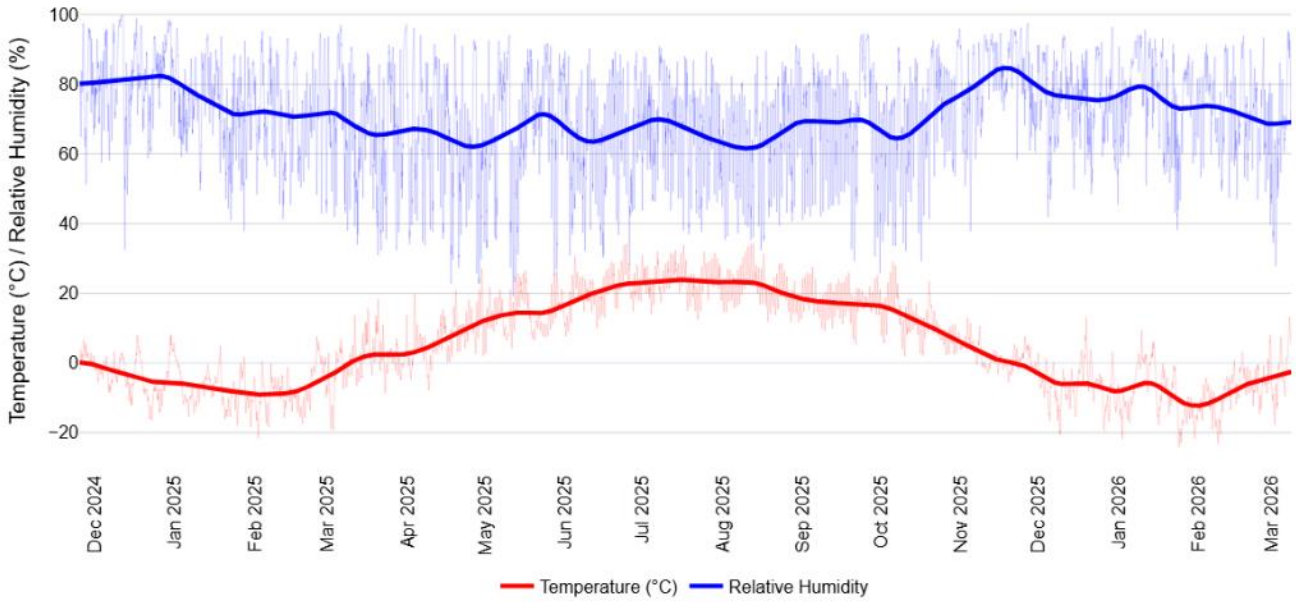

Figure 5-37. Daily temperature and relative humidity profiles at the Lancaster bridge (November 21, 2024 to March 8, 2026).

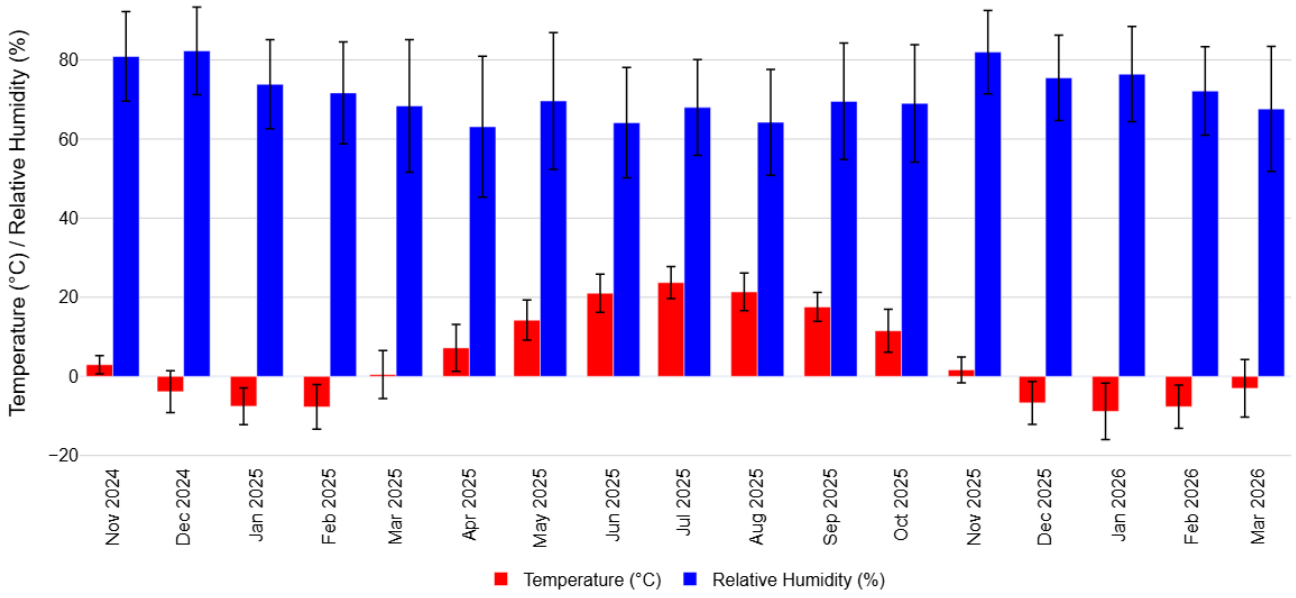

Figure 5-38. Monthly mean temperature and relative humidity with associated standard deviations.

The ToW profiles, presented in **Figure 6-39**, show a clear intensification of surface wetness during the winter months (December through March), characterized by high-frequency voltage spikes exceeding 1000 mV. These periods of peak wetness correlate with de-icing salt applications and roadway spray, which create a highly conductive electrolyte on the sensor surfaces. In contrast, the summer months (June through August) exhibit significantly lower activity, with the base signal stabilizing near 300-400 mV, representing a period of relative dryness.

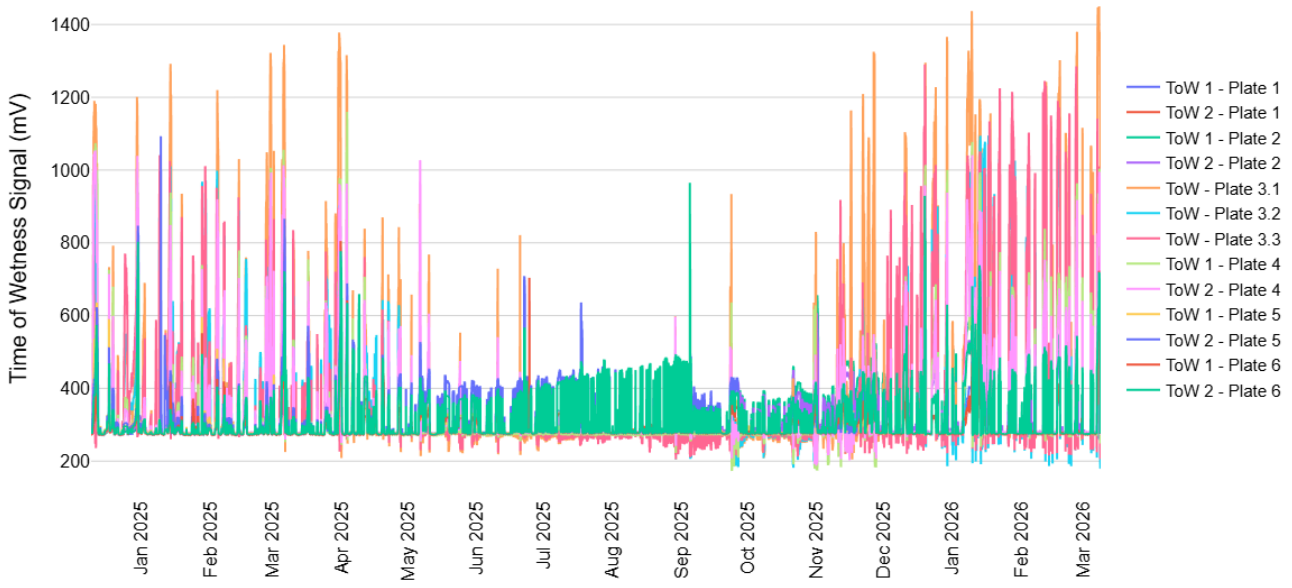

Figure 5-39. Profiles of ToW voltage signals (mV) recorded across the bridge sensor network from December 2024 to March 2026, illustrating the seasonal frequency and intensity of moisture events at the monitored structural positions.

While the seasonal analysis characterizes the temporal cycles of the environment, the average cumulative ToW per plate provides a quantitative measure of the total "corrosive dose" delivered to specific bridge locations during the first year of in-field exposure (as of November 24, 2025). This integrated metric maps the structural micro-climates and reveals a distinct gradient of environmental aggressiveness across the infrastructure. As seen in **Figure 6-40**, Plate 3.1 emerges as the most severely exposed location with a cumulative total of 17.6M mV, identifying it as a high-velocity splash zone or a region of poor drainage where electrolytes persist. In contrast, Plate 1 exhibits the lowest cumulative exposure at 14.7M mV, representing a drier baseline that may more readily facilitate the formation of a stable, protective patina.

Based on these cumulative ToW values, Plate 3.1 (See Section 5.5.2 and Figure 6-16 for the location of plates) is anticipated to exhibit the highest corrosion rates, likely trending toward the extreme corrosivity categories established in laboratory modeling. Conversely, the lower cumulative dose of Plate 1 suggests a significantly reduced corrosion rate, while the moderate values for Plate 5 (15.7M mV) and Plate 6 (15.6M mV) reflect a micro-climate characterized by fluctuating exposure events. This quantitative mapping provides the essential environmental context required to interpret the divergent corrosion behaviors and sensor responses observed across the different metallic substrates.

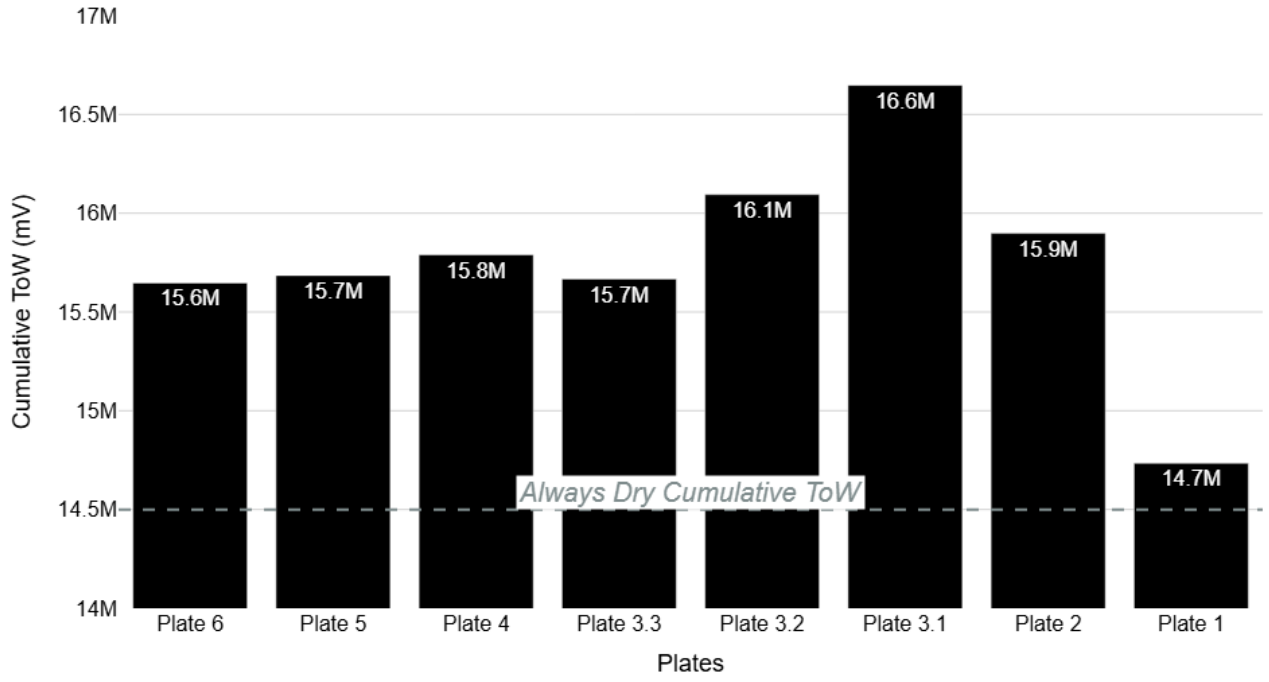

Figure 5-40. 12-month cumulative ToW voltage signals (mV) across eight monitored bridge positions, quantified as of November 24, 2025. The dashed grey line defines the theoretical baseline for a 100% dry sensor, providing a visual reference to distinguish baseline sensor noise from significant wetting events.

5.9.2 Galvanic Current Measurements Across the Bridge Infrastructure

To further evaluate the electrochemical activity driven by these bridge micro-climates, galvanic currents were monitored across the sensor network. **Figure 6-41** represents a typical example of the galvanic activity recorded across the bridge, specifically monitoring the interaction between Weathering Steel (WS) and Carbon Fiber Reinforced Polymer (CFRP).

The electrochemical data highlights a pronounced seasonal periodicity in galvanic activity, where winter peak currents frequently reaching between 0.25 mA and 0.35 mA (December to April) indicating the presence of a highly conductive electrolyte, likely a concentrated brine from de-icing salts, that bridges the WS-CFRP couple and triggers the corrosion process. This behavior is followed by a low-current period during summer, from June through September, during which galvanic currents drop to near-zero levels as the drier and salt-free environment inhibits the electrochemical circuit. Crucially, this curve represents a typical example of the system-wide consistency observed across the bridge, as other galvanic couples in the distributed sensor network demonstrate the same seasonal variability; while specific peak magnitudes vary by position, the "on/off" switching of the electrochemical cells remains synchronized with these bridge-wide climatic cycles.

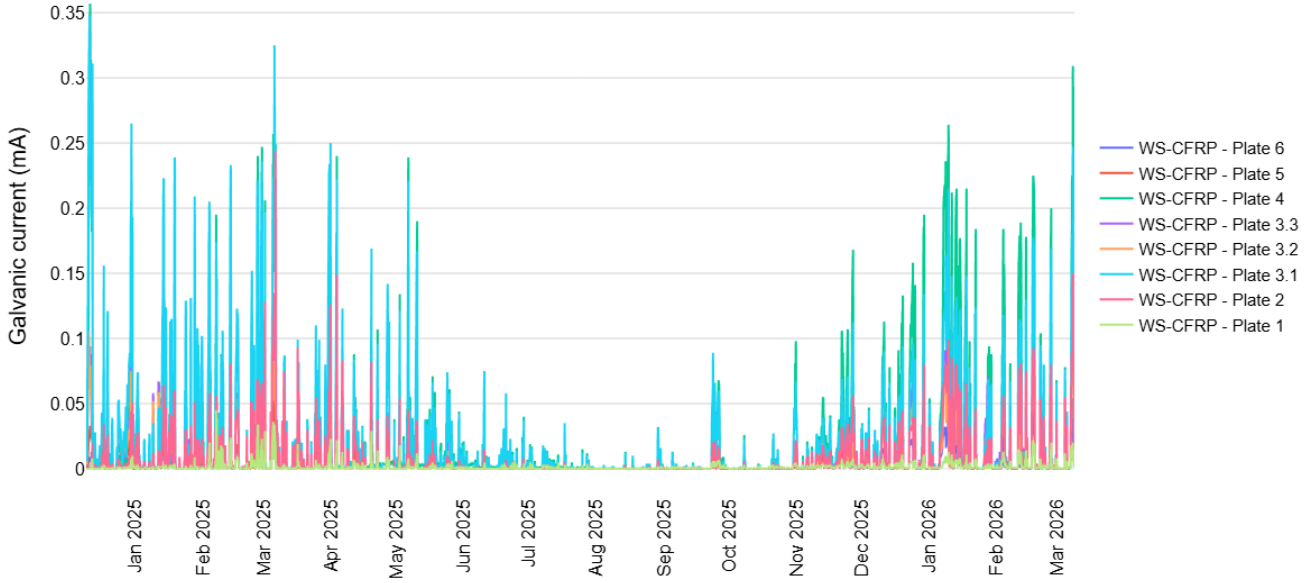

Figure 5-41. Profiles of galvanic current (mA) recorded for the weathering steel / carbon fiber reinforced polymer (WS-CFRP) assembly across eight positions from November 2024 to March 2026.

To provide a comprehensive overview of the comparative corrosion behaviors across the infrastructure, the monthly average galvanic current, presented in **Figure 6-42**, serves as a definitive indicator of the sustained corrosion levels experienced at different bridge positions. Although the entire sensor network responds to the same macro-climatic oscillations, alternating between active winter and passive summer states, a significant disparity in environmental aggressiveness is observed at the different positions on the bridge. Plate 4 and Plate 3.1 consistently maintain the highest average current densities, peaking near 0.05 mA during the winter of 2026, which confirms these zones are subject to the most persistent electrolyte contact and chloride accumulation. In the mid-range, Plates 2, 3.2, and 3.3 demonstrate a moderate but steady increase in activity as the second winter progresses, with averages climbing toward 0.02 mA. In contrast, the muted responses from Plate 5 and Plate 6, and especially Plate 1 (which remains below 0.005 mA), confirm significantly less corrosive micro-climates. By averaging these stochastic environmental triggers, the monthly variations reveal that the magnitude of the cumulative attack varies by nearly an order of magnitude across the structure (i.e., 0.005 vs. 0.05 mA).

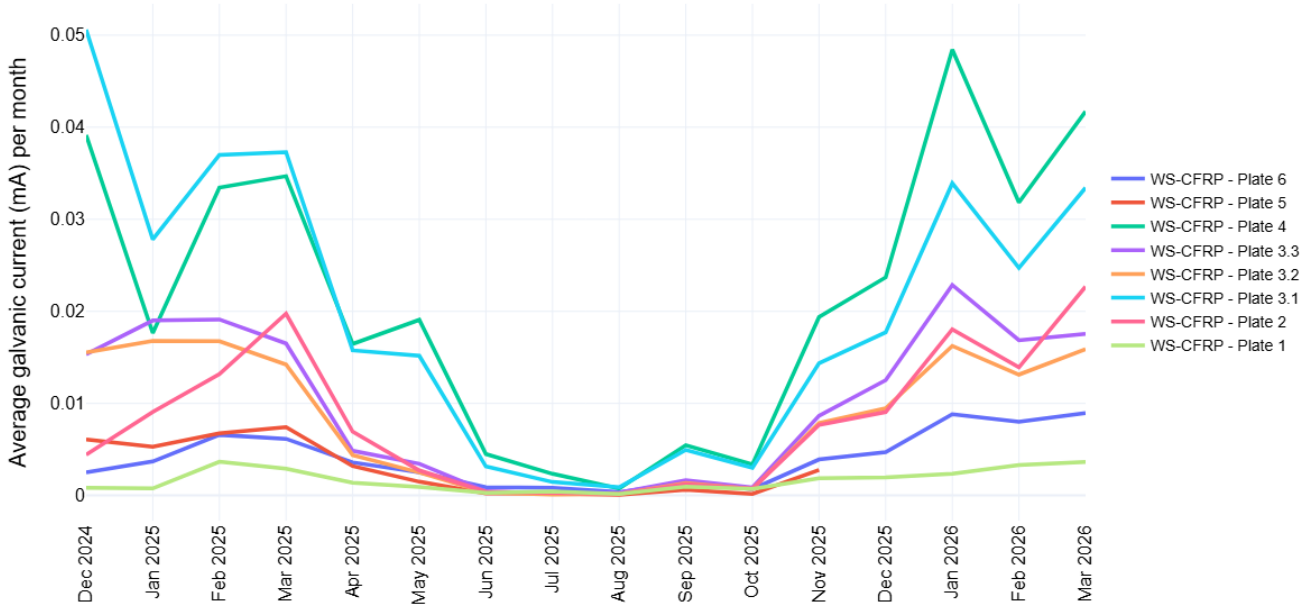

Figure 5-42. Average monthly galvanic current (mA) for the weathering steel and carbon-fiber-reinforced polymer (WS-CFRP) couples across eight structural positions from December 2024 to March 2026.

The interpretation of the environmental drivers and monthly averages is further substantiated by the cumulative charge over time. The total cumulative charge (Q), measured in Coulombs (C), is obtained by integrating the recorded galvanic current (I) over the total exposure time (t). Mathematically, the total charge (Q) is defined by the following integral:

$$Q = \int_{t0}^{t} I(t)dt \qquad (6\text{-}1)$$

This integrated metric allows for a direct comparison across different material couples, including CFRP-AA6022, WS-AA6061, WS-CFRP, and the WS1.18-WS2.0 galvanic sensors.

The cumulative charge curves presented in **Figure 6-43** reveal a "staircase" kinetic profile that confirms the high-intensity winter cycles (2025 and 2026) are responsible for the vast majority of material degradation. While the CFRP-AA6022 and WS-AA6061 couples exhibit the highest total magnitudes, reaching between 1750 C and 2500 C at the most aggressive locations, the WS-CFRP couples show a proportional but lower-magnitude response, peaking near 750 C. The WS1.18-WS2.0 sensors, which represent an almost similar-metal (weathering steel to weathering steel) macro-cell, exhibit an overall cumulative charge that is orders of magnitude lower than the dissimilar metal couples, peaking at just under 100 C. Despite these differing scales, the positional ranking remains remarkably consistent across all four material systems, revealing a clear structural gradient of corrosivity. Plate 4 and Plate 3.1, which are facing down over the #1 left lane and #2 middle lane respectively, are repeatedly identified as the most

aggressive micro-climates. These are followed by an upper-intermediate tier comprising Plates 3.3 & 3.2 (both vertical over the #2 (middle) lane), and 2 (facing down over the acceleration lane), which exhibit moderate-to-high cumulative totals reflective of their localized, yet slightly less persistent, exposure to active splash zones. Conversely, Plates 5 and 6 (vertical on the piers) demonstrate a significantly more reduced electrochemical response across all material pairings, positioning them within a moderately benign environmental envelope, while Plate 1 (on the abutment wall) consistently defines the absolute lower boundary of baseline activity. This multi-material synchronization demonstrates that the bridge micro-climates dictate the corrosion kinetics regardless of the specific galvanic couple

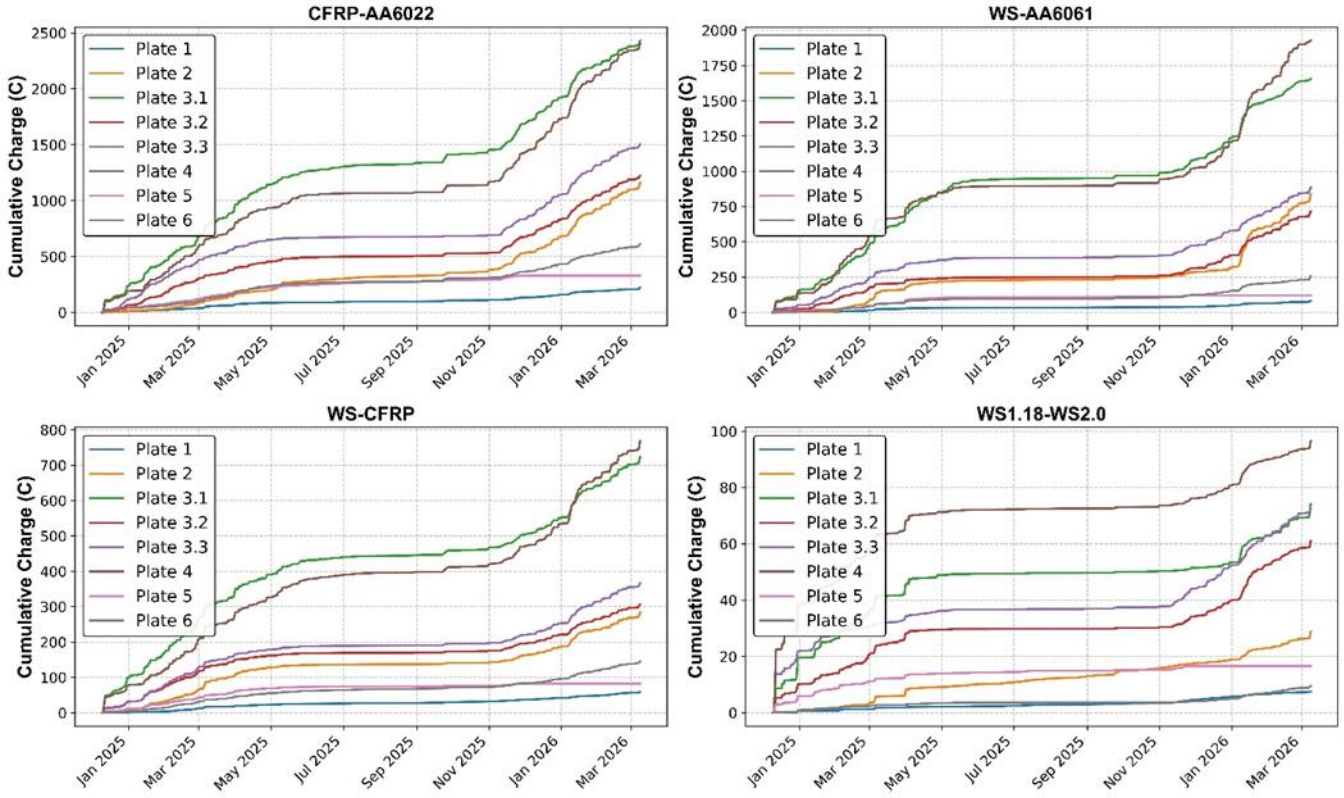

Figure 5-43. Cumulative electrical charge (C) over a 15-month exposure period for four distinct galvanic assemblies (CFRP-AA6022, WS-AA6061, WS-CFRP, and WS1.18-WS2.0) distributed across eight monitored micro-climates.

A critical insight from the heatmap presented in **Figure 6-44** lies in the contrast between the highly consistent proportional relationships of the dissimilar-metal couples (evidenced by the uniform dark blue bands in the lower rows) and the significant spatial variability observed when comparing against the similar-metal baseline. While the intrinsic galvanic relationships between the robust, high-current couples (e.g., CFRP-AA6022 and WS-AA6061) remain remarkably stable regardless of the overall environmental severity at a given position, the WS1.18-WS2.0 macro-cell demonstrates significantly less reproducible behavior across the infrastructure. This erratic spatial variance is likely an inherent consequence of the extremely

low galvanic driving force associated with pairing almost identical weathering steel alloys; the resulting micro-ampere currents are highly susceptible to localized stochastic noise, making the baseline couple inherently noisier and less reliable for comparative spatial mapping than the dominant signals of the dissimilar couples.

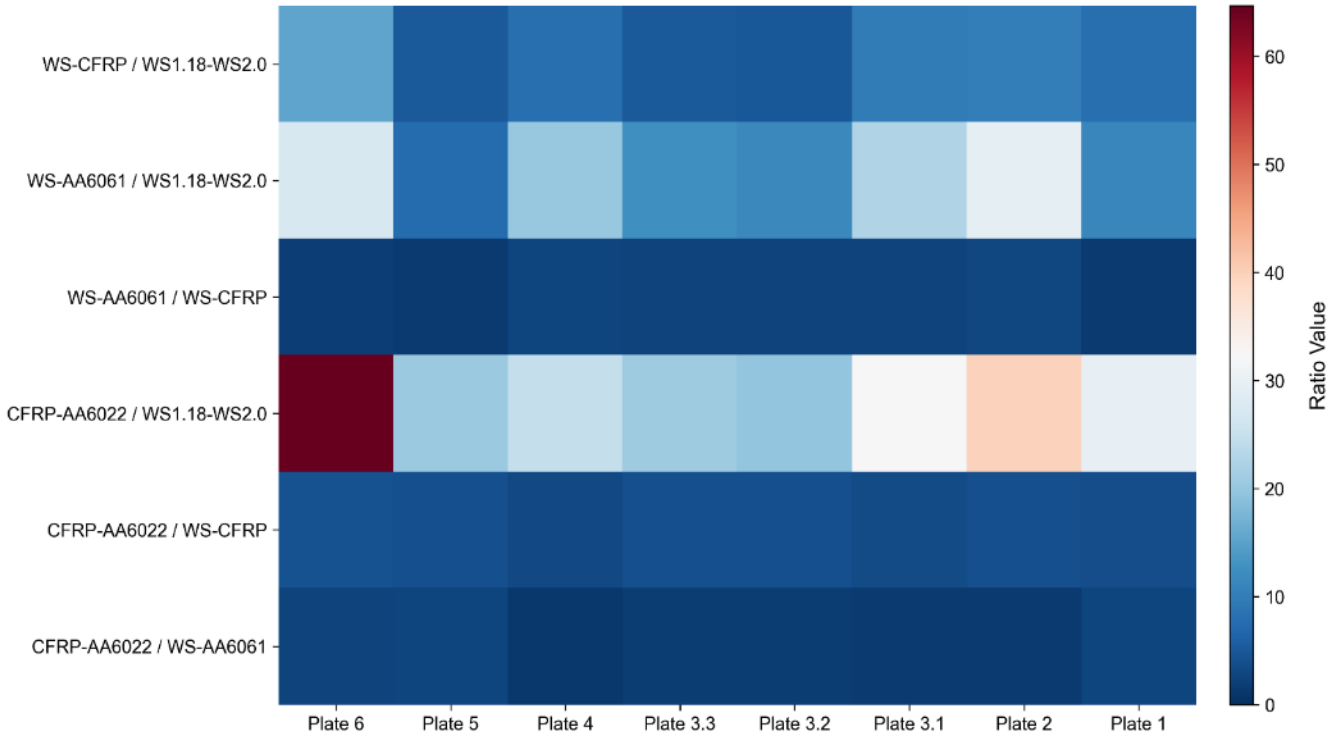

Figure 5-44. Matrix illustrating the calculated ratios of cumulative galvanic current for six distinct material pairing comparisons distributed across the respective structural coordinates of the bridge sensor network.

While the integration of galvanic current into cumulative charge provides a robust, high-resolution map of environmental aggressiveness, this electrochemical metric primarily quantifies the driving force specific to dissimilar material couples. However, because the oxygen reduction reaction (ORR) acts as the rate-controlling step for atmospheric corrosion, regardless of whether a metal is galvanically coupled or freely corroding, this charge may serve as a universal proxy for environmental severity. Consequently, it is anticipated that these cumulative galvanic charges will strongly correlate with the thickness loss calculated from the weathering steel (WS) sensors signals.

5.9.3 Weathering Steel Thickness Loss Sensors

To validate the environmental aggressiveness mapped by the galvanic specimens, the analysis now shifts to the results provided by the connected thickness loss sensors (TLS) made of

weathering steel. **Figure 6-45** reveals a cumulative thickness loss trajectory that strikingly mirrors the established positional rankings using the galvanic couples. As predicted by the cumulative galvanic charge data, sensors on Plate 3.1 and Plate 4 endure the most severe degradation, accumulating thickness losses of approximately 107 µm and 94 µm, respectively, after 15 months of exposure. Conversely, the almost sheltered Plate 1 consistently defines the lower boundary of atmospheric attack, stabilizing near 30 µm. Between these structural extremes lies a tightly clustered intermediate tier comprising Plates 2, 3.2, 3.3, 5, and 6, which collectively reach a cumulative thickness loss between 55 µm and 70 µm, suggesting a shared, moderate micro-climate that lacks the extreme, persistent wetness of the primary splash zones.

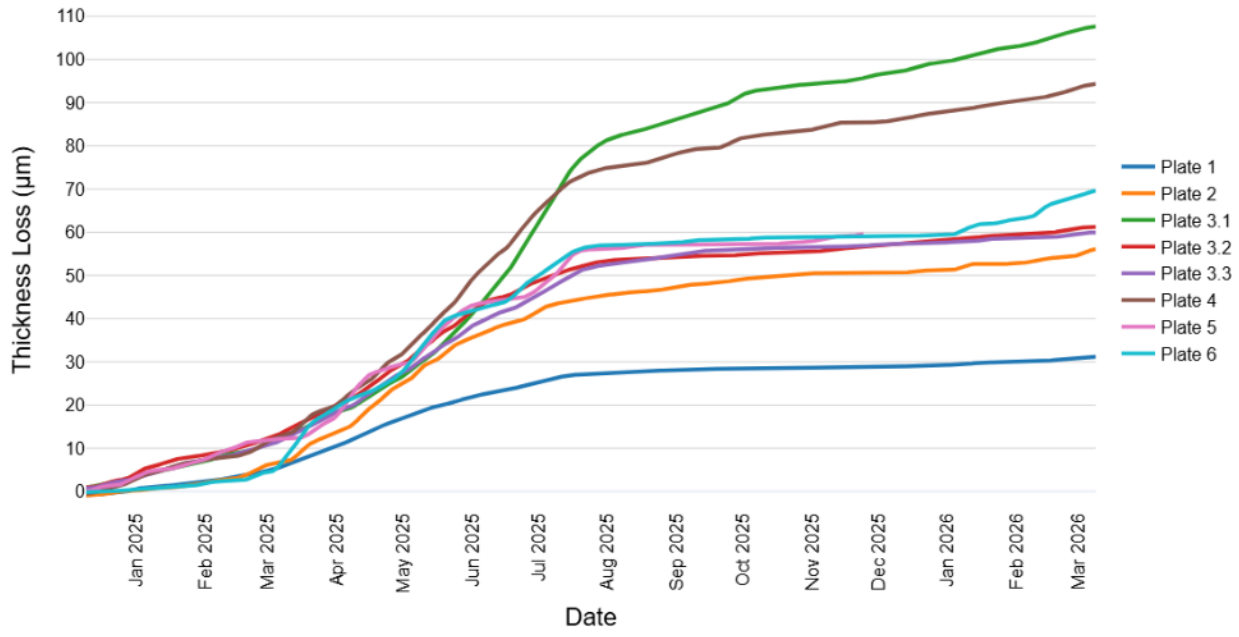

Figure 5-45. Cumulative thickness loss (µm) of weathering steel recorded by thickness loss sensors (TLS) across eight distinct bridge positions over a 15-month exposure period from December 2024 to March 2026.

Figure 6-46 presents the calculated thickness loss (µm) for the first 12 months of monitoring of WS TLS plotted against the cumulative galvanic charge (Q) for all four materials combinations. The resulting scatter plots demonstrate a robust linear relationship between these two metrics across all structural micro-climates, with the dissimilar-metal couples (CFRP-AA6022, WS-AA6061, and WS-CFRP) yielding exceptionally high coefficients of correlation (R^2 between 0.96 and 0.99). While the primary splash zones and abutment wall positions fall tightly along the regression lines, Plates 5 and 6 consistently appear as outliers across all material pairings. The vertical orientation of these galvanic assemblies, installed in a low splash zone, likely results in a thinner electrolyte film covering the surfaces, potentially increasing ohmic resistance within the local cell. This deviation, characterized by a higher WS thickness loss

than what is predicted by the galvanic coupling activities alone, suggests that in these more sheltered environments, the physical degradation of the weathering steel may be driven by localized moisture retention mechanisms that are not fully captured by the instantaneous galvanic signal. This discrepancy highlights how drainage and reduced electrolyte thickness on vertical surfaces can decouple the measured galvanic currents response from thickness loss measurements. Finally, the significantly lower R^2 of 0.75 for the WS1.18-WS2.0 assembly highlights the inherent difficulty in using low-current, highly similar metal couples, for predictive mapping.

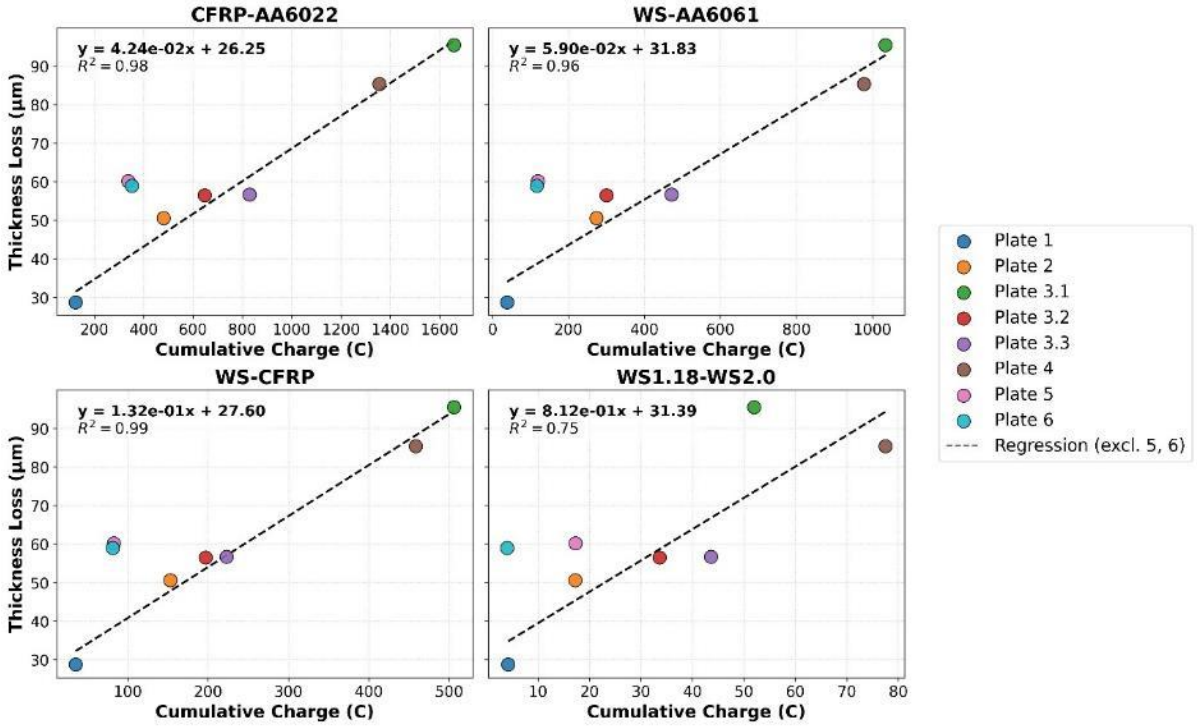

Figure 5-46. Correlation models between cumulative thickness loss (µm) and cumulative galvanic charge (C) for a 12-month exposure period. Linear regression models were calculated excluding Plates 5 and 6.

Figure 6-47 illustrates a 15-month temporal corrosion analysis (December 2024 to March 2026), revealing a distinct phase-shift between galvanic activity and bulk material loss. The uppermost panel shows that the cumulative thickness loss follows a sigmoidal trajectory with clear stratification; Plates 3.1 and 4 exhibit the most severe degradation, reaching approximately 100 µm and 90 µm, respectively, while Plate 1 remains a stable baseline at 30 µm. The derivative corrosion rates, presented in the secondary panel, confirm that most of the WS thickness loss occurs between April and September 2025, with Plate 3.1 peaking at over 250 µm/year due to heightened thermal kinetics. Conversely, as shown in the tertiary panel, the galvanic current exhibits a perfectly inverse seasonal trend, peaking during the winter and early spring. This behavior validates a winter "priming" mechanism where de-icing salts and

meltwater provide a thick, highly conductive electrolyte that maximizes galvanic drive and chemically conditions the WS surface, facilitating rapid thickness loss as soon as rising spring temperatures accelerate oxidation. This mechanism is further clarified by the performance of vertical Plates 5 and 6, where weathering steel loss continues despite negligible galvanic currents. This decoupling highlights the critical role of electrolyte thickness: while a bulk liquid layer is required to bridge dissimilar materials for a galvanic drive, the general atmospheric corrosion of the weathering steel is sustained by thin-film moisture, even when rapid drainage on vertical surfaces prevents the formation of a stable galvanic bridge.

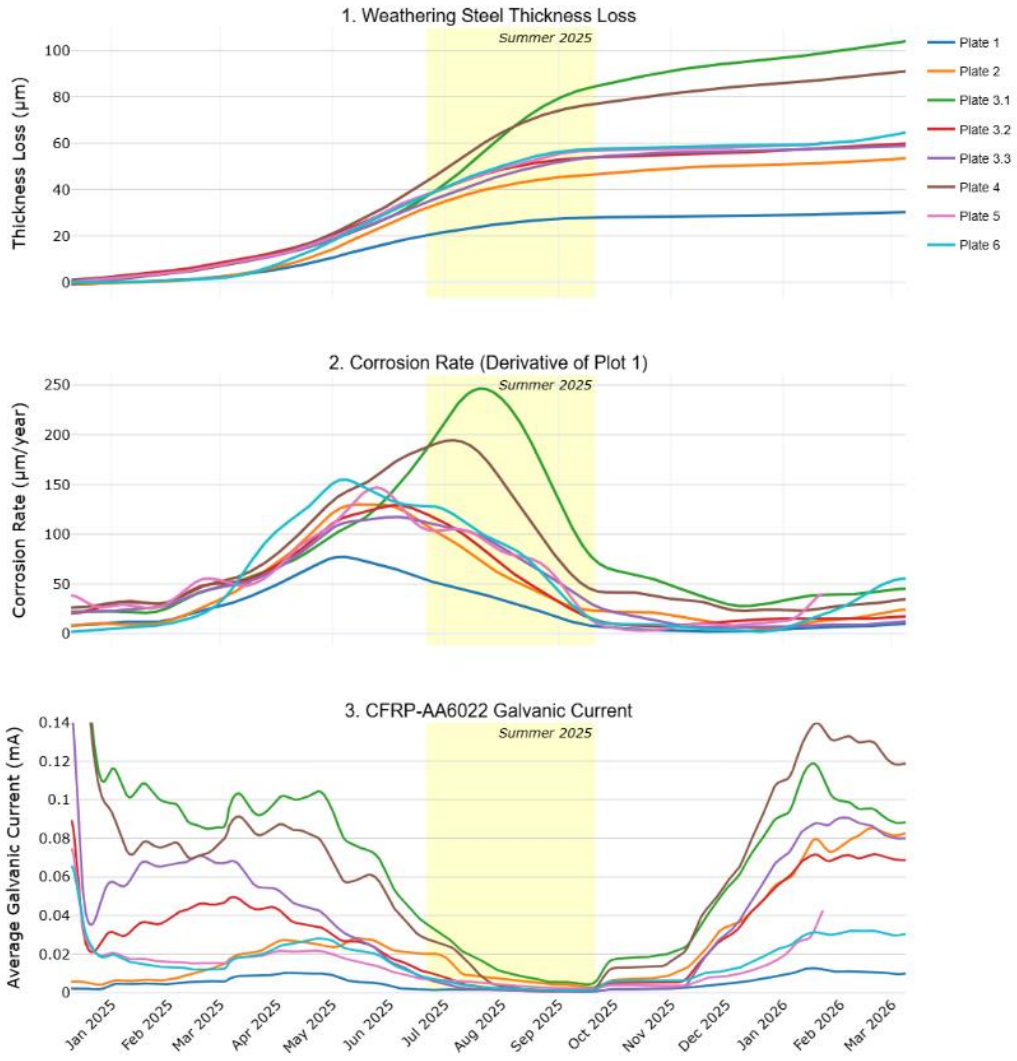

*Figure 5-47. Smoothed 2-month rolling mean time-series analysis comparing **(1)** cumulative calculated weathering steel thickness loss (µm), **(2)** the derived instantaneous corrosion rate (µm/yr), and **(3)** the galvanic current (mA) for the CFRP-AA6022 couples, across the eight different positions.*

Plates 3.1 and 4, which exhibited the highest corrosion rates across the monitoring network (see 2nd panel in **Figure 6-47**), were selected to evaluate the alignment of field data to

fundamental electrochemical principles during the late spring transition. In **Figure 6-48**, the linear relationship observed in the Arrhenius plots spanning the window from May 25 to June 24, 2025, confirms that the corrosion kinetics were strictly thermally activated and governed by a consistent rate-controlling step. The derived activation energy (E_a) values of 35.6 kJ/mol for Plate 3.1 and 14.6 kJ/mol for Plate 4 fall well within the established literature range of 10 to 60 kJ/mol for atmospheric steel corrosion [40].

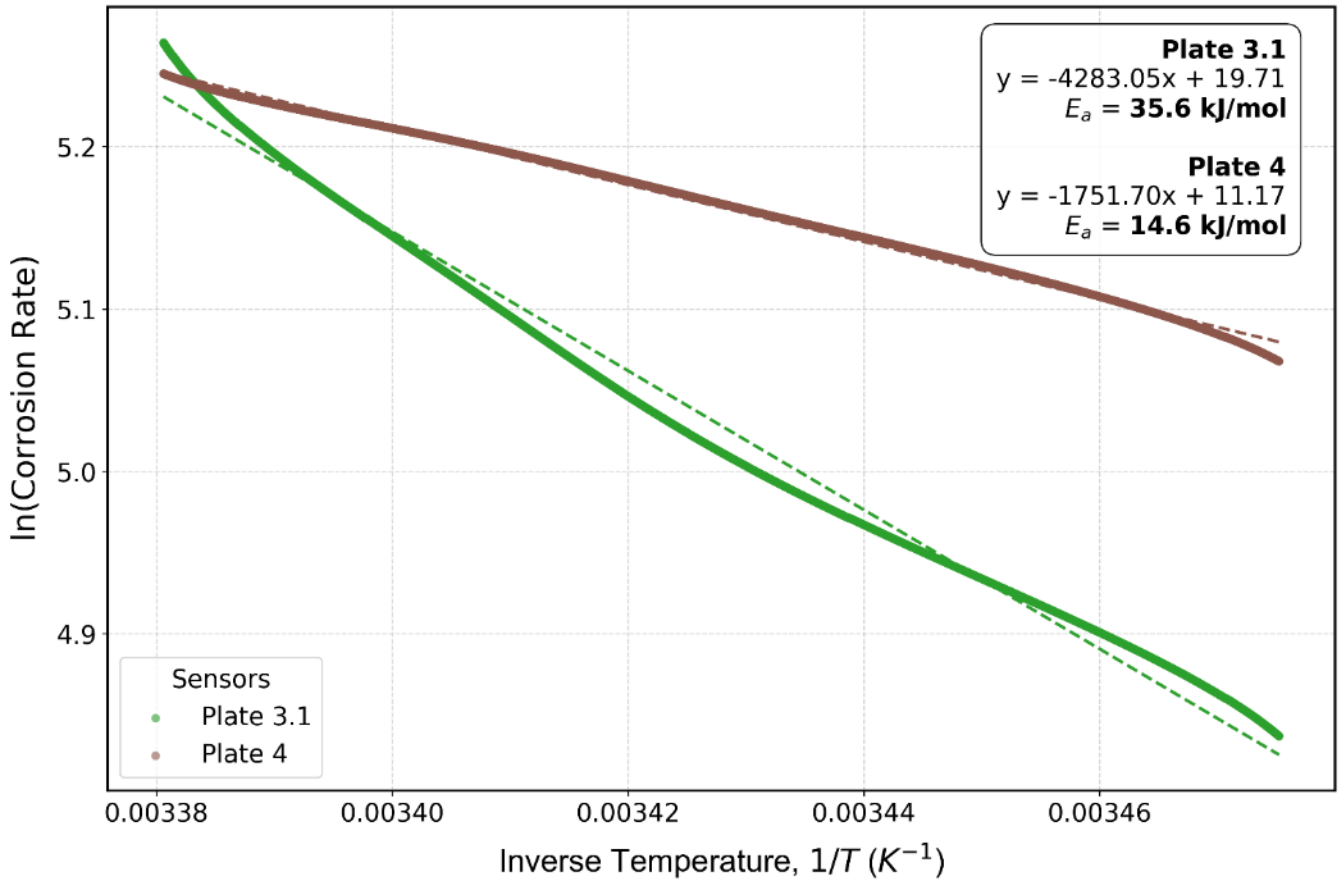

Figure 5-48. Arrhenius plots illustrating the relationship between the natural logarithm of the corrosion rate and inverse temperature (1/T) for Plates 3.1 and 4 during the late spring period (May 25 – June 24, 2026), demonstrating that the corrosion kinetics followed a predictable thermally activated path once freshwater conditions were established.

5.9.4 Systematic Evaluation of Plate 5 Specimens: 12-Month Bridge Site Exposure Results

Following the laboratory characterization of the WS thickness loss sensors (TLS) and steel calibration panels, a comprehensive post-mortem analysis was conducted on the specimens of Plate 5, shown in **Figure 6-49**, retrieved from the bridge. The primary objective was to

physically measure the actual thickness loss of the weathering steel and calibration steel panels after 12 months of deployment. This field data provides the "ground truth" required to validate the kinetic models established under GMW14872 exposure and to determine if the laboratory-observed transitions between ISO 9223 corrosivity zones can be correlated to the bridge's micro-climate. For instance, while laboratory results suggested an initial induction delay for weathering steel corrosion, the analysis of the decommissioned panel will reveal whether this passivating effect successfully develops in situ or if environmental conditions hinder the conservation or formation of a stable, protective patina.

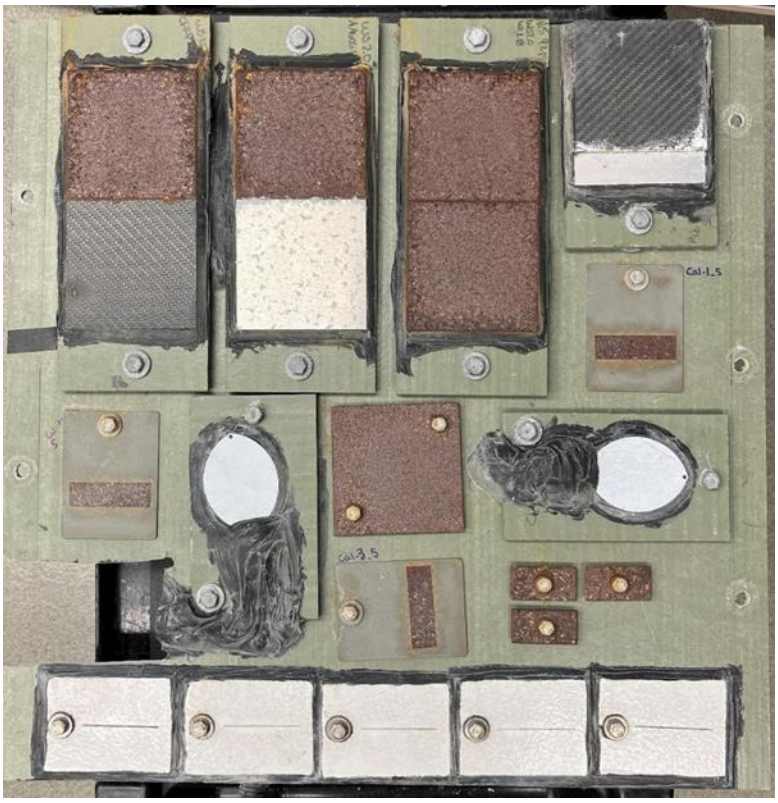

Figure 5-49. post-exposure photograph of the decommissioned Plate 5 following its 12-month in-field deployment. The assembly displays the diverse array of specimens used for "ground truth" sensor validation; note that the WS thickness loss sensor (TLS) was removed for immediate analysis prior to this documentation.

As a first step, the WS thickness loss sensor (TLS) from Panel 5 was subjected to cross-sectional metallographic analysis. This physical evaluation, illustrated in **Figure 6-50** micrographs, reveals the actual state of the material degradation after 12 months of in-field exposure. By comparing the pristine reference side (**Figure 6-50a**) with the typical corroded cross-section (**Figure 6-50b**), a distinct reduction in the sensor core is evident. Notably, the analysis shows that the metal was subjected to corrosion on all faces; despite being initially bonded to a supportive substrate, the ingress of moisture and corrosive species at the

interface allowed for significant “under-bond” degradation. This omnidirectional attack highlights the aggressive nature of the local micro-climate and provides the necessary physical baseline to calibrate the sensor’s cumulative thickness loss measurements presented in this report.

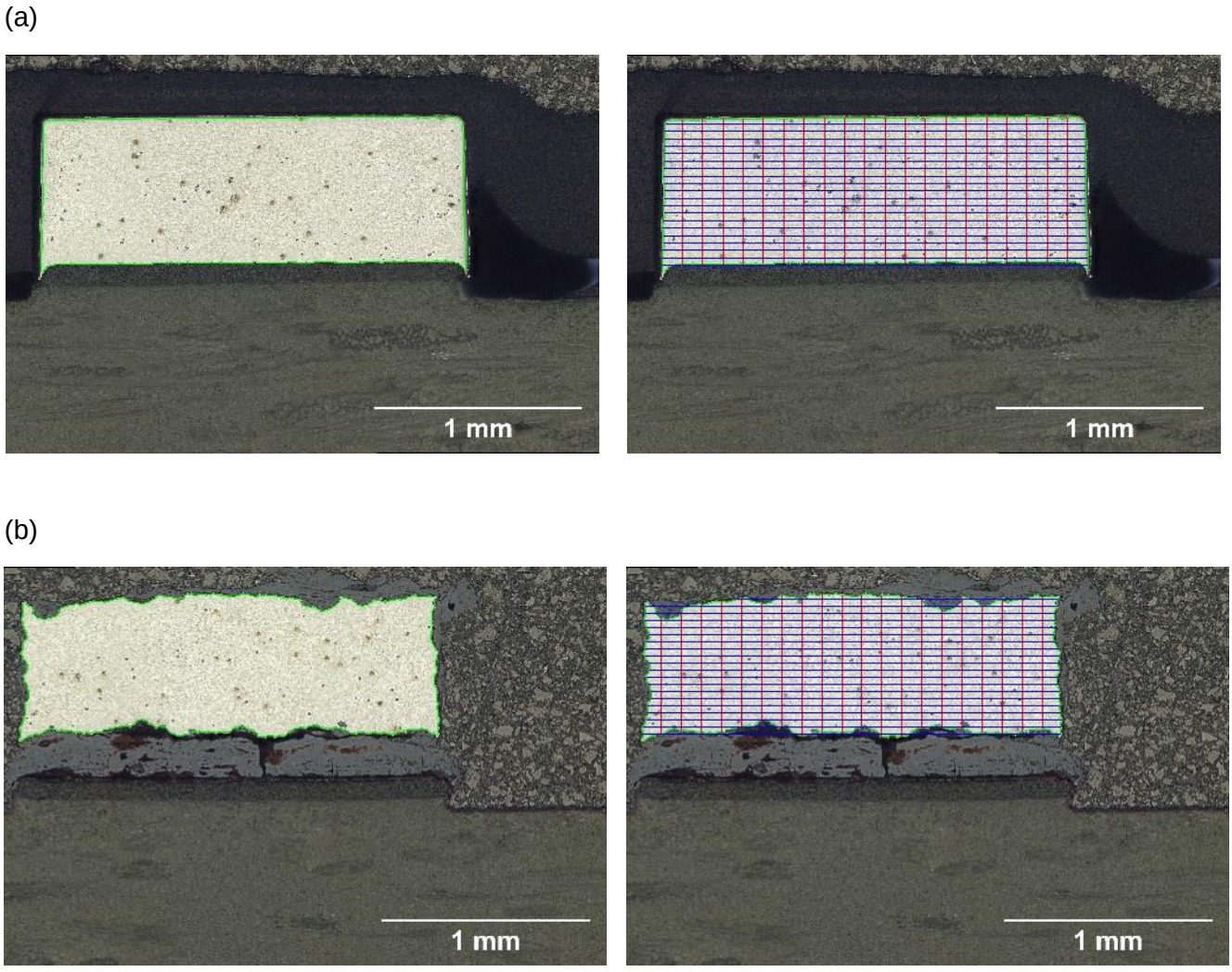

Figure 5-50. Cross-sectional metallographic analysis of the WS TLS from Panel 5: (a) typical image of the reference side showing the initial material integrity, and (b) typical image of the corroded section. The superimposed grid and green contours illustrate the digital quantification process used to assess the remaining metallic thickness and confirm that corrosion occurred around the entire perimeter of the specimen.

Table 6-7 summarizes the quantitative results derived from the digital image processing of the WS thickness loss sensor cross-sections by comparing the initial baseline dimensions to the measurements taken after 12 months of structural exposure. The data confirms a significant reduction in the metallic core, with the baseline average height measured at 0.7014 mm dropping to a corroded average of 0.6108 mm, representing a total height loss of 0.0906 mm (approximately 90.6 μm). Similarly, the width decreased from a baseline of 2.0479 mm to 1.9274 mm, indicating a lateral loss of 0.1204 mm (120.4 μm). A critical observation within the dataset is the sharp increase in the standard deviation for the corroded specimens; while the baseline height showed a minimal deviation of 0.0071 mm, the corroded height deviation rose to 0.0429 mm, reflecting the non-uniform, stochastic nature of the atmospheric attack.

Table 5-7. Quantitative dimensional analysis of the WS thickness loss sensor cross-sections from Panel 5, comparing the initial baseline state to the corroded metallic core after 12 months of structural exposure to determine total material recession (μm) and measurement variability.

Section Analyzed	Average Height (mm)	Standard Deviation on Height (mm)	Average Width (mm)	Standard Deviation on Width (mm)
Reference 1	0.6947	0.0038	2.0287	0.0098
Reference 2	0.7093	0.0034	2.0582	0.0105
Reference 3	0.7003	0.0041	2.0568	0.0114
Reference Average	**0.7014**	**0.0071**	**2.0479**	**0.0172**
Corroded 1	0.5817	0.0400	1.7809	0.4400
Corroded 2	0.6297	0.0259	2.0023	0.0264
Corroded 3	0.6298	0.0366	1.9801	0.1001
Corroded 4	0.6020	0.0479	1.9466	0.1657
Corroded Average	**0.6108**	**0.0429**	**1.9274**	**0.2518**
Total Loss	**0.0906**	**0.0434**	**0.1204**	**0.2524**

The method applied to determine a unified thickness calculates the total cross-sectional area of metal that disappeared and distributes it evenly over the specimen's original perimeter. Instead of treating height or width loss as separate, independent values, this approach views the corroded metal as a single, continuous layer removed from all four sides of the metallic core. The resulting value of 47.2 ± 32 μm provides a single, normalized measurement that can be directly compared to the cumulative thickness loss reported by the remotely recorded sensor signal prior to its decommissioning.

Table 6-8 summarizes the thickness loss for the three calibration steel panels retrieved from the decommissioned field Panel 5. To ensure a representative assessment of the material degradation, three independent cross-sectional cuts (lines a, b, and c) were analyzed for each specimen, yielding an aggregate thickness loss of 31.9 ± 25.8 μm. This high standard deviation reflects the non-uniform nature of the atmospheric corrosion experienced across the different sampling lines.

Table 5-8. Thickness loss averages and standard deviations for calibration steel panels from Panel 5, based on three independent cross-sectional analyses per panel.

Calibration Sample	Line	Average Thickness Loss (μm)	Standard Deviation on Thickness Loss (μm)
1	1	28.18	19.16
	2	31.72	20.79
	3	28.18	24.82
2	1	30.35	22.28
	2	33.61	25.03
	3	21.48	22.71
3	1	36.08	26.59
	2	37.57	28.23
	3	39.94	33.90

The physical measurements from the 12-month exposure period reveal a notable reversal in material performance compared to the initial laboratory projections. On Panel 5, while the weathering steel (WS) specimen exhibited a higher unified thickness loss of 47.2 ± 32 μm, the calibration steel panels showed a lower average loss of 31.9 ± 25.8 μm. This result stands in direct contradiction to the comparative analysis table (**Table 6-6**), which indicates that the weathering steel should approach C3 level significantly more slowly than the calibration steel. Specifically, the table shows the calibration panels entering the C3 zone at 91.1 hours, whereas the WS sensor was projected to take 138.7 hours, suggesting that the superior corrosion resistance observed during the laboratory cyclic corrosion test did not translate to the specific environmental conditions of the bridge micro-climate.

To reconcile the observed discrepancies, it is necessary to re-examine the kinetic transition identified in laboratory testing through a modified projection of the thickness loss. **Figure 6-51** was adapted from **Figure 6-36** by applying a vertical offset of 35.04 μm to the continuous trend (i.e., Regime 2 in **Figure 6-36**), allowing for an investigation into what the material recession of weathering steel would have been had the corrosion followed a linear path from the very beginning. By forcing the steady-state linear fit, observed between 250 and 600 hours, to pass through the origin (0,0), this model effectively bypasses the initial incubation and acceleration phases where the corrosion rate was significantly lower. This hypothetical “linear-from-start” scenario illustrates that the early-state resistance of the weathering steel in laboratory conditions accounted for a roughly 35 μm “credit” in thickness preservation. If the environment on the bridge prevented this protective phase from developing early on due to immediate exposure to high-chloride events or prolonged time of wetness, the cumulative loss would naturally shift toward the higher values recorded by the field sensors.

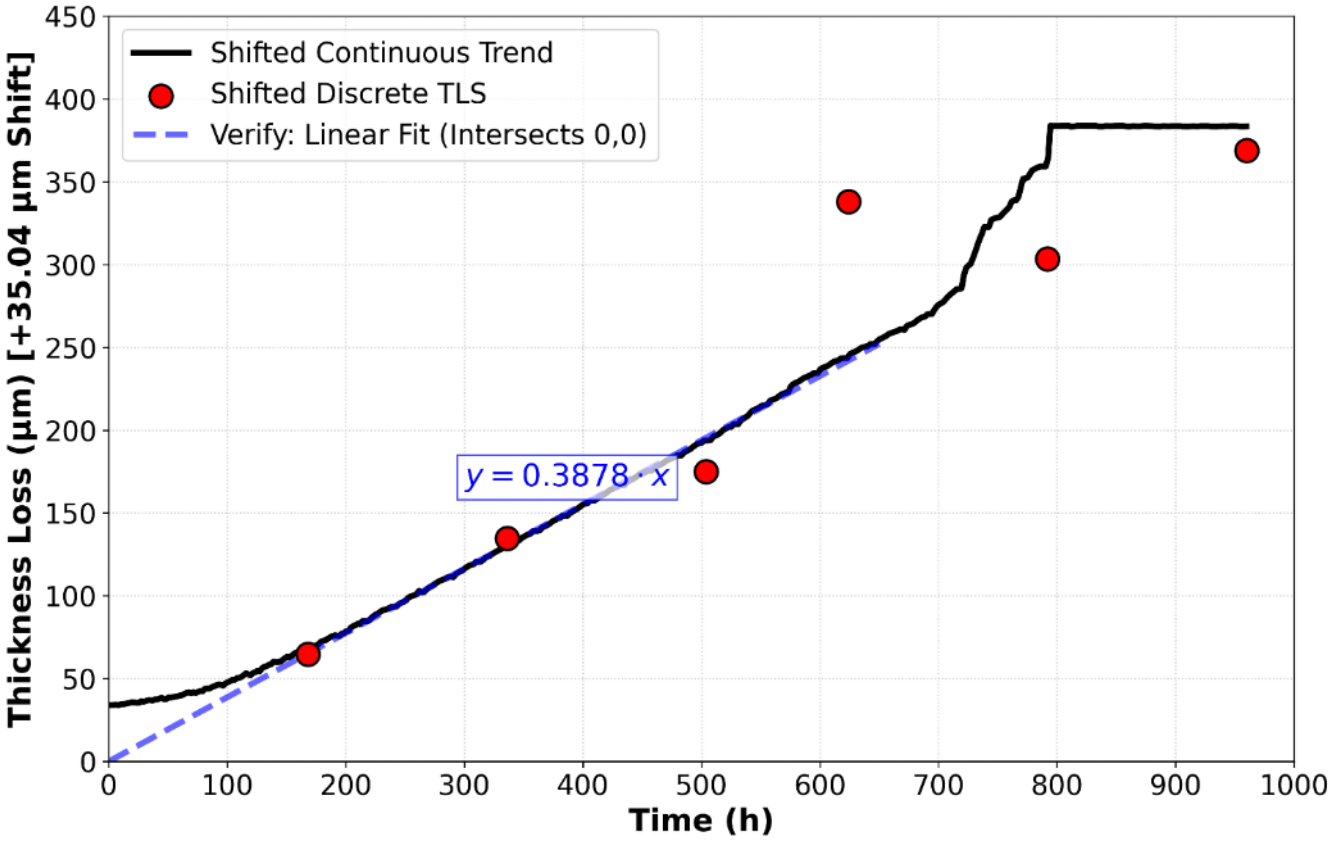

Figure 5-51. Shifted thickness loss profile for the weathering steel TLS, incorporating a 35.04 µm offset to align steady-state kinetics with the origin. The linear regression (TL = 0.3878t), calculated between 250 and 600 hours, demonstrates that the corrosion rate remains constant once the initial induction phase is bypassed.

Combining the linear thickness loss measured as a function of time for the calibration steel panels (**Figure 6-34**) with the linearized weathering steel thickness loss (**Figure 6-51**), the following relationship was established:

$$TL_{WS} = 1.422TL_{steel} - 0.735 \quad (6\text{-}2)$$

This predictive correlation, illustrated in **Figure 6-52**, indicates that the weathering steel thickness loss is approximately 42% higher than that of the carbon steel calibration panels under these specific conditions (i.e., incubation period for WS corrosion is bypassed). This linear model maps the expected thickness loss of weathering steel against the standard ISO 9223 thresholds; for example, when the calibration panels reach the 80 µm threshold (C5), the weathering steel is projected to have reached 113.0 µm in thickness loss. This relationship is critical for interpreting the 12-month data from Panel 5, as it reconciles why the weathering steel sensors (47.2 µm) ultimately exhibited greater thickness loss than the calibration panels (31.9 µm). Notably, the ratio observed in the field (47.2 µm / 31.9 µm = 1.48) aligns remarkably well with the laboratory-derived slope of 1.42. These results strongly support the hypothesis that the protective incubation period for weathering steel typically observed in controlled

environments was bypassed in service, resulting in immediate and steady-state corrosion of the weathering steel from the very beginning of its in-field exposure. This suggests the laboratory environment, characterized by higher temperatures and more efficient drying steps, is more effective at preserving the initial oxide layer than the actual bridge micro-climate. While these environmental factors are likely drivers of the discrepancy, further study is needed to confirm the exact mechanism.

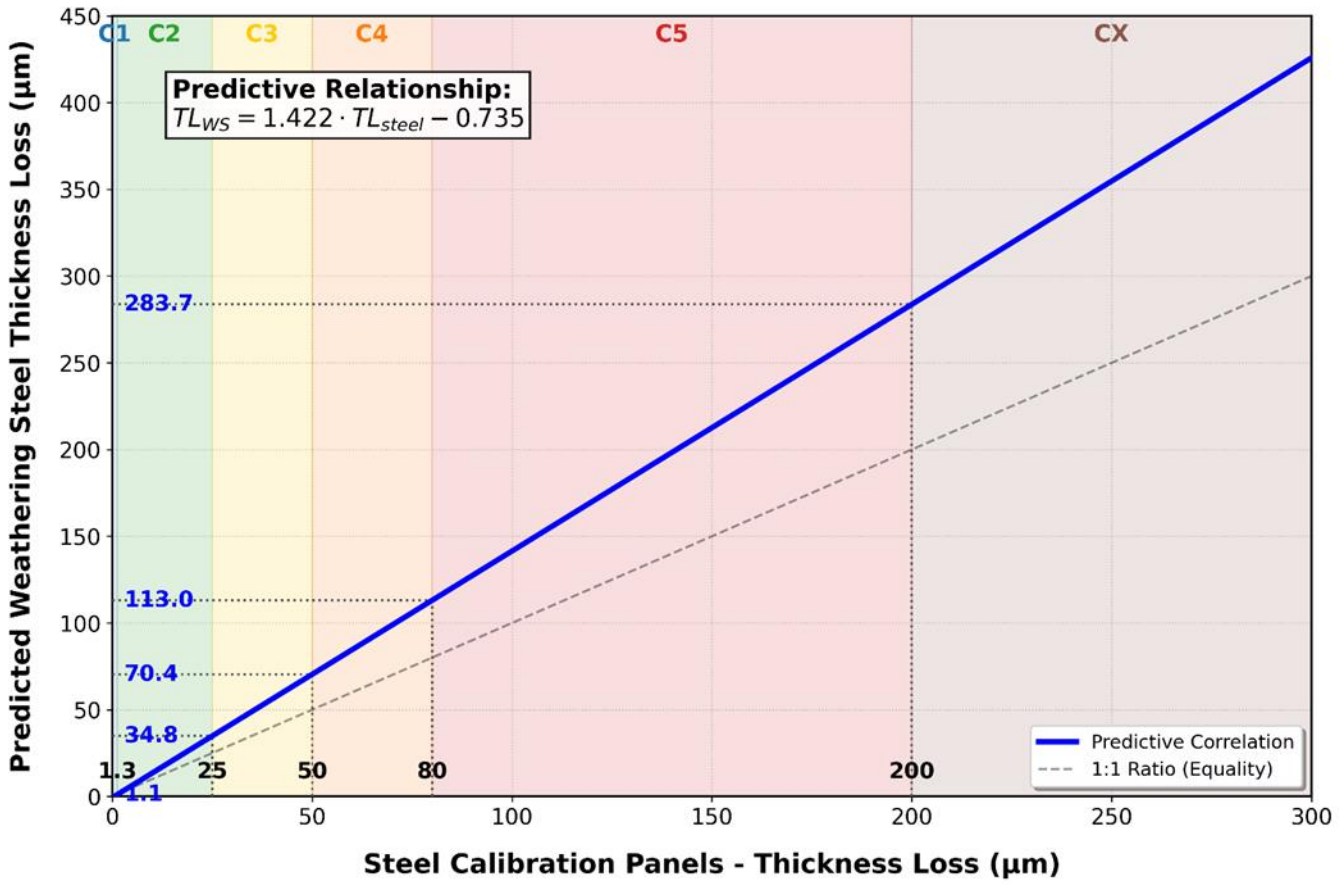

Figure 5-52. Predictive relationship between weathering steel thickness loss (TL_{WS}) and steel calibration panel thickness loss (TL_{steel}) derived from linearized laboratory kinetics, mapping the projected degradation against standard ISO 9223 corrosivity zones.

As illustrated in **Figure 6-53**, the individual field measurements from the calibration steel panels on Panel 5 (grey bars, data from **Table 6-8**) are compared against predicted weathering steel values (orange bars) derived from the laboratory-based correlation model (Equation 6-2). This comparison utilizes the individual thickness loss results from three calibration panels removed from Panel 5, each analyzed across three distinct cross-sectional lines to capture local environmental variability. By applying the established linear relationship ($TL_{WS} = 1.422TL_{steel} - 0.735$) to these specific data points, the expected weathering steel thickness loss was calculated for each location to model its performance within the real environment. The resulting analysis shows a measured global average of 31.9 µm for the calibration steel

panels, as mentioned previously, and a predicted average 44.6 µm for the weathering steel. This prediction aligns remarkably well with the actual field-measured thickness loss of 47 ± 32 µm obtained from the physical cross-sections of the weathering steel sensors themselves. This high degree of correlation validates the predictive model and confirms that, during in-field testing, the weathering steel sensors exhibited a higher thickness loss than the calibration panels because they entered a steady-state corrosion regime immediately upon exposure, without the benefit of the initial protective incubation period observed during the laboratory cyclic corrosion test.

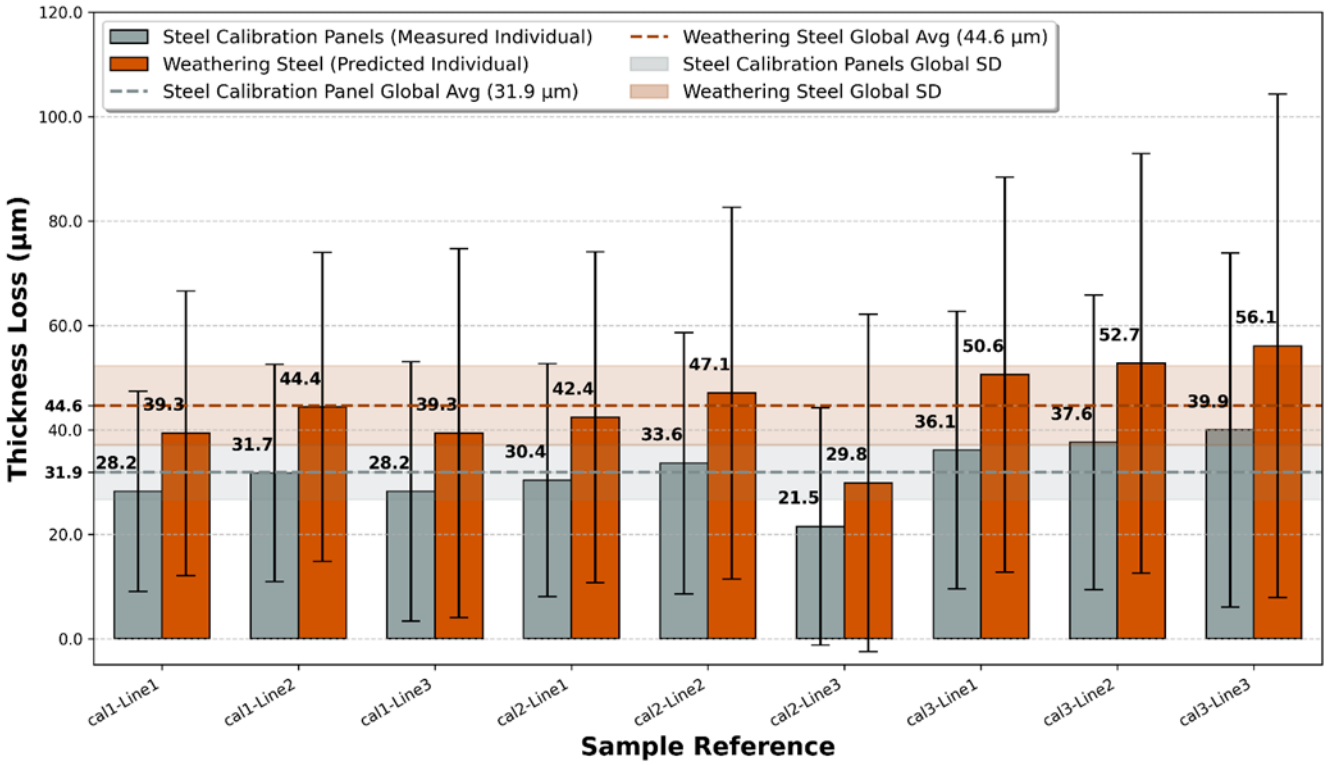

Figure 5-53. Comparative thickness loss (µm) of measured individual calibration steel panels and predicted weathering steel specimens using Equation (6-2), across the nine cuts made on the 3 sample references, featuring global averages and standard deviation bands for both material types.

As a point of reference, the 100 mm × 100 mm weathering steel specimen exposed on Panel 5 exhibited a thickness loss of 38.4 µm based on weight loss measurements. This value is lower than both the microscopic measurements conducted on the connected TLS (47.2 µm) and the model predictions (44.6 µm), a discrepancy likely attributable to the non-uniform exposure conditions between the front and back of the large specimen. Because the rear surface typically experienced less aggressive corrosion, the global average derived from weight loss is naturally lower than the localized measurements obtained from cross-sectional microscopy. Nevertheless, this thickness loss remains higher than the 31.9 µm average measured for the calibration steel panels, which is consistent with the established trend of the weathering steel

experiencing greater material degradation than the standard carbon steel in this specific environment.

With the physical thickness loss of the connected weathering steel (WS) sensor from Panel 5 now quantified, this result is compared to the thickness loss derived from the remote TLS signal to evaluate the monitoring system's performance. This step allows for a direct correlation between the empirical measurements obtained from cross-sectional analysis and the real-time data transmitted during the 12-month structural exposure, providing a clear assessment of the sensor's accuracy in the field. As illustrated in Figure 6-45, the remote monitoring system recorded a thickness loss of approximately 60 μm for Plate 5 by the conclusion of its 1-year exposure. Since the thickness loss of the decommissioned sensor has now been physically measured at 47.2 ± 32 μm, the remote TLS signal is seen to provide a slightly conservative overestimation of the actual degradation.

This overestimation is a direct consequence of how an electrical-resistance (ER) sensor infers thickness, combined with the fact that corrosion is rarely uniform along the sensing track. The sensor measures the total resistance of the element and converts it to a mean corrosion depth through the inverse relationship between resistance (R) and cross-sectional area, i.e. $R \propto \text{length} / (\text{width} \times \text{thickness})$, under the assumption that the material thins equally over the entire length of the track. In reality, the sensing track behaves like a set of resistors connected in series: it can be thought of as a chain of short segments, each with its own local thickness, whose resistance is proportional to its length and inversely proportional to its remaining cross-sectional area. The measured resistance is therefore the sum of all the individual segment resistances.

Because resistance is inversely proportional to thickness, a locally thinned "bottleneck" section contributes a disproportionately large increase to this sum, and thin spots inflate the total resistance far more than thick spots reduce it. When this total resistance is converted back to a single equivalent thickness under the uniform-thinning assumption, the result is effectively the harmonic mean of the local thicknesses rather than their arithmetic average. Since the harmonic mean is always lower than (and is dominated by) the smallest values, the reported thickness is weighted toward the most severely corroded segments. Consequently, the ER sensor does not report a representative average of the entire system, but a value biased toward its local minima, which explains the slightly higher thickness-loss values seen in the remote signals relative to the physical cross-sections.

Despite the slight overestimation, the 60 μm thickness loss recorded by the remote sensor remains well within the statistical spread of the physical field data presented in **Figure 6-53**. As shown by the expansive error bars for the weathering steel (orange), the localized variability of the corrosion attack frequently results in thickness loss values that significantly exceed the global average. This overlap confirms that the remote signal is statistically consistent with the physical measurements, as the sensor’s "bottleneck" sensitivity naturally aligns the reported data with the most severe local degradation captured within the sensing track.

5.10 Site-Specific Corrosivity Mapping and ISO 9223 Threshold Calibration for Weathering Steel

The 1-year thickness loss values of weathering steel across the various monitored positions on the bridge were extracted from the remote sensing data (**Figure 6-45**) and summarized in **Table 6-9**. These results provide a comprehensive map of the site-specific corrosivity, capturing the significant impact of local micro-climates and component orientations on the overall rate of degradation. The dataset encompasses a diverse range of environmental exposures, from the relatively sheltered right abutment wall to the high-intensity splash zones directly above the traffic lanes and on the bridge piers. The analysis of **Table 6-9** reveals that location and orientation are the primary drivers of environmental severity on the bridge, creating distinct micro-climates where corrosion intensities vary by a factor of more than 3. The data clearly delineates three tiers of exposure:

- The "Mist Trap" (Downward-Facing, Above Lanes): The most aggressive conditions are observed at locations 3.1 and 4, where plates are positioned directly above the traffic lanes and oriented facing downwards. These horizontal surfaces act as collectors for the saline mist and aerosolized road spray generated by vehicles. Notably, these results align well with the visible corrosion products on the flat, downward-facing surfaces of the girders, as illustrated in **Figures 6-24** and **6-25**. The #2 (middle) lane (3.1) exhibits the absolute maximum thickness loss of 95.5 µm, likely due to the higher volume of heavy-duty vehicles, which increases the intensity of the salt plume compared to the #1 (left) lane (4) at 85.4 µm.
- Vertical Pier & Lane Exposure: Locations 5 and 6 (the piers) and the vertical plates above the #2 (middle) lane (3.2 and 3.3) show a consistent mid-range thickness loss of approximately 56 to 60 µm. While these areas are still within the "splash zone," their vertical orientation facilitates better drainage and allows for a thinner electrolyte film compared to downward-facing surfaces. As noted previously, even when galvanic currents are low on the pier vertical assemblies, the persistent humidity from the road is sufficient to maintain a steady thickness loss, but lower than for downward-facing specimens.
- The Sheltered Zone: The Right Abutment Wall (location 1) presents the lowest thickness loss at 28.8 µm. Its position, vertical and parallel to traffic but further removed from the direct "splash plume", significantly reduces the chloride deposition rate.

Table 5-9. Summary of 1-year weathering steel (WS) thickness loss across the monitoring network, categorized by specific bridge location and spatial orientation (data extracted for Figure 6-45).

Panel	Location / orientation	1-Year WS TL (µm)
1	On the right abutment wall, vertical & parallel to direction of traffic	28.8
2	Above the acceleration, facing downwards	50.6
3.1	Above #2 (middle) lane, facing downwards	95.5

3.2	Above #2 (middle) lane, vertical & parallel to direction of traffic	56.5
3.3	Above #2 (middle) (left) lane, vertical & facing oncoming traffic	56.7
4	Above the #1 (left) lane, facing downwards	85.4
5	Lower section of the second pier, vertical & parallel to direction of traffic	60.2
6	Top of the first pier, vertical & parallel to direction of traffic	59.0

Table 6-10 presents the localized ISO 9223 corrosivity categories mapped specifically for weathering steel (WS) using the predictive correlation model developed in this study (extracted from **Figure 6-52**). By translating the standard 1-year carbon steel thickness loss thresholds through the established relationship presented as Equation (6-2) ($TL_{WS} = 1.422TL_{steel} - 0.735$), we can directly classify the bridge micro-climates based on the WS sensor signals and physical measurements. For example, while the standard C3 range for carbon steel is 25-50 μm, the equivalent range for weathering steel is adjusted to 34.8-70.4 μm. These Year-1 values serve as the essential baseline corrosion rate required for the next stage of the study: applying ISO 9224 to project whether the corrosion will stabilize or continue at these heightened rates over the coming years.

*Table 5-10**.** ISO 9223 corrosivity category thresholds defined by 1-year thickness loss ranges for carbon steel and the corresponding calculated ranges for weathering steel (WS) based on Equation (6-2)**.***

ISO 9223 Categories	1-Year Carbon Steel Thickness Loss Range as per ISO 9223 (μm)	TL Range for WS Associated to ISO9223 Categories, as per Equation (6-2) (μm)
C1	≤ 1.3	≤ 1.1
C2	[1.3 – 25]	[1.1 – 34.8]
C3	[25 – 50]	[34.8 – 70.4]
C4	[50 – 80]	[70.4 – 113.0]
C5	[80 – 200]	[113.0 – 283.7]
CX	[200 – 700]	[283.7 – 995.0]

The spatial distribution of corrosion severity across the bridge can be visualized in **Figure 6-54**, which maps the 1-year thickness loss data directly onto a schematic of the monitored zones. Each location is represented by a calibrated gauge that classifies the local micro-climate according to the weathering steel-specific ISO 9223 thresholds established throughout this study and summarized in **Table 6-10**. This comprehensive mapping illustrates how environmental aggressiveness is heterogeneously distributed across the superstructure, with the highest severity levels concentrated on downward-facing surfaces directly above the travel lanes.

To provide a comprehensive spatial context for the 12-month data, **Figures 6-55** through **6-58** present the localized thickness loss gauges overlaid onto their corresponding physical locations across the entire bridge structure. This in-situ visualization maps the remote sensing results, ranging from the high-intensity 95.5 μm “mist trap” zones above the #2 (middle) lane to the sheltered 28.8 μm**,** environment of the right abutment wall, directly onto the structural

components they monitor. By situating the data within the actual bridge geometry, these figures illustrate how environmental heterogeneity is dictated by a combination of component orientation, proximity to traffic-generated road spray, and structural shielding. This spatial representation confirms that while the global environment may be classified generally, the actual material corrosion rate varies by a factor of three depending on specific micro-climate factors.

(a)

(b)

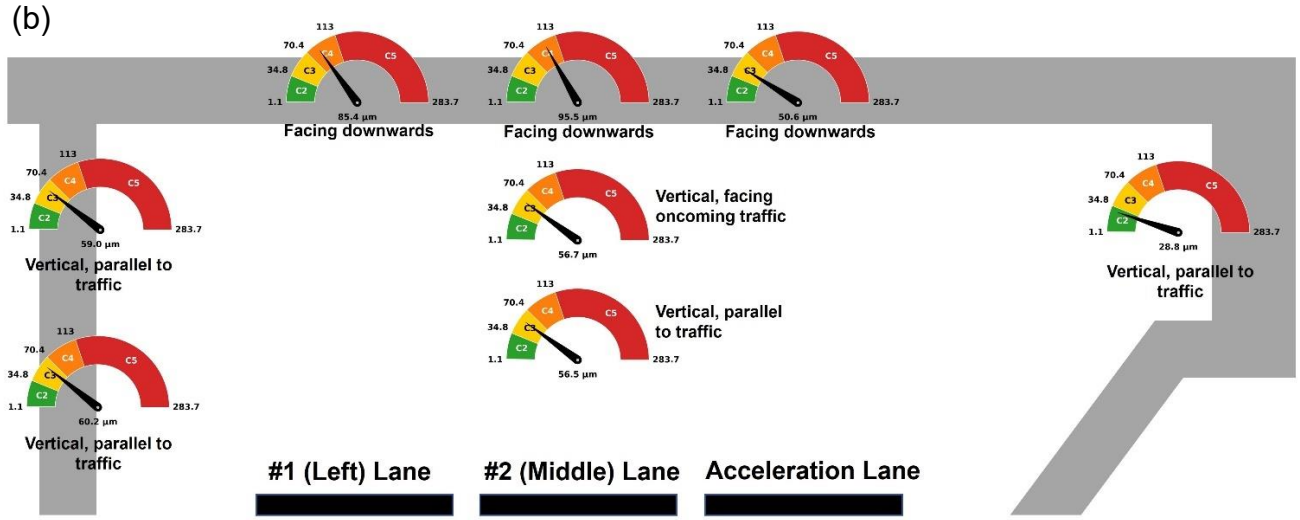

Figure 5-54. (a) Overview photograph of the monitored bridge structure and (b) corresponding spatial corrosivity map illustrating the thickness loss across various micro-climates after 12 months of exposure. The schematic in

(b) provides a direct representation of the structural elements shown in (a), with individual gauges displaying localized material degradation mapped against adjusted ISO 9223 categories (C2–C5) specifically calibrated for weathering steel.

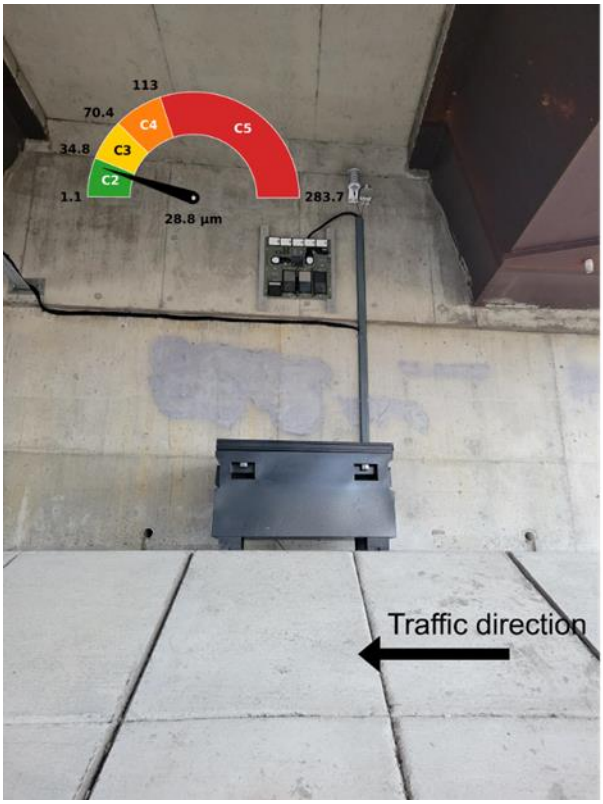

Figure 5-55. In-situ monitoring results for the weathering steel sensor installed on the Right abutment wall (panel 1).

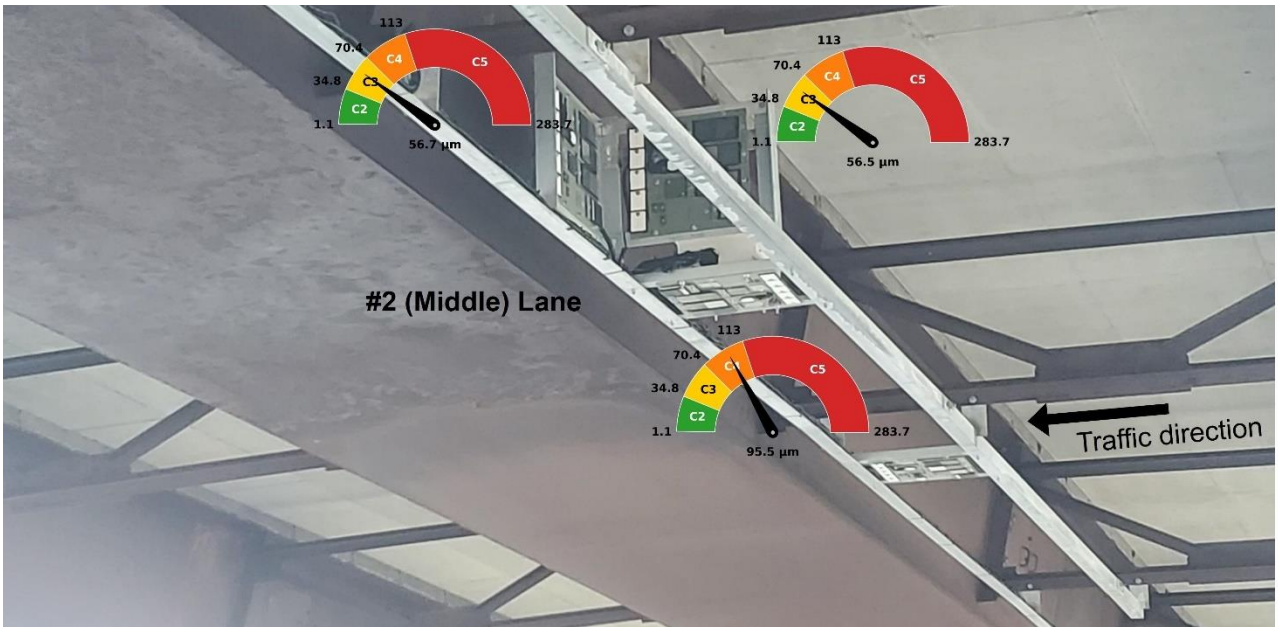

Figure 5-56. In-situ monitoring results for the three weathering steel sensors positioned above the #2 (middle) lane (panels 3.1, 3.2, and 3.3). The gauges demonstrate the direct correlation between structural orientation and environmental severity.

Figure 5-57. In-situ monitoring results for the weathering steel sensors installed on the bridge piers (panels 5 and 6).

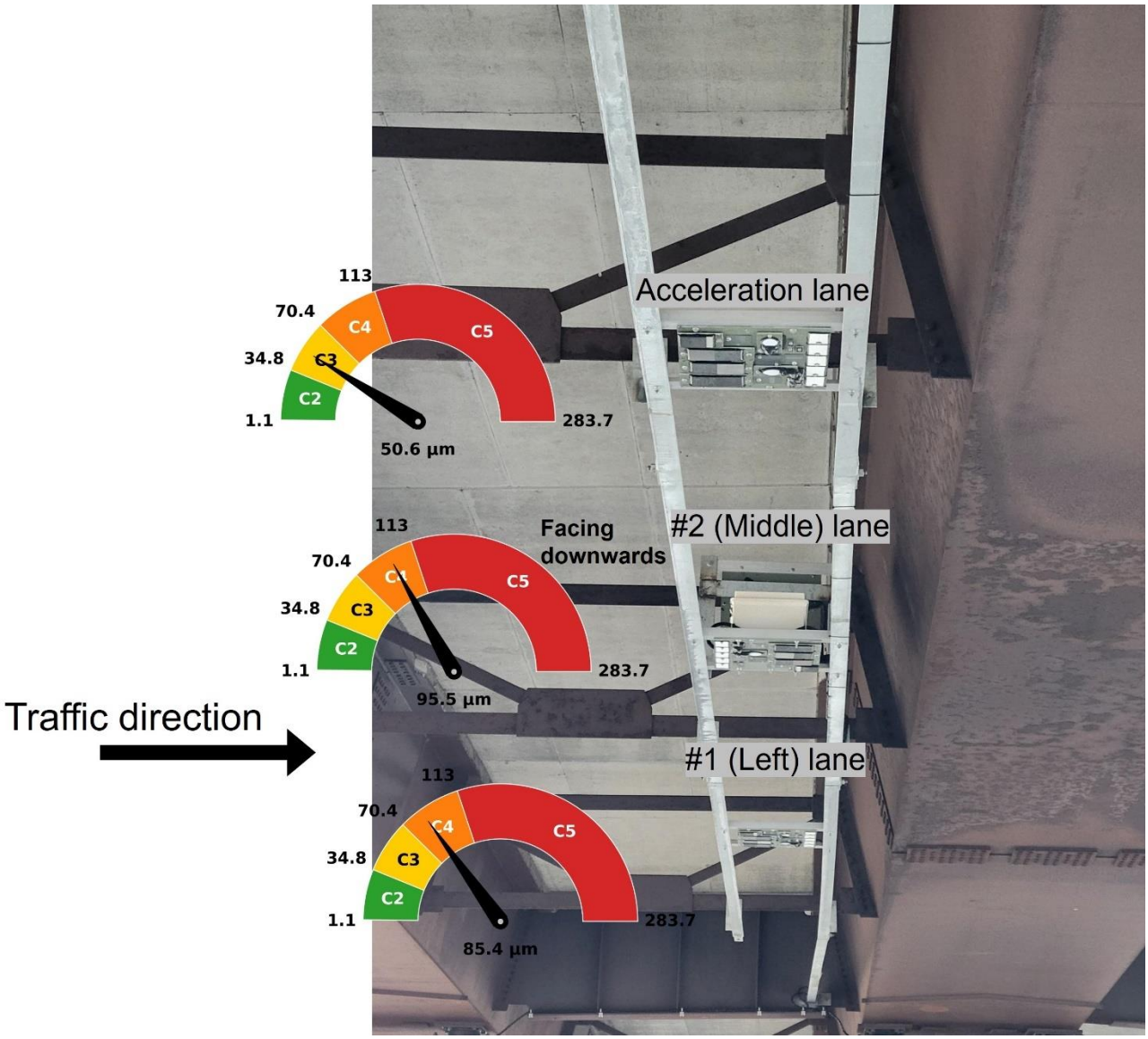

Figure 5-58. In-situ monitoring results for downward-facing weathering steel sensors positioned directly above the travel lanes and the acceleration lane.

5.11 Equivalent GMW14872 Test Durations for Observed In-Field Thickness Loss

Figure 6-59 presents a hybrid analytical model for weathering steel (WS) corrosion under cyclic corrosion test GMW14872, establishing a direct correlation between laboratory exposure time (t) and in-field sensor-measured thickness loss (TL). While previous findings indicate that correlating in-field carbon steel calibration with WS requires bypassing the laboratory incubation period in favor of a linear model from t_0, this figure evaluates the use of the cyclic corrosion test (CCT) as a standalone predictive tool. In this context, the blue 'X' markers represent the "solved targets", i.e., the precise laboratory durations required to reach the 1-

year in-field thickness loss experienced across the eight different bridge panels. By mapping these field results directly onto the CCT kinetic curve, the model provides a mathematical framework to translate accelerated laboratory hours into real-world structural performance for each specific micro-climate.

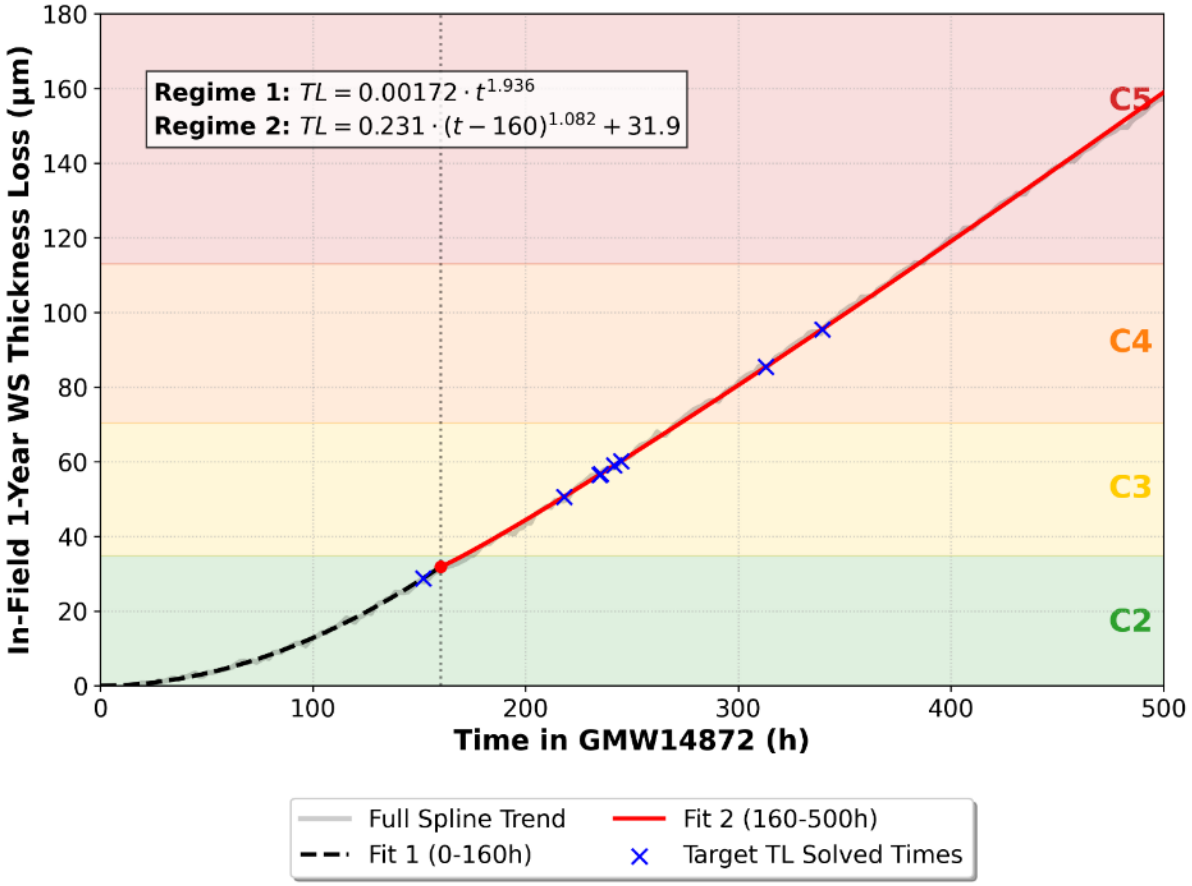

Figure 5-59. Hybrid analytical model for weathering steel (WS) thickness loss under GMW14872 cyclic corrosion testing, overlaid with the ISO 9223 corrosivity categories (C2-C5) specifically calibrated for WS (see Figure 6-52). This model serves as a standalone predictive tool to directly translate accelerated laboratory hours into real-world weathering thickness loss.

At the timestamps marked by blue crosses in **Figure 6-59**, representing the CCT durations required to replicate in-field thickness losses, the cumulative galvanic charges for the three CFRP-AA6022 sensors exposed to the CCT were extracted from the laboratory datasets. These charges were then plotted against the in-field thickness losses, with the resulting correlations shown in **Figure 6-60**. As a result, **Figure 6-60** shows that this galvanic couple can be used during the laboratory corrosion procedure as a translation medium for converting cumulative galvanic charge of a specific couple into physical thickness loss of weathering steel. By establishing these high-precision linear regressions ($R^2 > 0.997$), the galvanic sensor data provides a direct mathematical link between the laboratory's accelerated charge accumulation (Q) and the WS thickness loss (TL) observed in the field. This allows the

laboratory corrosion procedure to serve as a quantitative predictive tool, where the cumulative charge generated by the CFRP-AA6022 sensors acts as a real-time proxy for the 1-year environmental severity across diverse micro-climates.

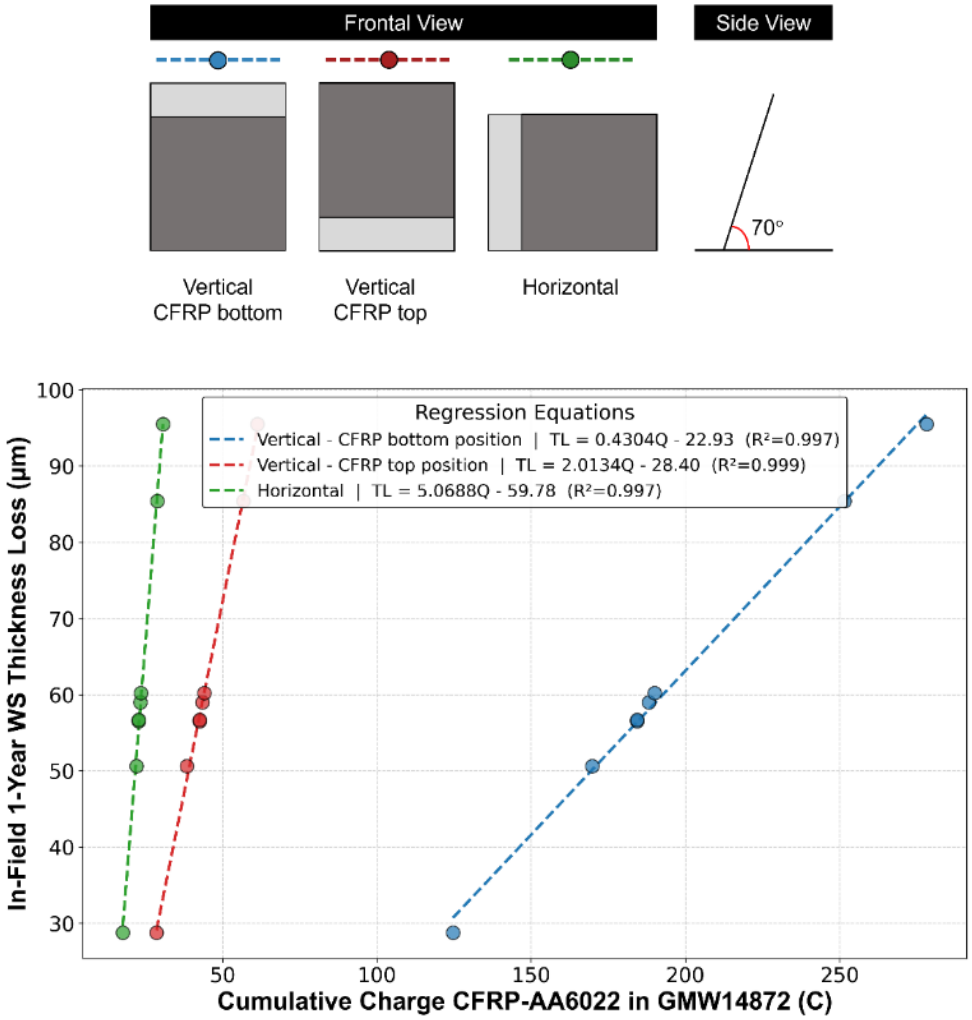

Figure 5-60. Correlation between the cumulative galvanic charge (Q) measured by CFRP-AA6022 sensors during GMW14872 testing and the observed 1-year in-field thickness loss for weathering steel. The upper schematics illustrate the three sensor configurations in the cyclic corrosion chamber.

5.12 Seasonal Corrosion Kinetics of Weathering Steel at Guard Rail Height

Figure 6-61 illustrates the seasonal evolution of the cumulative thickness loss (calculated from weight loss after oxide removal, and assuming equal loss on both sides of the coupons) for weathering steel panels installed at the guard rail height, where the corrosion kinetics are governed by the interplay between aggressive salt-loading and natural rinsing. The data reveals a highly non-linear process, beginning with a massive initial surge during the winter

months (Samples 1 & 2; approx. 40 µm) that is directly attributable to the proximity of the guard rail to the highway splash zone and the heavy deposition of de-icing salts. Notably, the additional thickness loss accumulated over the remainder of the year (Sample 5 – Sample 1 or 2 = approx. 16 to 18 µm) is significantly lower than the mathematical sum of the isolated seasonal exposures (sum of Samples 6, 7, and 8 = 29.1 µm; represented by the individual seasonal bands). This discrepancy provides empirical evidence that the corrosion product acts as a physical barrier that is progressively built over the course of the year. As this layer thickens, it creates an increasingly restrictive path for the diffusion of oxygen and moisture to the underlying metal. Consequently, while the "fresh" steel in the individual seasonal tests remains fully exposed and vulnerable to initial atmospheric attack, the results show that for the panels continually exposed, the thickness loss is virtually zero during the summer and fall. These cumulative samples benefit from a growing physical obstruction that effectively dampens the corrosion rate in the later stages of exposure. With a total annual thickness loss of 58.5 µm (Sample 5), this specific location is classified as C3 according to the adjusted ISO 9223 thresholds.

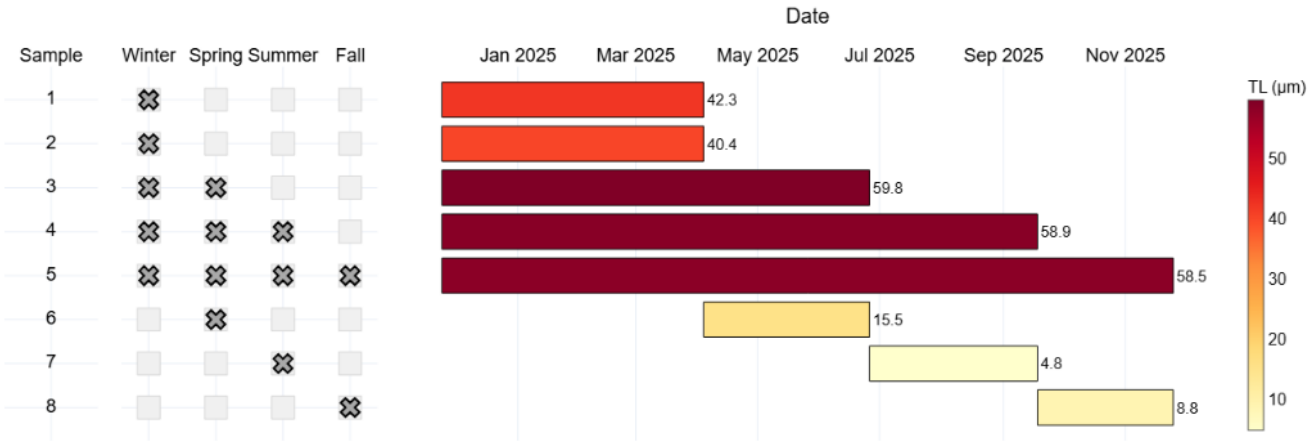

Figure 5-61. Breakdown of cumulative thickness loss for weathering steel based on seasonal exposure windows from November 2024 to November 2025. The left-hand grid identifies the specific seasons encompassed by each exposure period (marked with an 'X'), while the corresponding horizontal bars quantify the resulting thickness loss in micrometers.

6 Summary and Key Findings

6.1 Summary

Weathering steel represents a cornerstone material in the transition toward sustainable, low-maintenance bridge infrastructure, offering an autonomous corrosion-protection mechanism that substantially reduces lifecycle costs and eliminates the environmental burden of periodic coating systems. However, the integrity of this protection is entirely contingent on the formation and stabilization of a dense, adherent nanophase patina; a process that is highly sensitive to local environmental conditions and can be irreversibly compromised by chloride accumulation, chronic moisture, or inadequate detailing. The consequences of patina failure are not merely aesthetic; undetected section loss in primary structural members directly undermines load-carrying capacity and long-term serviceability, making the accurate evaluation of corrosion performance a structural safety imperative rather than a maintenance convenience.

At the material qualification stage, the modified GM 9540P (now GMW14872) cyclic corrosion test was identified as an accelerated protocol for evaluating WS alloys intended for Canadian bridge applications, as it provides the strongest predictive alignment with long-term field performance. At the phase characterization level, X-Ray Diffraction (XRD) analysis is indispensable for quantifying the ratio of protective goethite (α-FeOOH) to deleterious akaganeite (β-FeOOH) and lepidocrocite (γ-FeOOH) within the patina, providing a definitive assessment of oxide stability through established indices such as the Protective Ability Index (PAI) and its modified variant for chloride-rich environments. Complementary surface characterization through Scanning Electron Microscopy (SEM) and Energy Dispersive Spectroscopy (EDS) further reveals the morphological integrity of the oxide layer and confirms the presence and distribution of chloride contamination within the patina matrix. In the field, non-destructive patina thickness measurement using electromagnetic induction gauges, combined with gravimetric mass loss analysis in accordance with ASTM G1-03, provides the quantitative corrosion rate data required to validate design assumptions and calibrate predictive degradation models.

It is precisely the disconnect between regional classification and localized structural reality, however, that establishes the critical need for continuous, in-situ monitoring as the final and most decisive layer of this evaluation framework. The deployment of Electrical Resistance (ER) thickness loss sensors at strategically selected structural positions (spanning the full range of micro-environmental zones from sheltered abutments to downward-facing mist-trap surfaces above active traffic lanes) provides the continuous, real-time corrosion rate data that bridges the gap between periodic laboratory assessments and the evolving structural reality of a bridge in service. Only through the integration of these real-time sensing technologies can bridge owners detect the onset of accelerated corrosion, validate whether the patina is stabilizing as designed, and make evidence-based intervention decisions before irreversible section loss occurs.

This need is particularly acute given that regional macro-environmental classifications alone are insufficient to characterize the true corrosion demand experienced by a structure. A bridge situated within a nominally benign C2 or C3 macro-environment can sustain localized micro-environments that effectively reach C4 corrosivity (driven by the tunnel effect, poultice formation, de-icing salt accumulation, and low vertical clearance over trafficked lanes) conditions that standard site assessments and periodic visual inspections are inherently unable to capture in real time. Neither of these conventional approaches provides the quantitative, phase-specific data necessary to confirm whether a patina is developing protectively or deteriorating toward structural compromise. A rigorous, multi-tiered testing and monitoring program is therefore appropriate and recommended at every stage of a bridge's lifecycle; from material qualification prior to procurement, through accelerated laboratory evaluation during design, to in-situ monitoring and periodic physical assessment throughout the service life of the structure.

6.2 Future Research and Development Priorities

Moving forward, the primary objective is to extend the current monitoring campaign through Years 2 and 3 to capture the long-term evolution of the corrosion kinetics across the bridge's various micro-climates. While the Year 1 results provided an initial corrosivity classification based on ISO 9223, the subsequent multi-year datasets will enable the transition to ISO 9224 for the calculation of guiding values for long-term atmospheric corrosion. By analyzing the thickness loss over a three-year window, it will be possible to determine if the "no incubation" behavior observed in Year 1 persists or if the weathering steel eventually develops a more protective patina that shifts the kinetics toward a stabilizing power-law exponent. This longitudinal approach will refine the predictive accuracy of the current models, ultimately allowing for more reliable estimates of the remaining service life and the long-term environmental durability of the structural components.

While ISO 9223 establishes the initial "speed limit" of environmental severity, ISO 9224 provides the framework for calculating long-term guiding values. By utilizing the power-law equation, the progression of material degradation can be projected over the intended service life of the structure:

$$TL(t) = r_1 t^n \quad (7\text{-}1)$$

where:

TL(t): Cumulative thickness loss at time t (μm)

r_1: the first-year corrosion rate (the baseline established in this report)

t: time in years (Years in service)

n: the corrosion-dependent exponent

The determination of n represents the most critical phase of the long-term durability assessment, as it defines the "weathering" capability of the steel in its specific micro-climate. The integration of Year 2 and Year 3 data is essential to accurately evaluate this parameter:

Linear corrosion (n approx. 1.0): If the exponent remains near unity, the weathering steel is failing to stabilize. In this scenario, the material lacks a sufficiently protective surface, causing it to corrode similarly to standard carbon steel at a steady, linear rate but 1.4 times faster.

Protective stabilization (n < 0.6): A significant drop in the exponent provides clear physical evidence that the corrosion product is successfully acting as a physical barrier. As this layer densifies, it increasingly restricts the diffusion of oxygen and electrolytes to the metal surface, confirming that the material is performing as intended by "weathering" to protect the underlying structural section.

By establishing the r1 baseline from the current sensor and TLS datasets, the foundation is now set to quantify these kinetic shifts. This will allow for the projection of whether the high-intensity zones will eventually stabilize or if they will require specialized maintenance interventions in the remaining service life.

7 References

[1] Morcillo M, Díaz I, Cano H, Chico B, De la Fuente D. Atmospheric corrosion of weathering steels. Overview for engineers. Part I: Basic concepts. Constr Build Mater 2019;213:723–37.

[2] Morcillo M, Díaz I, Cano H, Chico B, De la Fuente D. Atmospheric corrosion of weathering steels. Overview for engineers. Part II: Testing, inspection, maintenance. Constr Build Mater 2019;222:750–65.

[3] Albrecht P, Hall Jr TT. Atmospheric corrosion resistance of structural steels. Journal of Materials in Civil Engineering 2003;15:2–24.

[4] Aisc, Nsba. Uncoated Weathering Steel Reference Guide. 2022.

[5] Albrecht P, Coburn SK, Wattar FM, Tinklenberg GL,, Gallagher WP,. Guidelines For the Use of Weathering Steel in Bridges. Washington D.C.: 1989.

[6] El Sarraf R, Mandeno W,, Hicks S,. Weathering Steel-Design Guide for Bridges in Australia. Manukau, Auckland City: 2017.

[7] Ungermann D, Hatke P, Committee B. ECCS European design guide for the use of weathering steel in bridge construction. 2021.

[8] Han C, Li Z, Yang X, Wang J. Corrosion Behavior and Mechanical Performance of Weathering Steel in Industrial and Rural Atmospheric Environments. Constr Build Mater 2024;411:134284. https://doi.org/https://doi.org/10.1016/j.conbuildmat.2023.134284.

[9] Mccuen RH, Asce M, Albrecht P. Effect of Alloy Composition on Atmospheric Corrosion of Weathering Steel. Journal of Materials in Civil Engineering 2005;17:117–25. https://doi.org/10.1061/ASCE0899-1561200517:2117.

[10] Hamby G. High Performance Steel Designers' Guide. San Francisco, CA 94105: 2002.

[11] Crampton, Douglas D. Assessment of Weathering Steel Bridge Performance in Iowa and Development of Inspection and Maintenance Techniques. Northbrook, Illinois 60062: 2013.

[12] Ebrahimi N, Roshanfar M, Momeni M, Naboka O. Corrosion Performance of Atmospheric Corrosion Resistant Steel Bridges in the Current Climate: A Performance Review. Materials 2025;18. https://doi.org/10.3390/ma18153510.

[13] Ebrahimi N, Zhang J, Pan X, Naboka O, Combe J, Mermigas K. Understanding the impact of alloying elements on weathering steel's atmospheric corrosion – A ten-year bridge exposure evaluation. Constr Build Mater 2024;449:138439. https://doi.org/https://doi.org/10.1016/j.conbuildmat.2024.138439.

[14] Grandón-Soliz C, Sandoli A, Fabbrocino G. Weathering Steel in Civil Engineering and Architecture: A State-of-the-Art Review. Buildings 2025;15. https://doi.org/10.3390/buildings15132260.

[15] Jia J, Liu Z, Cheng X, Du C, Li X. Development and optimization of Ni-advanced weathering steel: A review. Corrosion Communications 2021;2:82–90. https://doi.org/10.1016/j.corcom.2021.09.003.

[16] Wang Y, Mu X, Chen Z, Lin Z, Dong J, Daniel EF, Qi J, Ke W. Understanding the role of alloyed Cu and P in the initial rust composition of weathering steel formed in a simulated coastal-industrial atmosphere. Corros Sci 2021;193. https://doi.org/10.1016/j.corsci.2021.109912.

[17] Nagoshi M, Kawano T, Kage I, Hayakawa S. Micro-beam XRF and Fe–K Edge XAFS on the Cross Section of the Rust Layer Formed on a Weathering Steel 2011.

[18] Fletcher FB,. Improved Corrosion-Resistant Steel for Highway Bridge Construction. McLean, VA: 2011.

[19] ASTM A242-24: Specification for High-Strength Low-Alloy Structural Steel 2024. https://doi.org/10.1520/A0242_A0242M-13.

[20] ASTM A588-19 - Standard Specification for High-Strength Low-Alloy Structural Steel, up to 50 ksi [345 MPa] Minimum Yield Point, with Atmospheric Corrosion Resistance 2019.

[21] ASTM A709-21- Standard Specification for Structural Steel for Bridges 2021.

[22] Daghash SM, Ozbulut OE. Mechanical Evaluation of Corrosion-Resistant Steel Plates for Bridge Girder Fabrication. In: Soules JG, editor. Structures Congress, Denver, Colorado: ASCE; 2017, p. 494–505. https://doi.org/https://doi.org/10.1061/9780784480410.

[23] ASTM A1010-13 - Specification for Higher-Strength Martensitic Stainless Steel Plate, Sheet, and Strip 2013.

[24] The AASHTO LRFD Bridge Construction Specifications. vol. 4. 2010.

[25] Stratmann M, Bohnenkamp K, Engell H-J. An Electrochemical Study of Phase-Transitions in Rust Layers. Corros Sci 1983;23:969–85.

[26] Gardiner CP, Melchers RE. Corrosion of Mild Steel in Porous Media. Corros Sci 2002;44:2459–78.

[27] Stratmann M, Hoffmann K. In Situ Mobbauer Spectroscopic Study of Reactions Within Rust Layers. Corros Sci 1989;29:1329–52.

[28] Alamilla JL, Sosa E. Stochastic modelling of corrosion damage propagation in active sites from field inspection data. Corros Sci 2008;50:1811–9. https://doi.org/10.1016/j.corsci.2008.03.005.

[29] Neff D, Dillmann P, Bellot-Gurlet L, Beranger G. Corrosion of iron archaeological artefacts in soil: Characterisation of the corrosion system. Corros Sci 2005;47:515–35. https://doi.org/10.1016/j.corsci.2004.05.029.

[30] Stratmann M, Moller J. The Mechanism of the Oxygen Reduction on Rust-Covered Metal Substrates. Corros Sci 1994;36:327–59.

[31] Helbert VS, Nazarov A, Taryba M, Vucko F, Montemor F, Thierry D. Kinetics of corrosion reactions on press hardened steel in atmospheric conditions under thin electrolyte films. Electrochim Acta 2023;458. https://doi.org/10.1016/j.electacta.2023.142500.

[32] Sancy M, Gourbeyre Y, Sutter EMM, Tribollet B. Mechanism of corrosion of cast iron covered by aged corrosion products: Application of electrochemical impedance spectrometry. Corros Sci 2010;52:1222–7. https://doi.org/10.1016/j.corsci.2009.12.026.

[33] Stratmann M, Streckel H, Kim KT, Crockett S. On the atmospheric corrosion of metals which are covered with thin electrolyte layers-iii. the measurement of polarisation curves on metal surfaces which are covered by thin electrolyte layers. Corros Sci 1990;30:715–34. https://doi.org/10.1016/0010-938X(90)90034-3.

[34] Alamilla JL, Espinosa-Medina MA, Sosa E. Modelling steel corrosion damage in soil environment. Corros Sci 2009;51:2628–38. https://doi.org/10.1016/j.corsci.2009.06.052.

[35] ISO 9223 - Corrosion of metals and alloys-Corrosivity of atmospheres-Classification, determination and estimation. vol. 9223. 2012.

[36] Adsetts JR, Ebrahimi N, Zhang J, Jalaei F, Noël JJ. Steel Bridge-Coating Systems and Their Environmental Impacts: Current Practices and Future Trends. Coatings 2023;13. https://doi.org/10.3390/coatings13050850.

[37] Morcillo M, Chico B, Díaz I, Cano H, de la Fuente D. Atmospheric corrosion data of weathering steels. A review. Corros Sci 2013;77:6–24. https://doi.org/10.1016/j.corsci.2013.08.021.

[38] Morcillo M, Díaz I, Chico B, Cano H, de la Fuente D. Weathering steels: From empirical development to scientific design. A review. Corros Sci 2014;83:6–31. https://doi.org/10.1016/j.corsci.2014.03.006.

[39] Diler E, Lédan F, LeBozec N, Thierry D. Real-time monitoring of the degradation of metallic and organic coatings using electrical resistance sensors. Materials and Corrosion 2017;68:1365–76. https://doi.org/10.1002/maco.201709655.

[40] Leygraf C. Atmospheric corrosion. In: Marcus P, editor. Corrosion mechanisms in theory and practice, CRC Press; 2011, p. 669–704.